# Energy Transfer in Biomimetic and Biosensing Molecular Nanomaterials

Wei-Hsin Chen

St Edmund Hall, Oxford




Thesis submitted in fulfilment of the requirements for the degree of

Master of Science at the University of Oxford

Trinity Term, 2013

# Energy Transfer in Biomimetic and Biosensing Molecular Nanomaterials

Wei-Hsin Chen, St Edmund Hall, Oxford

Thesis submitted in fulfilment of the requirements for the degree of
Master of Science at the University of Oxford. Trinity Term, 2013

## Abstract

This thesis is concerned with ultrafast photophysics and excitation energy transfer in biomimetic and biosensing molecular nanomaterials, which have been investigated using time-resolved photoluminescence spectroscopy.

Artificially-synthesised fully $\pi$-conjugated nanorings with 6-24 units of porphyrins incorporated have demonstrated remarkable full delocalisation of the absorbing excited state across the entire ring on an ultrafast timescale. The largest ring of 24 porphyrin units with a diameter of $\sim$10 nm is the largest man-made molecular nanoring at present. The constraint that the lowest electronic transition is forbidden due to their high molecular symmetries is released by static and dynamic distortions in the solution. These findings provide promising opportunities for using these man-made light-harvesting materials that match the efficiency of their natural counterparts in technological applications.

On the other hand, self-assembled organic fluorescent nanoparticles (NPs) formed of amphiphilic monomers with targeting ligands exhibit potential to be used in bio-sensing applications. Homotransfer and heterotransfer of excitation energy in nanoparticles have been investigated, where mannose covalently linked on Amp1-B monomers provide binding sites for Concanavalin A which is attached with energy acceptors. Increasing the molar ratios of Amp1-B-mannose and Amp3-B can increase the binding sites and forming directional energetic cascades towards the NP surface, respectively. However, the amount of these two monomers must be optimised in order to reach the highest donor–acceptor energy transfer rate in the system.

*"An indispensable hypothesis, even though still far from being a guarantee of success, is however the pursuit of a specific aim, whose lighted beacon, even by initial failures, is not betrayed."*

*Max K. E. L. Planck (1858-1947)*

# Acknowledgements

Foremost, I would like to express my heartfelt gratitude to my supportive and patient supervisor, Prof. Laura M. Herz, for her continuous support and the many discussions we have shared throughout my MSc study. I deeply appreciate the freedom Laura gave me in pursuing the goal of perfection in my experimental results. She is an ideal role model for pursuing a conscientious and careful attitude in order to achieve high-quality research performance.

I would also like to thank all of my friends in the LMH, MBJ and JLH groups, who made Clarendon life full of happiness and laughter. Thank you especially to Dr. Chaw Keong Yong for the inspirational discussions and his generous help, and Dr. Hannah J. Joyce for polishing the language in this thesis. I have really enjoyed my time working with collaborators in Oxford University. In addition, I would like to express my appreciation to the members of my examination committee, Dr. Moritz Riede and Prof. Richard Phillips, for taking their time to read and correct this thesis and providing constructive feedback.

Thank you to Prof. Harry L. Anderson, Dmitry Kondratuk and Dr. Melanie O'Sullivan for providing nanoring samples and valuable suggestions. I also feel an immense gratitude for the support of Eindhoven University of Technology. Thank you to Prof. Albertus P. H. J. Schenning and Irén Fischer for providing nanoparticle samples and plentiful conversation.

Special thanks also go to St Edmund Hall, Oxford for financial support through the William R. Miller Postgraduate Award, and my college advisor, Jeff Tseng, who always encouraged me and was available for consultation during my MSc study.

Last but not least, I would like to dedicate this thesis to my parents, Hsi-Ming Chao and Tang-Sheng Chen, and my uncle, Hsi-Hua Chao, for their financial and spiritual support and everlasting love throughout my life. Thank you for being wonderful!

# Contents


**1 Introduction** **1**

1.1 Introduction . . . . . 1

1.2 Thesis outline . . . . . 3

**2 Electronic Processes in Organic Conjugated Materials** **7**

2.1 Basic concepts of conjugated materials . . . . . 7

2.1.1 Hybrid orbital theory . . . . . 8

2.1.2 Conducting properties of a conjugated system . . . . . 9

2.2 Electronic transition under absorption . . . . . 10

2.2.1 Transition dipole moment and oscillator strength . . . . . 10

2.2.2 Allowed and forbidden transitions . . . . . 12

2.2.3 Franck-Condon process . . . . . 13

2.2.4 Exciton model under intermolecular interaction . . . . . 16

2.3 De-excitation processes and dynamics . . . . . 22

2.3.1 Non-radiative relaxations and photoluminescence . . . . . 22

2.3.2 Exciton dynamics and rate equations . . . . . 23

2.3.3 Einstein relation and emission rate . . . . . 25

2.3.4 Fluorescence anisotropy of polarisation . . . . . 27

2.4 Excitation energy transfer . . . . . 30

2.4.1 Förster resonance energy transfer (FRET) . . . . . 32

**3 Experimental Methods** **37**

3.1 Generation of femtosecond pulses . . . . . 38

3.2 Non-linear optics in PLUCS . . . . . 39

3.3 Experimental setup of PLUCS . . . . . 42

3.4 Operating principle of TCSPC . . . . . 45
3.5 Electronics in TCSPC . . . . . 47

**4 Full Delocalisation of the Absorbing Excited State in Porphyrin Nanorings 49**
4.1 Introduction and Background . . . . . 49
4.2 Sample Preparation and Experiments . . . . . 51
4.2.1 Synthesis and characterisation of porphyrins . . . . . 51
4.2.2 Time-resolved photoluminescence spectroscopy . . . . . 51
4.2.3 PL Intensity Transients . . . . . 53
4.2.4 Quantum Yield . . . . . 53
4.3 Results and Discussion . . . . . 54
4.3.1 Anisotropy of PL Polarisation of Nanorings . . . . . 56
4.3.2 Radiative Transition Rates of Nanorings . . . . . 62
4.4 Conclusion . . . . . 66

**5 Excitation Energy Transfer in Organic Self-Assembled Nanoparticles of Amphiphilic Monomers with Targeting Ligands 69**
5.1 Introduction and Background . . . . . 69
5.2 Samples and Experimental Details . . . . . 71
5.2.1 Characterization of Amphiphilic Monomers . . . . . 71
5.2.2 Introduction to Conconavalin A . . . . . 73
5.2.3 Sample Preparation . . . . . 73
5.2.4 Measurement of Transient Photoluminescence Decay . . . . . 74
5.3 Results and Discussion . . . . . 75
5.3.1 Transient Fluorescent Characteristics of Nanoparticles . . . . . 75
5.3.2 Energy Transfer between Nanoparticles and Attached Acceptors . . . 79
5.4 Conclusion . . . . . 89

**6 Conclusions and Outlook 91**

**Bibliography 95**

# Publications

J. K. Sprafke, D. V. Kondratuk, M. Wykes, A. L. Thompson, M. Hoffmann, R. Drevinskas, W.-H. Chen, C. K. Yong, J. Karnbratt, J. E. Bullock, M. Malfois, M. R. Wasielewski, B. Albinsson, L. M. Herz, D. Zigmantas, D. Beljonne, and H. L. Anderson. Belt-Shaped $\pi$-Systems: Relating Geometry to Electronic Structure in a Six-Porphyrin Nanoring. *Journal of the American Chemical Society*, **133**:17262-17273, 2011.

C. K. Yong, W.-H. Chen, D. V. Kondratuk, P. Parkinson, A. Stannard, A. Summerfield, J. K. Sprafke, M. C. O'Sullivan, P. H. Beton, H. L. Anderson, and L. M. Herz. Spatially Coherent Excitation in Synthetic Light-Harvesting Nanorings. *Manuscript submitted.*

W.-H. Chen, C. K. Yong, I. Fischer, A. Kaeser, A. P. H. J. Schenning, and L. M. Herz. Excitation Energy Transfer in Organic Self-Assembled Nanoparticles of Amphiphilic Monomers with Targeting Ligands. *Manuscript in preparation.*

# Prize

William R Miller Postgraduate Award
*St Edmund Hall, University of Oxford, 2011-2012.*

# Chapter 1

# Introduction

## 1.1 Introduction

Organic polymers, which usually have low intrinsic electrical conductivity, were not previously considered to be a conducting materials until a breakthrough occurred in 1977, namely the discovery that doped polyacetylene has a high electrical conductivity [1]. After the milestone of the research into electroluminescence in poly(phenylenevinylene) in 1990 [2], electronic devices based on organic semiconductors have enabled great achievements in applications including organic photovoltaics (OPVs) [3, 4], light emitting diodes (OLEDs) [5, 6], field-effect transistors (OFETs) [7] and biological and chemical sensors [8]. The advantages of these $\pi$-conjugated materials used in organic semiconductor electronics are that bandgap engineering allows the tunability of their light absorption and emission and exciton transport properties [2]; the low-cost printable solution process for large-area roll-to-roll device fabrication especially lends an impetus to speed up the development of plastic electronics [5]. Although considerable research efforts have been made to explore the optoelectrical characteristics of these organic $\pi$-conjugated materials over the last decades, and some organic devices have been successfully commercialised, their fundamental physics are not completely understood. This is because the uncontrollable morphology resulting from the manufacturing process produces complicated intra- and inter-molecular interactions [9].

Ordered supramolecular assembly will enable insights into ways to improve carrier mobil-

ity and to reduce exciton loss. The bottom-up processing of self-assembled supramolecules is an alternative approach to building an organic device, which is in contrast to the traditional top-down method and is able to assemble elaborate nanoscale building blocks by careful design of their chemical structures [10]. To gain an insight into methods to optimise device efficiency, scientists have been inspired by processes occurring in nature. In the application of solar cells, the photosynthesis process in plants and some specific bacteria is intriguing; for example, in purple photosynthetic bacteria, solar energy is light-harvested with almost 100 % quantum efficiency over a distance of 20-100 nm by its pigment-protein complexes, formed by porphyrin derivatives, and excitation energy finally arrives at a reaction centre for further chemical production [11]. This has motivated many researchers to synthesise organic biomimetic macrocycles and attempt to understand the underlying photophysics in the design of nature, so that an OPV with ultra-high efficiency can be achieved [12–15].

Moreover, organic nanomaterial also plays an important role in medical applications for disease and cancer research; for instance, bio-imaging [16], sensing [17] and drug delivery [18]. Although quantum dots (QDs) exhibit excellent photoluminescence properties [19–21], their core is formed by noble metals or inorganic semiconductors that may lead to potential bio-toxicity in the human body [22]. Highly-emissive fluorescent $\pi$-conjugated nanoparticles (NPs) combining the advantages of inorganic QDs and organic dyes are adopted to solve the toxicity problem, which can be created by organic polymers or oligomers with self-assembled processes in solution [23]. Furthermore, functional groups covalently or non-covalently decorated on the surface of nanoparticles can tune their binding affinity to specific targets to realise the auto navigation, which is able to direct the nanoparticles to the targets *in vivo* or *in vitro* [24]. Thus, an understanding of fundamental physical electronic dynamics can help to improve the optical performance of the nanoparticles.

The relaxation and transfer of the excited energy usually occurs on an ultrafast timescale, so the spectroscopic information determined by these physical processes can be studied by time-resolved photoluminescence experimental techniques based on the femtosecond laser system, which includes photoluminescence up-conversion spectroscopy (PLUCS) and a Time-

Correlated Single Photon Counting (TCSPC) system with a time-resolution of hundreds of femtoseconds and hundreds of picoseconds, respectively. Therefore, ultrafast spectroscopy provides the opportunity to solve the technical and biological issues relevant to alternative energy generation and medical applications.

## 1.2 Thesis outline

This thesis aims to investigate the issues concerned with excitation energy transfer in the organic biomimetic and biosensing systems referred to above by ultrafast photoluminescence spectroscopy. The rest of the thesis is structured as follows:

In Chapter 2, the electronic processes occurring in light-perturbed organic material are introduced. If the transition is allowed, the absorption of a photon at a particular wavelength renders the electron excited to a higher energy level, whilst still being attracted to the hole in the original location where the electron used to be. Subsequently, various alternative pathways of relaxation processes follow, which release the absorbed energy by radiative emission of photons or non-radiative phonon vibration to achieve thermal equilibrium again. In fact, after a brief time interval after the excitation within the lifetime, excited energy is able to be transferred to adjacent molecules coherently or incoherently under appropriate conditions.

Chapter 3 describes the experimental methods used to investigate photophysics in nanomaterials when excited by a femtosecond laser pulse with a specific wavelength. The generation of the femtosecond light; and the fundamental principles of optical-gating and electrical-gating time-resolved photoluminescence techniques based on the Ti:Sapphire mode-locking system are explained. The experimental setup of the photoluminescence up-conversion spectroscopy (PLUCS) and Time-Correlated Single Photon Counting (TCSPC) system are then discussed in detail.

The degree of delocalisation occurring on an ultrafast timescale among different sizes of fully $\pi$-conjugated porphyrin nanorings are investigated in Chapter 4. It is found that

in the nanoring, the excited-state wavefunction is fully delocalised even in the case of the largest with a diameter of ∼10 nm. Such spatial coherent excitations are supported by the initial PL anisotropy of polarisation smaller than 0.1. The full delocalisation of the absorbing excited state may be helpful for forming the charge-separated state in organic devices [25, 26]. In fact, due to their symmetrical structures, transitions involving the lowest electronic state of the nanorings are theoretically forbidden, and no emission is expected. However, the deviation from the ideal ring-like symmetry of the nanoring structures in the solution may relax this constraint. The static distortion, which dominates the break of the circular symmetry in the flexible larger nanorings, dramatically raises the radiative decay rate when the unit of porphyrins in the nanoring is increased from 6 to 24. On the other hand, the dynamic distortion, which dominates in the smaller rings, can be explained by the Herzberg-Teller coupling theory [27–29]. The spatial coherence of the excited state of the synthesised fully $\pi$-conjugated porphyrin nanorings is remarkably robust against disorder-induced weakening of the electronic coupling between porphyrin units, which supasses their counterparts in natural light-harvesting systems.

In Chapter 5, monotransfer and heterotransfer of excitons in organic nanoparticles formed of amphiphilic coil-rod-coil monomers and between protein-carried fluorescent dyes are investigated. There are four different locations on the fluorene pairs linked by a benzothiazole allowing synthesis with hydrophobic or hydrophilic side chains, resulting in the formation of self-assembled nanoparticles in water. On one of the hydrophilic tails at the Amp1-B monomer end, an $\alpha$-D-mannosyl group can be attached and used as a binding site for proteins (Concanavalin A, ConA), which are the carriers for fluorescent dyes (Alexa Fluor 633, AF633). The transient PL spectra measurements of nanoparticles formed by higher molar fraction of mannose and formed by Amp3-B monomers both exhibit larger red-shifts of average emission energy of excitons in the 8 ns observation window, suggesting that excitons in these two cases migrate efficiently towards the sites with lower energy because of energetic cascades. The study of Förster resonance energy transfer from the excitons on chromophores in nanoparticles to ConA/AF633 acceptors further prove that Amp3-B/Amp1-B-mannose NPs are able to establish more energetically favorable routes for excitons towards the sur-

face than that in Amp1-B/Amp1-B-mannose NPs; therefore, the energy transfer rates are increased owing to more excitons being channelled to the Amp3-B monomers on the interface between nanoparticles and water. However, an increase in the amount of Amp3-B monomers leads to a decrease in that of Amp1-B-mannose in the nanoparticles; hence, optimisation of the molar ratios of these two monomers is crucial to achieve the highest energy transfer rate in the system, which leads to a high signal-to-noise ConA/AF633 emission. These findings explore the fundamental photophysics in new carbohydrate-coated organic amphiphilic nanoparticles, which exhibit potential to be used in biological sensing applications.

Finally, Chapter 6 provides a summary of the research in this thesis, together with an outlook for future experiments that is based on the experimental results presented here.

# Chapter 2

# Electronic Processes in Organic Conjugated Materials

## 2.1 Basic concepts of conjugated materials

The electronic properties of electrons surrounding a nucleus are usually studied using a quantum mechanical approach, where the wave packet of electrons can be described by a linear combination of the harmonic oscillators of electrons on individual atoms. For a single-electron atom, the wavefunction of the electron for a time-independent Schrödinger equation can be written by a product of $R_{n,l}(r)$, $\Theta_{l,m_l}(\theta)$ and $\Phi_{m_l}(\phi)$ using separation of variables in polar coordinates:

$$\psi_{n,l,m_l}(r,\theta,\phi) = R_{n,l}(r)\Theta_{l,m_l}(\theta)\Phi_{m_l}(\phi), \tag{2.1}$$

where $n$, $l$ and $m_l$ are the principle, azimutal and magnetic quantum numbers, respectively. The eigenvalues of a single electron system mainly correspond to $n$, whilst the eigenfunctions are decided by all of the three quantum numbers $n$, $l$ and $m_l$, which form a complete set (atomic orbitals, AOs) and can be adopted to establish wavefunctions in another, more complicated system with the same coordinates by performing their linear combination. It is noted that the orbital quantum numbers $l$ are also termed $s$, $p$, $d$ and $f$ orbitals corresponding

to $l = 0$, $l = 1$, $l = 2$ and $l = 3$, respectively.

### 2.1.1 Hybrid orbital theory

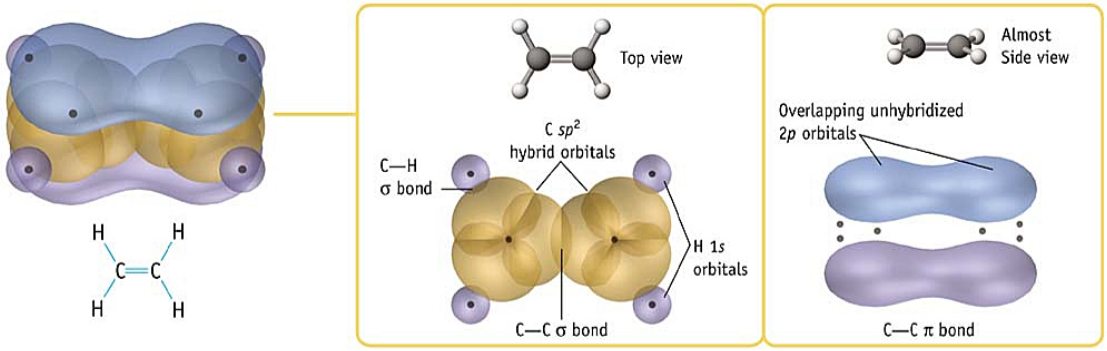


Figure 2.1: Schematic diagram of the chemical structure and orbital bonding of ethylene, $C_4H_4$. Taken from [30].

For qualitative calculation, the hybrid orbital theory has been proposed to explain the bonding phenomenon between atoms, in which mixed atomic orbitals are rewritten as new hybrid atomic orbitals (HAOs) [31, 32]. For instance, in a simple molecular system, ethylene, two adjacent triangular lobes of $sp^2$ in a plane, which is hybridised originally from one $2s$ and two $2p$ orbitals between carbon-carbon bond formation, will be hybridised again and split into a molecular orbital (MO) of in-phase $\sigma$ bonding and an out-of-phase $\sigma^*$ bonding according to the Pauli exclusion principle, as shown in Figure 2.1. The rest of the $2p_z$ orbitals, which are perpendicular to the plane of $sp^2$ hybridisation, will be hybridised and create new bonding ($\psi_\pi$) and antibonding ($\psi_\pi^*$) orbitals, and they can be written as:

$$\psi_\pi \approx \frac{1}{\sqrt{2}}\psi_{2p_z(a)} + \frac{1}{\sqrt{2}}\psi_{2p_z(b)}, \tag{2.2}$$

$$\psi_{\pi^*} \approx \frac{1}{\sqrt{2}}\psi_{2p_z(a)} - \frac{1}{\sqrt{2}}\psi_{2p_z(b)}, \tag{2.3}$$

where $\psi_{2p_z(a)}$ and $\psi_{2p_z(b)}$ represent the $2p_z$ orbitals on each carbon atom respectively. Electrons in $\pi$ bonds, which are weakly bound and coupled to one another to build a one-dimensional delocalised electron band, are responsible for the main chemical characteristics

of the system, whilst electrons in $\sigma$ bond are constrained and build its backbone. In the same way, delocalised $\pi$ orbitals of N conjugated carbons in the system can be extended and written by a linear combination of individual $2p_z$ orbitals as

$$\psi_{\pi,k} \approx \sum_{n=1}^{N} C_n^k \psi_{2p_z(n)}, \tag{2.4}$$

where $\psi_{2p_z(n)}$ is the $2p_z$ orbital on the $n$th carbon atom, and $C_n^k$ is the factor deciding the contribution of $\psi_{2p_z(n)}$ to the total orbital $\psi_{\pi,k}$; $k$ is the energy level in the hybridised orbital.

For the approximation of eigenvalues of a $\pi$-conjugated hydrocarbon system, the Hückel molecular orbital (HMO) method, developed by E. Hückel [33], which is similar to the tight-binding model [34, 34], is also based on the concept that $\pi$ MOs are a linear combination of individual $2p_z$ HAO. It is most suitable for coplanar hydrocarbon molecules linked by alternating single and double carbon-carbon bonds, but the approach is also applicable to various large systems. In a conjugated polymer with N carbon atoms on the backbone, if there are N $\pi$ orbitals, they will split into N/2 $\pi$ subbands and N/2 $\pi^*$ subbands [33].

### 2.1.2 Conducting properties of a conjugated system

If a conjugated polymer, for example, polyacetylene (PA), has an equally spaced carbon-carbon distance with a unit cell length of $a$ without distortion and bending, where each of the $\pi$ orbital contains only one electron, the one-dimensional band is supposed to be half-filled and demonstrate metallic conducting characteristics. However, formation of such a 1-D metal usually has low stability, so dimerisation results from bond-length alternation (BLA) [35, 36]. Alternating single and double bonds will lead to a doubled length of a unit cell, $2a$, and the energy diagram in the momentum space is modified to achieve a lower total energy by forming an energy gap, which is termed the Peierls band gap, as shown in Figure 2.2. Generally, the BLA is small when the conjugation is spatially ordered, such as in 2-D metals and graphene, which demonstrate metallic conductivity [9]. On the contrary, the BLA is large in a less ordered backbone of conjugated polymers. Depending on the size of the energy

gap, an imperfect conjugated polymer can possess semiconducting or insulating properties.

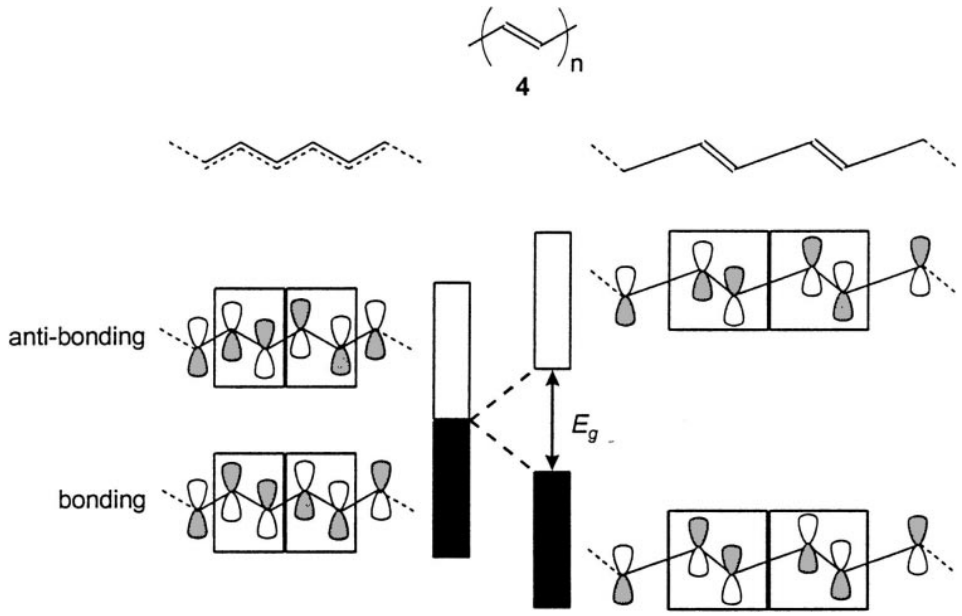


Figure 2.2: Illustration of the formation of the Peierls gap by bond-length alternation (PLA) in *trans*-polyacetylene 4. Taken from [37].

## 2.2 Electronic transition under absorption

### 2.2.1 Transition dipole moment and oscillator strength

When additional perturbations are added into a molecular system they can be described by a classical approach, whilst the states of electrons that absorb the energy of the perturbation can still be treated quantum-mechanically, as described in the previous sections. The transition dipole moment $\boldsymbol{\mu}$ is the oscillating electric dipole moment for the transition of electrons from an initial state to a final state [38]. Its direction represents the polarisation of a system and characterises how the system will interact with an added perturbation, which is usually a polarised electromagnetic wave. Therefore, the strength of the transition due to the absorption of light can be defined by a dimensionless factor termed dipole strength, or a modified factor termed oscillator strength [38].

A dipole operator, $\hat{\mu}$, is introduced by the time-dependent perturbation theory to the original system. Thus, the modified Hamiltonian operator, $\hat{H}$, can be written as [39]

$$\hat{H}(t) = -\mathbf{E}(t) \cdot \hat{\mu}, \tag{2.5}$$

where $\mathbf{E}(t)$ is the linearly-polarised oscillating electric field. Equation 2.5 can be written by Taylor series approximation at the origin of the coordinates, if the polarisation of the light is in the direction of the $z$ axis: [40]

$$\begin{aligned}\hat{H}(x,y,z,t) &= -e\mathbf{E}(t) \cdot \mathbf{r} \\ &= -ez(t) \left\{ |E(t)|_{x,y=0} + \left[ x \left( \frac{\partial |E(t)|}{\partial x} \right)_{x,y=0} + y \left( \frac{\partial |E(t)|}{\partial y} \right)_{x,y=0} \right] + \dots \right\},\end{aligned} \tag{2.6}$$

in which the dominating term represents the dipole interaction, and the rest of the terms are higher-order interactions that are relatively small and can be neglected. Assuming that in a 2-level system, the wavefunction $\psi'$ in the perturbed system can be expressed as a linear combination of the wavefunctions, $\psi_1$ and $\psi_2$ in an unperturbed version:

$$\psi' = C_1\psi_1 + C_2\psi_2, \tag{2.7}$$

where $C_n (n = 1, 2)$ are time-dependent coefficients. Conceptually, $\psi_1$ and $\psi_2$ present that the electrons are in ground and excited states, respectively, and therefore $\psi_2$ locates at a higher energy state than $\psi_1$, and $E_2$ is larger than $E_1$. $C_2$ is the time-dependent ratio of the electrons in the ground state being promoted to the excited state after the excitation. Assume $N_{total}$ is the density of electrons originally in the ground state, and $t'$ is the time interval after the excitation. According to Fermi's golden rule [41, 42], the total absorption probability for promotion of electrons from $\psi_1$ to $\psi_2$ per unit time over all oscillating frequencies covered

by light, $|C_2(t')|^2 N_{total}/t'$, is given by:

$$\begin{aligned} |C_2(t')|^2 N_{total}/t' &= \frac{1}{t'} \int_0^\infty N_{total} C_2^*(t',\nu) C_2(t',\nu) \rho_\nu(\nu) d\nu \\ &= N_{total}(\mathbf{E}_0 \cdot \langle \psi_2 | \hat{\mu} | \psi_1 \rangle)^2 \rho_\nu(\nu_0)/\hbar^2 \\ &= N_{total}(\mathbf{E}_0 \cdot \boldsymbol{\mu}_{21})^2 \rho_\nu(\nu_0)/\hbar^2, \end{aligned} \tag{2.8}$$

which is also the transition rate of electrons from $\psi_1$ to $\psi_2$. Here $\rho_\nu$ is the density of the oscillation states (number of modes of the oscillation), $\nu_0 = (E_2 - E_1)/h$ is the resonance condition, and $\boldsymbol{\mu}_{21} \equiv \langle \psi_2 | \hat{\mu} | \psi_1 \rangle$ is the transition dipole moment. $\boldsymbol{\mu}_{21}$ describes the properties of the transition from $\psi_1$ to $\psi_2$, and it can be depicted as a vector on the nuclear coordinates. The transition probability due to polarised light is proportional to the square of the dot product between $\boldsymbol{\mu}_{21}$ and the oscillating electric field.

The dipole strength is defined as $D_{21} = |\boldsymbol{\mu}_{21}|^2$ [43], which stands for the strength to make a certain transition. The absorption strength can also be connected by the oscillator strength, $f_{21}$, which is defined as: [43]

$$f_{21} = \frac{8\pi^2 m_e \nu}{3e^2 h} D_{21}, \tag{2.9}$$

where $m_e$ is the electron mass. It is noted that although the direction of the vector of $\boldsymbol{\mu}_{21}$ does not influence its absorption strength in a simple 2-orbital model, the electronic transition rate is calculated by a vector combination of transition dipole moments of various units in a complex molecular system [44], which will be discussed in Chapter 4.

### 2.2.2 Allowed and forbidden transitions

By calculating the dipole strength, it is possible to determine if a specific absorption transition is allowed or forbidden, where the symmetry of molecular orbitals plays an important

role. Due to the definition of a transition dipole moment, it is written as:

$$\begin{aligned}\boldsymbol{\mu}_{21} &= \langle\psi_2|\hat{\mu}|\psi_1\rangle \\ &= e\langle\psi_2|\mathbf{r}|\psi_1\rangle \\ &\equiv e\int \psi_2^*\mathbf{r}\psi_1 d\Delta,\end{aligned} \tag{2.10}$$

where $d\Delta$ is the volume element around $\mathbf{r}$. $\psi_2^*\mathbf{r}\psi_1$ must have symmetric components to be nonzero for an allowed transition [39]. It is generally easier to calculate with the help of group theory, which defines the molecular configuration structures into various group points [45]. Nevertheless, the symmetry-forbidden transitions are sometimes observable due to vibrational coupling, which breaks the symmetry of the molecular orbitals by molecular vibrations, although their oscillator strengths will be relatively small. On the other hand, except for the symmetry-forbidden, spin-forbidden also plays an important role in electronic transitions, which is based on the rule that the angular momentum must be conserved, i.e. the multiplicities of two transition states must be the same. However, similarly, singlet–triplet transitions can sometimes be seen in the experiment because of weak interaction by the spin-orbit coupling in the molecular system [46].

### 2.2.3 Franck-Condon process

In fact, the complete wavefunction for describing a molecular system consists of contributions from not only the electrons but also nuclei. Thus, the Hamiltonian for the electrons also includes the influence from the nuclei, and can be written as a product of electronic and nuclear wavefunctions. After the Schrödinger equation with the complete Hamiltonian is solved, we obtain:

$$\Psi_{complete} = \sum_n \sum_k \psi_n \chi_{k(n)}, \tag{2.11}$$

where $\psi_n$ is the electronic wavefunctions at electronic level $n$ depending on the electron and nuclei coordinates, and $\chi_{k(n)}$ is the nuclear wavefunctions at vibronic state $k$ corresponding

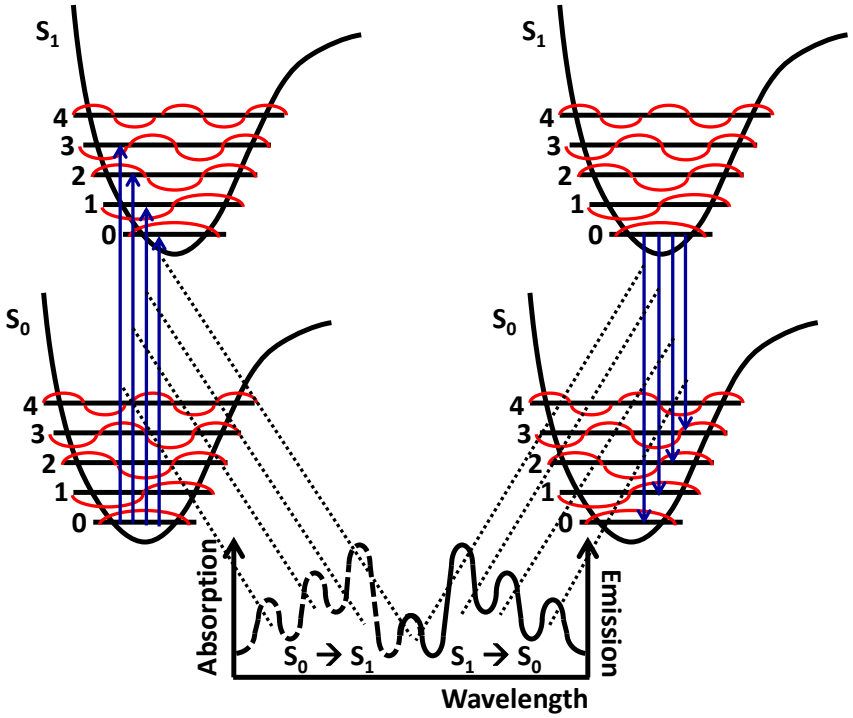


Figure 2.3: Schematic diagram to represent the Franck-Condon process. Simplified potential energy curves with discrete levels show the $S_0$ and $S_1$ vibronic states in a conjugated material. The mirror image with a Stoke's shift of the absorption and emission spectra resulting from the transition of absorption is from the lowest vibronic state of $S_0$ and emission occurs at the lowest vibronic state of $S_1$ after a quick relaxation of the excited energy, according to Kasha's rule.

to each electronic level $n$. By the Born-Oppenheimer approximation, Equation 2.11 can be simplified by the dominating term [47–49]:

$$\Psi_{complete} = \psi_n \chi_{k(n)}, \tag{2.12}$$

which means that the electron cloud changes its distribution immediately according to the change of the nuclear location in the vibrational coordinate, because the mass of the nuclei is much heavier than that of electrons. On the other hand, it also suggests that the nuclear motion is almost frozen during the electronic transition (vertical transition); and, subsequently, the change of the charge distribution of electrons leads to nuclear vibration, finally achieving thermal equilibrium. For a system containing one electron and one nucleus, the dipole operator is composed of an electronic and a nuclear term, $\hat{\mu} = \hat{\mu}_{electron} + \hat{\mu}_{nucleus}$,

and then the transition dipole moment from the vibronic state $n$ at electronic level 1 to the vibronic state $m$ at electronic level 2 is [34, 50]:

$$\begin{aligned}\boldsymbol{\mu}_{21,mn} &= \langle\psi_2\chi_m|\hat{\mu}_{electron}|\psi_1\chi_n\rangle + \langle\psi_2\chi_m|\hat{\mu}_{nucleus}|\psi_1\chi_n\rangle \\ &= \langle\psi_2\chi_m|\hat{\mu}_{electron}|\psi_1\chi_n\rangle \\ &= \langle\chi_m|\chi_n\langle\psi_2|\hat{\mu}_{electron}|\psi_1\rangle\rangle \\ &= \langle\chi_m|\chi_n\boldsymbol{\mu}_{21}^{'}\rangle \\ &= \langle\chi_m|\chi_n\rangle\overline{\boldsymbol{\mu}_{21}^{'}},\end{aligned} \tag{2.13}$$

where $\boldsymbol{\mu}_{21}^{'}$ is the electronic transition dipole moment on the nuclear coordinate and it is assumed that $\boldsymbol{\mu}_{21}^{'}$ is a constant in the range where $\chi_n$ and $\chi_m$ are non-zero; $\overline{\boldsymbol{\mu}_{21}^{'}}$ is the average of the electronic transition dipole moment. It is noted that Equation 2.13 is derived by Condon approximation. Obviously, the dipole strength is proportional to $|\langle\chi_m|\chi_n\rangle|^2$, which is termed the Franck-Condon factor. The Franck-Condon factor, describing various vibronic transitions, can be approximated by the wavefunctions of a one-dimensional harmonic oscillator. If the difference in the bond length in the excited and ground states is $l_{ex}$ – $l_{gr}$, the coupling strength by excitation, $S$, is defined as [51, 52]:

$$S = \frac{m_v\pi\nu}{\hbar}(l_{ex} - l_{gr})^2, \tag{2.14}$$

which is also termed the Huang-Rhys factor. Here $m_v$ is the mass of the vibrating atoms; $l_{ex}$ and $l_{gr}$ are the bond lengths in the excited and ground states, respectively. The Franck-Condon factor from the lowest ground vibronic state to one of the excited vibronic states is shown as follows [53]:

$$|\langle\chi_k|\chi_0\rangle|^2 = \frac{S^k exp(-S)}{k!}, \tag{2.15}$$

where $\chi_k$ is the $k$th excited vibronic state and $\chi_0$ is the lowest ground vibronic state. If there is more than one atom in a molecular system, the overall Huang-Rhys factor for a vibronic transition is the product of the individual factor of each atom. According to the

Boltzmann distribution at room temperature, most of the population tends to occupy the lowest vibronic state in the ground state. Therefore, the absorption strength is dominated by the electronic transition from the bottom of the ground vibronic state to the bottom of the excited state (0–0 transition), unless the solvent effect is strong, leading to a shift of the excited-state potential energy in the vibrational coordinate. The Franck-Condon process with a shifted potential energy is shown in Figure 2.3 [54], where the 0–1 vertical transition has the largest dipole strength, and the fast relaxation of the excited energy leads to a shift (Stokes shift) of the mirror image between the absorption and emission spectra. In addition, the vibronic transitions and solvent effect will result in homogeneous and inhomogeneous broadening of the absorption spectrum, respectively.

### 2.2.4 Exciton model under intermolecular interaction

When there are more than two molecular systems, which are close enough to form aggregates or polymers containing repeated units of chromophores, the strong dipolar interaction between molecules will result in the splitting of excited energy levels and lead to variations in the spectroscopic properties compared with that of the individual molecule. This phenomenon can be explained by the exciton model, which describes the behaviour of excitation energy as a quasi-particle moving almost freely among more than one unit of molecules in a system [55, 56]. The excitons are no longer localised on one single molecule; on the contrary, the electronic waves oscillate and delocalise over several different units of molecules, so it cannot be distinguished which specific molecule is excited [39]. The physical meaning of an exciton can be depicted by an electron being excited to one of the excited states is still attracted to the hole produced at its original location when it transports. In conjugated materials, Frenkel excitons are usually used to describe a molecular system [57, 58], whilst Wannier excitons have a much longer distance between the electron and the hole that are attracted to each other and more suitably describe inorganic materials [59, 60]. Here, an electronically coupled dimer is used as an example to explain the theory of the formation of excitonic states. If there is no orbital overlapping in the dimer, where two molecules are

separated spatially, it is feasible to write the wavefunctions in the dimer as a linear combination of wavefunctions on individual molecules. The simple derivation is shown as follows [55, 61]. The wavefunction of a dimer in the ground state is given as:

$$\Psi_{ground} = \phi_{a1}\phi_{b1}, \tag{2.16}$$

where the notation of $a$ and $b$ means the individual wavefunctions in molecules $a$ and $b$, respectively; the notation of 1 and 2 represent the wavefunctions in the ground state and the excited state, respectively. The wavefunction of a dimer in the excited state is written as a linear combination of two states: (1) $\psi_A$, the electron in molecule $a$ is promoted to the excited level, whilst the electron in molecule $b$ is kept at the ground level; (2) $\psi_B$, the electron in molecule $b$ is promoted to the excited level, while the electron in molecule $a$ stays at the ground level. Therefore, the wavefunction of a dimer in the excited state is read:

$$\Psi_{excited} = C_A\psi_A + C_B\psi_B = C_A\phi_{a2}\phi_{b1} + C_B\phi_{a1}\phi_{b2}, \tag{2.17}$$

where $C_A$ and $C_B$ are the coefficients for $\psi_A$ and $\psi_B$, respectively; $\psi_A$ is written as $\phi_{a2}\phi_{b1}$, and $\psi_B$ is $\phi_{a1}\phi_{b2}$. The Hamiltonian for the dimer, including the Coulombic interaction between two molecules, is written as:

$$\hat{H}_a + \hat{H}_b + \hat{H}_{inter}, \tag{2.18}$$

where $\hat{H}_a$ and $\hat{H}_b$ are the Hamiltonian of the isolated molecules $a$ and $b$, respectively; $\hat{H}_{inter}$ is the Hamiltonian of Coulombic interaction. Therefore, the corresponding ground-state energy, $E_{ground}$, is:

$$\begin{aligned} E_{ground} &= \langle\phi_{a1}\phi_{b1}|\hat{H}_a + \hat{H}_b + \hat{H}_{inter}|\phi_{a1}\phi_{b1}\rangle \\ &= E_{a1} + E_{b1} + \langle\phi_{a1}\phi_{b1}|\hat{H}_{inter}|\phi_{a1}\phi_{b1}\rangle, \end{aligned} \tag{2.19}$$

where $E_{a1}$ and $E_{b1}$ are the ground-state energy in the isolated molecule $a$ and $b$, respectively.

It is noted that $\langle\phi_{a1}\phi_{b1}|\hat{H}_{inter}|\phi_{a1}\phi_{b1}\rangle$ can be ignored if molecule $a$ and $b$ are neutral. Next, $E_{excited}$ can be written as:

$$\begin{aligned} E_{excited} &= \langle C_A\psi_A + C_B\psi_B|\hat{H}_a + \hat{H}_b + \hat{H}_{inter}|C_A\psi_A + C_B\psi_B\rangle \\ &= |C_A|^2(E_{a2} + E_{b1}) + |C_B|^2(E_{a1} + E_{b2}) + \langle C_A\psi_A + C_B\psi_B|\hat{H}_{inter}|C_A\psi_A + C_B\psi_B\rangle. \end{aligned} \tag{2.20}$$

It is noted that the eigenstates $\psi_A$ and $\psi_B$ are not stationary states, because oscillation occurs between the two molecules in the system. New stationary eigenstates can be obtained by solving the time-independent Schrödinger equation of the system of a dimer, and it is written as:

$$(\hat{H}_a + \hat{H}_b + \hat{H}_{inter})(C_A\psi_A + C_B\psi_B) = E_{excited}(C_A\psi_A + C_B\psi_B). \tag{2.21}$$

For clarification, define $H_{AA}$, $H_{BB}$, $H_{AB}$ and $H_{BA}$ as:

$$H_{AA} = \langle\psi_A|\hat{H}_a|\psi_A\rangle + \langle\psi_A|\hat{H}_{inter}|\psi_A\rangle = E_{a2} + E_{b1} + \langle\psi_A|\hat{H}_{inter}|\psi_A\rangle; \tag{2.22}$$

$$H_{BB} = \langle\psi_B|\hat{H}_b|\psi_B\rangle + \langle\psi_B|\hat{H}_{inter}|\psi_B\rangle = E_{a1} + E_{b2} + \langle\psi_B|\hat{H}_{inter}|\psi_B\rangle; \tag{2.23}$$

$$H_{AB} = \langle\psi_A|\hat{H}_{inter}|\psi_B\rangle; \tag{2.24}$$

$$H_{BA} = \langle\psi_B|\hat{H}_{inter}|\psi_A\rangle. \tag{2.25}$$

$H_{AB} = H_{BA}$ if these matrices are composed of real numbers. Subsequently, multiply both sides of the equation by either $\psi_A$ or $\psi_B$ and integrate it over the whole space. Two equations are obtained:

$$C_AH_{AA} + C_BH_{AB} = C_AE_{excited} \tag{2.26}$$

$$C_AH_{BA} + C_BH_{BB} = C_BE_{excited}, \tag{2.27}$$

which can be written as:

$$C_A(H_{AA} - E_{excited}) + C_B H_{AB} = 0 \tag{2.28}$$

$$C_A H_{BA} + C_B(H_{BB} - E_{excited}) = 0, \tag{2.29}$$

Non-trivial $C_A$ and $C_B$ can only be obtained when the determinant is equal to zero:

$$\begin{vmatrix} H_{AA} - E_{excited} & H_{AB} \\ H_{BA} & H_{BB} - E_{excited} \end{vmatrix} = 0.$$

Assume that $H_{AA} \approx H_{BB}$, two possible solutions of $E_{excited}$, denoted as $E_{excited2}$ and $E_{excited1}$, are obtained and shown as follows:

$$E_{excited1} = (H_{AA} + H_{BB})/2 - H_{AB}; \tag{2.30}$$

$$E_{excited2} = (H_{AA} + H_{BB})/2 + H_{AB}. \tag{2.31}$$

Therefore, it is obvious that the Coulombic interaction between the two molecules in the dimer leads to the splitting of the excited-state energy into two levels by an amount of $2H_{AB}$, which is termed exciton splitting. If the difference between excitation energies in isolated molecules is not zero, i.e., $H_{AA} \not\approx H_{BB}$, and it is much larger than the Coulombic interaction in the dimer, the excitation energy will be found to be localised on either one of the molecules, rather than being delocalised over both. Next, the solutions of $E_{excited1}$ and $E_{excited2}$ can be put back to Equation 2.28 and Equation 2.29 to find the coefficients, $C_A$ and $C_B$, and then the two wavefunctions, $\Psi_{excited1}$ and $\Psi_{excited2}$, are obtained:

$$\Psi_{excited1} = \frac{\sqrt{2}}{2}(\psi_A - \psi_B), \tag{2.32}$$

and

$$\Psi_{excited2} = \frac{\sqrt{2}}{2}(\psi_A + \psi_B). \tag{2.33}$$

The absorption strength of the dimer is associated with its dipole strength, which can be calculated from the dipolar coupling using the definition used previously. Thus, one of the transition dipole moments of the electronic transitions from the ground state to the two splitted excited-state levels can be written as:

$$\begin{aligned}
\boldsymbol{\mu}_{excited2} &= \langle \psi_{excited2} | \hat{\mu}_{excited} | \psi_{ground} \rangle \\
&= \langle \psi_{excited2} | \hat{\mu}_a + \hat{\mu}_b | \psi_{ground} \rangle \\
&= \langle C_A \phi_{a2} \phi_{b1} + C_B \phi_{a1} \phi_{b2} | \hat{\mu}_a + \hat{\mu}_b | \phi_{a1} \phi_{b1} \rangle \\
&= C_{A2} \langle \phi_{a2} | \hat{\mu}_a | \phi_{a1} \rangle + C_{B2} \langle \phi_{b2} | \hat{\mu}_b | \phi_{b1} \rangle \\
&= C_{A2} \boldsymbol{\mu}_a + C_{B2} \boldsymbol{\mu}_b \\
&= \frac{\sqrt{2}}{2} \boldsymbol{\mu}_a + \frac{\sqrt{2}}{2} \boldsymbol{\mu}_b
\end{aligned} \tag{2.34}$$

Similarly, $\boldsymbol{\mu}_{excited1}$ is found to be:

$$\begin{aligned}
\boldsymbol{\mu}_{excited1} &= C_{A1} \boldsymbol{\mu}_a + C_{B1} \boldsymbol{\mu}_b \\
&= \frac{\sqrt{2}}{2} \boldsymbol{\mu}_a - \frac{\sqrt{2}}{2} \boldsymbol{\mu}_b .
\end{aligned} \tag{2.35}$$

Here, $\hat{\mu}_{excited} = \hat{\mu}_a + \hat{\mu}_b$; $C_{A1}$ and $C_{B1}$, $C_{A2}$ and $C_{B2}$ are the corresponding coefficients of $\Psi_{excited1}$ and $\Psi_{excited2}$, respectively. The dipole strength is then calculated easily as follows:

$$\begin{aligned}
D_{excited2} &= \left( \frac{\sqrt{2}}{2} \boldsymbol{\mu}_a + \frac{\sqrt{2}}{2} \boldsymbol{\mu}_b \right) \times \left( \frac{\sqrt{2}}{2} \boldsymbol{\mu}_a + \frac{\sqrt{2}}{2} \boldsymbol{\mu}_b \right) \\
&= \frac{1}{2} D_a + \frac{1}{2} D_b + \boldsymbol{\mu}_a \cdot \boldsymbol{\mu}_b \\
&= \frac{1}{2} D_a + \frac{1}{2} D_b + \sqrt{D_a D_b} cos\theta
\end{aligned} \tag{2.36}$$

and

$$\begin{aligned} D_{excited1} &= \left(\frac{\sqrt{2}}{2}\boldsymbol{\mu}_a - \frac{\sqrt{2}}{2}\boldsymbol{\mu}_b\right) \times \left(\frac{\sqrt{2}}{2}\boldsymbol{\mu}_a - \frac{\sqrt{2}}{2}\boldsymbol{\mu}_b\right) \\ &= \frac{1}{2}D_a + \frac{1}{2}D_b - \boldsymbol{\mu}_a \cdot \boldsymbol{\mu}_b \\ &= \frac{1}{2}D_a + \frac{1}{2}D_b - \sqrt{D_a D_b}cos\theta, \end{aligned} \tag{2.37}$$

where $D_a$ and $D_b$ are the dipole strengths in the isolated molecule $a$ and $b$, respectively; $\theta$ is the angle between two vectors, $\boldsymbol{\mu}_a$ and $\boldsymbol{\mu}_b$. The dipole strength is responsible for the absorption intensity of each of the excitonic transitions, under the point-dipole approximation [62, 63] (the approximation is discussed in detail in section 2.4.1), the angle $\theta$ between two transition dipole moments decides its value. When the dipole strength is equal to zero, this specific excitonic transition is optically forbidden, which usually results in a very low intensity of absorption and emission spectra in experiments. This dipole strength will be redistributed on other excitonic bands, and it follows the rule that the summation of the dipole strengths of all excitonic bands in a molecular system is equal to the summation of the dipole strengths of separated molecules [61]. H- and J-aggregates of dimers are simple examples for explaining this concept, which is shown in Figure 2.4. In J-aggregate, $\theta = 0°$ and $H_{AB} < 0$, so the dipole strength at higher excitonic level $E_{excited1}$, is forbidden. However, in H-aggregate, although $\theta$ is also $0°$, $H_{AB} > 0$, so the dipole strength at lower excitonic level $E_{excited1}$, is forbidden. Therefore, the other excitonic band that is optically allowed for each aggregate possesses the dipole strength of $D_a + D_b$. This concept can be extended to a complex molecular system; for example, conjugated polymers or porphyrin rings, where the total transition dipole moment of a system is a linear combination of individuals on the chain or ring. The calculated dipole strength decides if it is transitionally forbidden, and it shows the absorption and emission ability in a specific excitonic band.

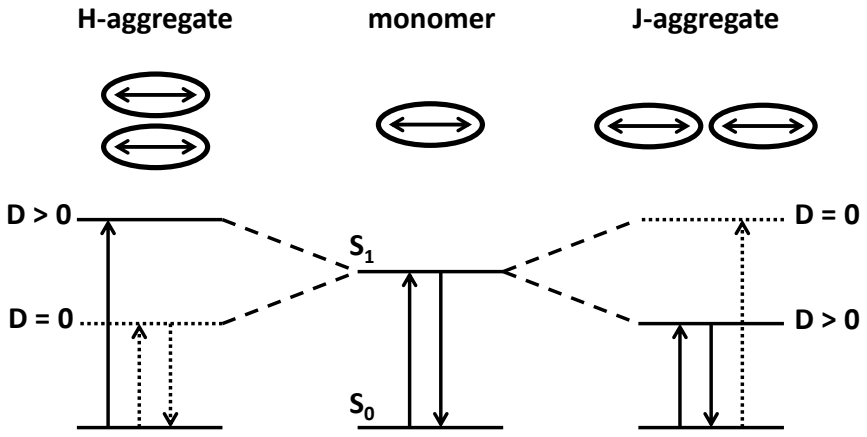


Figure 2.4: Schematic representation of the splitting of excitonic bands formed by a dimer with H- or J-aggregate. A monomer is able to absorb and emit photons between its $S_0$ and $S_1$ energy states, but when a dimer forms, the forbidden energy level may appear due to a zero of the structural vector sum of its transition dipole moments. The dotted lines and arrows represent the forbidden levels and transitions, respectively. In H-aggregate, the forbidden transition occurs at the lower energy state, whilst in J-aggregate, it is at the higher energy state.

## 2.3 De-excitation processes and dynamics

### 2.3.1 Non-radiative relaxations and photoluminescence

After light-perturbed electrons are promoted to excited states, several de-excitation processes usually follow in order to achieve thermal equilibrium. The Perrin-Jablonski diagram shown in Figure 2.5 can clearly describe the electronic transition pathways, in which the relaxation of excited energy can go through radiative ways (fluorescence and phosphorescence) or non-radiative processes (internal conversion and intersystem crossing) [38]. According to the Franck-Condon principle [50], the absorption of light occurs extremely quickly, with a time scale of $10^{-15}$ s during which no nuclear motion is involved. If the initial excitation energy is high enough for electrons to reach one of the vibronic levels of the second excited state ($S_2$), the electrons will experience a vibrational relaxation to the bottom of $S_2$ and then make the internal conversion to $S_1$ within period of time of $10^{-13} - 10^{-11}$ s. When electrons are at $S_1$, their lifetimes are around $10^{-10} - 10^{-7}$ s, and subsequently there are some competing processes, including the fluorescence from $S_1$ to $S_0$, internal conversion from $S_1$ to $S_0$ and

intersystem crossing from $S_1$ to another suitable vibronic triplet level in the first excited triplet state ($T_1$) [64]. It is noted that the internal conversion must happen in the same spin multiplicities. By Kasha's rule, the process of fluorescence, where excitation energy is relaxed by the emission of photons will occur at the bottom of $S_1$, because the internal conversion and nuclear vibrational relaxation are very rapid [65]. Hence, these relaxations lead to a shift between the absorption and the corresponding emission spectra, which is termed the Stokes shift. The Stokes shift occurs not only for the above reasons; for instance, the energy relaxation to the solvent molecules also results in the red shift of the emission spectrum [66, 67]. The spectra of the absorption and emission will follow mirror-image symmetry (Figure 2.3) at the wavenumber of 0–0 electronic transitions between $S_0$ and $S_1$ [68], if the Born-Oppenheimer approximation is valid [47], and the vibronic levels at $S_0$ and $S_1$ are of equal energetic difference. The process of fluorescence is also discussed in section 2.3.3. The transition of different multiplicities is basically not allowed, unless spin-orbit coupling exists in the system [46]. If so, the intersystem crossing process ($10^{-7} - 10^{-9}$ s) can be fast enough to compete with the fluorescencing and internal conversion. When the electrons are at the bottom of $T_1$ after another vibrational relaxation, they can release energy by emitting phosphorescence ($10^{-6} - 10$ s) or perform intersystem crossing back to $S_0$ once again. Due to the very-long lifetime of the excited electrons at $T_1$, generally, the probability that non-radiative mechanisms will occur is relatively high; for example, collision with solvent molecules in a sample solution is more efficient than luminescing phosphorescence.

### 2.3.2 Exciton dynamics and rate equations

The kinetics of radiative and non-radiative processes can be described by rate constants [69]:

$$k_{total} = k_{rad} + k_{non}, \tag{2.38}$$

where $k_{total}$ is the sum of all de-excitation rates; $k_{rad}$ is the rate of fluorescence emission from $S_1$ to $S_0$; $k_{non}$ is the rate for all non-radiative processes, which include internal conversion

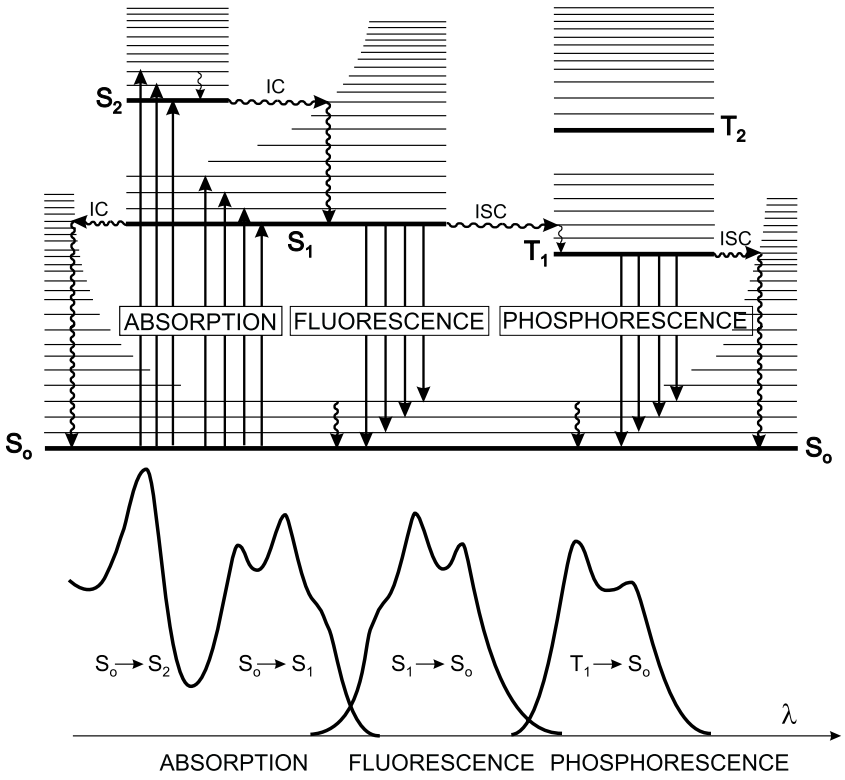


Figure 2.5: Perrin Jablonski diagram showing alternative pathways for the absorption of photons and de-excitation processes. The straight arrows pointing upwards represent vibronic transitions under absorption, and the population promoted to the excited state is formed. The straight arrows pointing downwards are the radiative pathways of the relaxation of energy, including fluorescence and phosphorescence, whilst the wavy arrows represent non-radiative relaxation processes containing internal conversion (IC) and inter system crossing (ISC). The spectra below depicts the corresponding wavelength distributions of absorption ($S_0 \rightarrow S_1$ and $S_0 \rightarrow S_2$), fluorescence ($S_1 \rightarrow S_0$) and phosphorescence ($T_1 \rightarrow S_0$). Taken from [38].

from $S_1$ to $S_0$ and the intersystem crossing from $S_1$ to $T_1$, non-radiative energy transfer from one molecule to another, and so on. A simple rate equation of the population of excited electrons is written as:

$$\frac{dn(t)}{dt} = G(t) - (k_{rad} + k_{non})n(t), \tag{2.39}$$

where $n(t)$ is the time-dependant number of the excited population at $S_1$, and $G(t)$ is the $\delta$ function-like generation of excited eletrons in the molecular system. The solution of $n(t)$ is given by:

$$n(t) = n(0) \exp\left(-(k_{rad} + k_{non})t\right), \tag{2.40}$$

where $n(0)$ is the initial number of excited electrons in the system. The lifetime of the excited population at $S_1$, $\tau$, is defined as:

$$\tau = \frac{1}{k_{rad} + k_{non}}, \tag{2.41}$$

In addition, the fluorescence quantum yield, $\phi$, is defined as [64]:

$$\phi = \frac{k_{rad}}{k_{total}} = k_{rad} \times \tau, \tag{2.42}$$

which is the fraction of the rate of relaxation of the excited population by emission of fluorescence to the rate of total de-excitation processes. It also represents the fraction of the number of emitted photons to the number of absorbed photons.

### 2.3.3 Einstein relation and emission rate

The theoretical model used to describe fluorescence, including stimulated and spontaneous emission, is derived from the Einstein relation, where the molecular system is assumed to be restricted to only the excitation of black body radiation [70, 71]. The rate of absorption is written as Equation 2.8:

$$\begin{aligned} \text{absorption rate} &= N_{total}\overline{(\mathbf{E}_0 \cdot \boldsymbol{\mu}_{21})^2}\rho_\nu(\nu_0)/\hbar^2 \\ &= N_{total}B\rho(\nu_0) \end{aligned} \tag{2.43}$$

where $\rho(\nu_0)$ is the energy density at $\nu_0 = \nu_2 - \nu_1$; $N_{total}$ is the atom density in the ground state; $B$ is one of the Einstein coefficients and is defined as $B = (2\pi f^2 D_{21})/(3n^2\hbar^2)$, where $f$ is the local-field correction factor and $n$ is the refractive index in a medium. According to the Einstein relation, the stimulated emission rate is written as $N_{S_1}B\rho(\nu_0)$, where $N_{S_1}$ is the atom density at $S_1$. Now assume the processes of emitting photons include stimulated and spontaneous emissions. The latter has the constant A, which is the other Einstein coefficient

for spontaneous emissions. Therefore, the total rate of emission is given by $N_{S_1}(B\rho(\nu_0)+A)$. Using Boltzmann distribution at thermal equilibrium, the fraction of atom densities at the first excited state, $S_1$, to those at the ground state is written as [72]:

$$\frac{N_{S_1}}{N_{total}} = \frac{B\rho(\nu_0)}{B\rho(\nu_0)+A} = \exp\left(\frac{-h\nu_0}{k_B T}\right), \tag{2.44}$$

where $k_B$ is the Boltzmann constant and $T$ is temperature. From Equation 2.44, the fraction of $A/B$ is given by:

$$\frac{A}{B} = \frac{\rho(\nu_0)\left[1-\exp\left(\frac{-h\nu_0}{k_B T}\right)\right]}{1-\exp\left(\frac{-h\nu_0}{k_B T}\right)}. \tag{2.45}$$

If $\rho(\nu_0)$ adopts the format of equation used in the Planck's black body radiation, it is written as [72]:

$$\rho(\nu_0) = \frac{8\pi h n^3 \nu^3}{c^3\left[\exp\left(\frac{-h\nu_0}{k_B T}\right)-1\right]}, \tag{2.46}$$

Therefore, putting Equation 2.46 back to Equation 2.45, the Einstein coefficient A can be rewritten as:

$$\begin{aligned} A &= \frac{8\pi h n^3 \nu^3}{c^3} B \\ &= \left(\frac{8\pi h n^3 \nu^3}{c^3}\right)\left(\frac{2\pi f^2 D_{21}}{3n^2\hbar^2}\right) \\ &= \frac{32\pi^3 f^2 n \nu^3}{3\hbar c^3} D_{21}, \end{aligned} \tag{2.47}$$

which means that both the Einstein coefficients A and B are proportional to the dipole strength, $D_{21}$, after being excited from the ground state to an electronic state with a higher energy. However, the expression in Equation 2.47 can only be used for the absorption of a single frequency, which is not the case for a conventional molecular system, whose absorption spectrum is usually broadened by phonon coupling and solvent effect. The modified fluorescening rate considering the integral of all dipole strengths, proposed by Strickler and Berg [68, 73, 74], may provide a closer value to the experimental result.

### 2.3.4 Fluorescence anisotropy of polarisation

Time-dependent fluorescence anisotropy of polarisation can provide information of depolarization dynamics in a molecular system on various time scales. For example, change in the molecular rotational orientation is observed via steady-state fluorescence anisotropy, whilst ultrafast intramolecular excitation energy relaxation can be noted via instantaneous fluorescence anisotropy, after the sample has been illuminated by a linearly polarised light source. Molecules have the tendency to selectively absorb light that is polarised parallel to its transition dipole moment. If the incident light is not parallel to the orientation of a transition dipole moment, the probability of the molecule being excited is proportional to the square of the scalar product of the vectors of the transition dipole moment and the incident electric field, i.e. $\cos^2\theta$, where $\theta$ is the angle between vectors of the transition dipole moment and the electric field of the incident light. When the light emitted by a sample is linearly polarised with a composition of vertical and parallel parts, the time-resolved fluorescence anisotropy $r$, as shown in Figure 2.6, is defined as [75, 76]:

$$r = \frac{I_{\parallel}(t) - I_{\perp}(t)}{I_{total}(t)} = \frac{I_{\parallel}(t) - I_{\perp}(t)}{I_{\parallel}(t) + 2I_{\perp}(t)} \tag{2.48}$$

where $I_{\perp}(t)$ and $I_{\parallel}(t)$ are the intensities of the light emitted with vertical and parallel polarisation, respectively, at time $t$; $I_{total}(t)$ is the sum of all emitted components polarised at $I_x(t)$, $I_y(t)$ and $I_z(t)$ with respect to the coordinates of incident light. There is an assumption that all polarised components in the three axes are independent from one another, so the depolarisation process is recorded by fluorescence anisotropy.

Assume that there are N motionless molecules with random orientations illuminated by polarised light along the z axis, and the absorption and emission transition dipole moments orientate in the same direction. The fluorescence intensity components are shown as [38]:

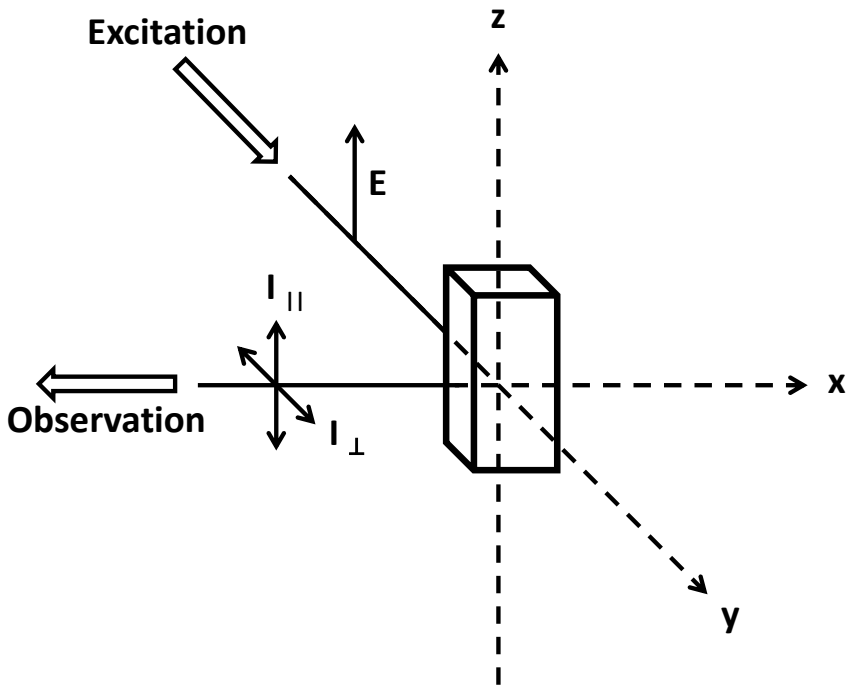


Figure 2.6: An illustration of the incident electric field on a sample and the corresponding intensity of the emission with different direction of polarisation. If the incident electric field is polarised at the $z$ axis, and the observation is located at the $x$ axis, the emission with polarisation along the $x$ axis cannot be observed. $I_{\parallel}$ and $I_{\perp}$ are the emissions with polarisation parallel and vertical to that of the incident excitation beam, respectively.

$$
\begin{aligned}
I_x(t) &= AD_E \sum_{i=1}^{N} \cos^2\theta_{xi}(t) = AND_E\overline{\cos^2\theta_x(t)} \\
I_y(t) &= AD_E \sum_{i=1}^{N} \cos^2\theta_{yi}(t) = AND_E\overline{\cos^2\theta_y(t)} \\
I_z(t) &= AD_E \sum_{i=1}^{N} \cos^2\theta_{zi}(t) = AND_E\overline{\cos^2\theta_z(t)}
\end{aligned}
\tag{2.49}
$$

where $A$ is a constant, $D_E$ is the emission dipole strength, and $\cos\theta_x$, $\cos\theta_y$, $\cos\theta_z$ are the cosines to the $x$, $y$, $z$ axes, respectively. Due to the symmetrical condition at the $z$ axis (incident light is polarised at the $z$ axis), $\overline{\cos^2\theta_x(t)} = \overline{\cos^2\theta_y(t)}$. In addition, $\overline{\cos^2\theta_x(t)} + \overline{\cos^2\theta_y(t)} + \overline{\cos^2\theta_z(t)} = 1$, and the fluorescence anisotropy is given by:

$$
\begin{aligned}
r\left(t\right) &= \frac{I_{\parallel}\left(t\right) - I_{\perp}\left(t\right)}{I_{total}\left(t\right)} = \frac{I_z\left(t\right) - I_y\left(t\right)}{I_x\left(t\right) + I_y\left(t\right) + I_z\left(t\right)} = \frac{\overline{cos^2\theta_z\left(t\right)} - \overline{cos^2\theta_x\left(t\right)}}{\overline{\cos^2\theta_x\left(t\right)} + \overline{\cos^2\theta_y\left(t\right)} + \overline{\cos^2\theta_z\left(t\right)}} \\
&= \overline{\cos^2\theta_z\left(t\right)} + \frac{\overline{\cos^2\theta_z\left(t\right)} - 1}{2} = \frac{3\overline{\cos^2\theta_z\left(t\right)} - 1}{2} \\
&= \frac{3\overline{\cos^2\theta_E\left(t\right)} - 1}{2},
\end{aligned} \tag{2.50}
$$

where $\cos\theta_z\left(t\right) = \cos\theta_E\left(t\right)$. The fraction of the excited molecules with transition dipole moment oriented parallelly to $\boldsymbol{\mu}_E$, with angles between $\theta$ and $\theta + d\theta$ and $\phi$ and $\phi + d\phi$, $W(\theta,\phi)d\theta d\phi$, is written as [38]:

$$
W(\theta,\phi)d\theta d\phi = \frac{\cos^2\theta\sin\theta d\theta d\phi}{\int_0^{2\pi} d\phi \int_0^{\pi} \cos^2\theta\sin\theta d\theta d\phi}. \tag{2.51}
$$

To obtain the emission probability with polarisation in the direction of the $z$ axis, the average of $\cos^2\theta$ is calculated as follows, using Equation 2.51:

$$
\begin{aligned}
\overline{\cos^2\theta} &= \int_0^{2\pi} d\phi \int_0^{\pi} \cos^2\theta W(\theta,\phi)d\theta \\
&= \frac{\int_0^{2\pi} d\phi \int_0^{\pi} \cos^4\theta\sin\theta d\theta}{\int_0^{2\pi} d\phi \int_0^{\pi} \cos^2\theta\sin\theta d\theta} = \frac{2\pi\times\frac{2}{5}}{\frac{4\pi}{3}} = \frac{3}{5}.
\end{aligned} \tag{2.52}
$$

Therefore, $r(0)$ in Equation 2.50 using the value in Equation 2.52 is calculated to be 0.4. The definition of angles with respect to the coordinates is shown in Figure 2.7. If N motionless molecules are distributed with random orientations illuminated by polarised light along the z axis, and the angle between the absorption and emission transition dipole

moments is $\alpha$, the average of $\cos^2\theta_E$ is written as:

$$\begin{aligned}\overline{\cos^2\theta_E} &= \cos^2\alpha\overline{\cos^2\theta_A} + \frac{1}{2}\sin^2\alpha\overline{\sin^2\theta_A} \\ &= \cos^2\alpha\overline{\cos^2\theta_A} + \frac{1}{2}\left(1-\cos^2\alpha\right)\left(1-\overline{\cos^2\theta_A}\right) \\ &= \frac{3}{2}\cos^2\alpha\overline{\cos^2\theta_A} + \frac{1}{2} - \frac{1}{2}\overline{\cos^2\theta_A} - \frac{1}{2}\cos^2\alpha \end{aligned} \tag{2.53}$$

And,

$$\begin{aligned} r(0) &= \frac{3\overline{\cos^2\theta_E}-1}{2} \\ &= \frac{1}{2\times 2}(9\cos^2\alpha\overline{\cos^2\theta_A} - 3\overline{\cos^2\theta_A} - 3\cos^2\alpha + 1) \\ &= \frac{3\overline{\cos^2\theta_A}-1}{2}\times\frac{3\cos^2\alpha-1}{2} \\ &= \frac{3\cos^2\alpha-1}{5}, \end{aligned} \tag{2.54}$$

where $\overline{\cos^2\theta_A} = \overline{\cos^2\theta}$ in Equation 2.52. Thus, when the transition dipole moments in a molecule are parallel to one another ($\alpha = 0°$), $r(0) = 0.4$; if the transition dipole moments in a molecule are perpendicular to one another ($\alpha = 90°$), $r(0) = -0.2$. They are the maximum and minimum values of $r(0)$, so $-0.2 < r(0) < 0.4$. There is a special case when the absorption and emission transition dipole moments orient randomly but are fixed on the same plane, $r(0)$ is written as:

$$r(0) \;\; = \frac{3\overline{\cos^2\alpha}-1}{5} = \frac{3\times\left(\frac{1}{2}\right)-1}{5} = 0.1. \tag{2.55}$$

## 2.4 Excitation energy transfer

The total Hamiltonian for a dimer has been shown in Equation 2.18, which contains the Hamiltonian for the separated molecules, $\hat{H}_a$ and $\hat{H}_b$, and the Hamiltonian for the Coulom-

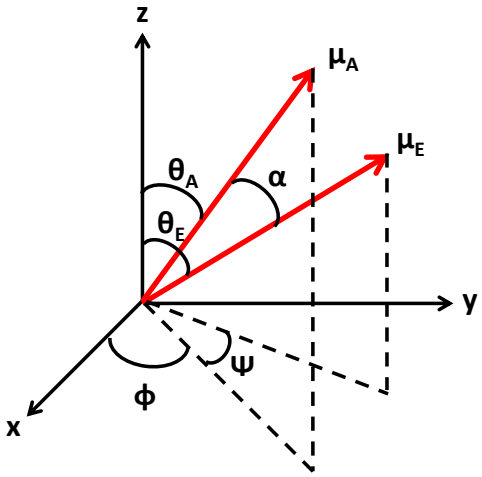


Figure 2.7: The definition of angles characterising the orientations of the absorption and emission transition dipole moments. It is noted that the absorption and emission transition dipole moments are not parallel to one another.

bic interaction between them, $\hat{H}_{inter}$. According to the electronic coupling strength of $\langle\psi_B|\hat{H}_{inter}|\psi_A\rangle$, which can be denoted as $H_{BA}$, different approximations can be adopted to treat the mechanisms of excitation energy transfer (EET). When two molecules are close enough, and $H_{BA}$ is much larger than the electron-phonon coupling (reorganisation energy), the original absorption and emission spectra of the individual molecules are influenced, and exciton bands are formed in a dimer [44]. Excitonic wavefunctions are delocalised over one molecule, and the coherent EET is dominated by the Redfield equation, where the Hamiltonian of electron-phonon coupling is considered as a perturbation to the system [76–78]. In some biological light harvesting systems, Redfield equation can describe the coherent EET accurately [76]. When $H_{BA}$ is much weaker than the reorganisation energy, $H_{BA}$ can be considered as the perturbation term. The system is treated by time-dependent perturbation theory, and the famous Förster resonance energy transfer (FRET) theory, presented by Theodor Förster [79], is used for the modelling of incoherent EET. When the distance between the pair of energy donor and acceptor is much larger than the molecular length of the chromophores, the point-dipole approximation can be used. In general, the exciton wavefunctions are quickly dephased due to the vibration relaxation before the transfer; hence, FRET dominates the EET in most of the molecular systems on a ps–ns timescale, and only the theory of FRET will be covered in this section.

### 2.4.1 Förster resonance energy transfer (FRET)

The Förster theory for EET is derived from the time-dependent perturbation theory and Fermi's golden rule [41, 79]. The derivation procedure is similar to that of the dipole strength discussed in section 2.2.1, but in EET, the energy donor and acceptor are involved and therefore the total energy includes the linear combination of either the donor or acceptor in the system which is promoted to the excited state. It is considered that there is usually more than one pair of the donor and acceptor in a molecular system, so the integral over the distribution of their energy difference is necessary. In addition, assume that the Born-Oppenheimer approximation holds [47], and therefore $H_{BA}$ can be written as:

$$\begin{aligned} H_{BA} &= H_{inter-el} \times H_{inter-nu} \\ &= \langle \psi_{a1}\psi_{b2}|\hat{H}_{inter}|\psi_{a2}\psi_{b1}\rangle\langle\chi_{a1}|\chi_{a2}\rangle\langle\chi_{b2}|\chi_{b1}\rangle, \end{aligned} \tag{2.56}$$

where $H_{inter-el}$ and $H_{inter-nu}$ are the Hamiltonians of pure electronic coupling and pure nuclear coupling, respectively; $\langle\chi_{a1}|\chi_{a2}\rangle$ is the Franck-Condon factor for vibronic transition from excited level 2 to ground level 1 in molecule $a$; $\langle\chi_{b2}|\chi_{b1}\rangle$ is the Franck-Condon factor for vibronic transition from ground level 1 to excited level 2 in molecule $b$ [50]. Using the assumptions described above and Equation 2.56, according to Fermi's golden rule, the total energy transfer rate $k_{EET}$ gives [39]:

$$\begin{aligned} k_{EET} = \frac{2\pi}{\hbar}|H_{inter-el}|^2 \left[\sum_j \sum_i W(j)|\langle\chi_{ai}|\chi_{aj}\rangle|^2\right] \left[\sum_k \sum_l W(k)|\langle\chi_{bl}|\chi_{bk}\rangle|^2\right] \\ \times \delta(\Delta E_{excited1} - \Delta E_{excited2}), \end{aligned} \tag{2.57}$$

where $\langle\chi_{ai}|\chi_{aj}\rangle$ is the Franck-Condon factor for vibronic transition from excited level $j$ to ground level $i$ in the molecule $a$; $\langle\chi_{bl}|\chi_{bk}\rangle$ is the Frank-Condon factor for vibronic transition from ground level $k$ to excited level $l$ in the molecule $b$; $W(j)$ and $W(k)$ are the weighted functions by Boltzmann distribution at the excited-state vibronic level $j$ and ground-state vibronic level $k$, respectively. $\delta(\Delta E_{excited1} - \Delta E_{excited2})$ is the resonance condition obeying

the law of conservation of energy. $H_{inter-el}$ is dominated by the Coulombic interaction between the pair of donor and acceptor. If there is no orbital overlap, the distance between them is several times larger than the chromophore's scale, and there is no net charge in the system, $\hat{H}_{inter-el}$ can be approximated by an operator of long-range dipole-dipole interaction, $\hat{H}_{inter-DD}$, which is obtained by assuming that the interaction between monopoles and between higher order terms in Taylor's expansion of the electric potential energy are relatively small [80]. $\hat{H}_{inter-DD}$ is given as:

$$\hat{H}_{inter-DD} = \frac{f^2}{n^2}\left[\frac{\hat{\mu_a}\cdot\hat{\mu_b}}{|\mathbf{R}_{ab}|^3} - \frac{3(\hat{\mu_a}\cdot\mathbf{R}_{ab})(\hat{\mu_b}\cdot\mathbf{R}_{ab})}{|\mathbf{R}_{ab}|^5}\right], \tag{2.58}$$

where $\mathbf{R}_{ab}$ is the vector from molecule $a$ to molecule $b$; $f$ and $n$ are the corrections for the local field and the bath refractive index, respectively. Therefore, $H_{inter-el}$ is approximated by $H_{inter-DD}$ and is written as:

$$\begin{aligned} H_{inter-DD} &= \frac{f^2}{n^2}\left[\frac{\langle\phi_{a2}|\boldsymbol{\mu}_a|\phi_{a1}\rangle\cdot\langle\phi_{b2}|\boldsymbol{\mu}_b|\phi_{b1}\rangle}{|\mathbf{R}_{ab}|^3} - \frac{3(\langle\phi_{a2}|\boldsymbol{\mu}_a|\phi_{a1}\rangle\cdot\mathbf{R}_{ab})(\langle\phi_{b2}|\boldsymbol{\mu}_b|\phi_{b1}\rangle\cdot\mathbf{R}_{ab})}{|\mathbf{R}_{ab}|^5}\right] \\ &= \frac{f^2}{n^2}\left[\frac{\sqrt{D_a}\sqrt{D_b}(\cos\theta - 3\cos\alpha\cos\beta)}{|\mathbf{R}_{ab}|^3}\right] \\ &= \frac{f^2}{n^2}\left[\frac{\sqrt{D_a}\sqrt{D_b}\kappa}{|\mathbf{R}_{ab}|^3}\right], \end{aligned} \tag{2.59}$$

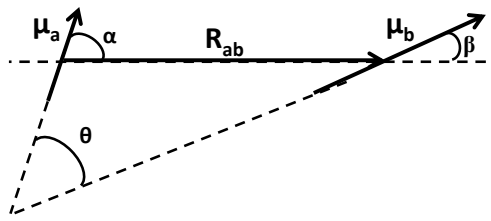


Figure 2.8: Illustration of the defined angles between the transition dipole moments of a donor and an acceptor, where the efficiency of non-radiative energy transfer depends on their Coulombic interaction. $R_{ab}$ is the vector between these two transition dipole moments.

where $D_a$ and $D_b$ are the dipole strength of molecules $a$ and $b$ when being separated, and defined angles between the transition dipole moments are shown in Figure 2.8. $\kappa = \cos\theta - 3\cos\alpha\cos\beta$ is the point-dipole approximation. $\kappa^2$ is 2/3 when random rotational dynamics

are faster than the de-excitation rate, whilst $\kappa^2$ is 0.476 for motionless random orientations and random distances of the donor-acceptor pairs [81]. Next, $H_{inter-DD}$ is substituted for $H_{inter-el}$ in Equation 2.57 and according to Föster's theory, $k_{EET}$ is rewritten as [79]:

$$\begin{aligned} k_{EET} &= \left(\frac{9000\ln(10)}{128\pi^5 N_A}\frac{\kappa^2\phi_D}{n^4}\right)\left(\frac{1}{\tau|\mathbf{R}_{ab}|^6}\right)\left(\frac{\int_0^\infty F_D(\nu)\epsilon_A(\nu)\nu^{-4}d\nu}{\int_0^\infty F_D(\nu)d\nu}\right) \\ &= \frac{1}{\tau}\left|\frac{R_0}{\mathbf{R}_{ab}}\right|^6, \end{aligned} \tag{2.60}$$

where $\phi_D$ is the donor fluorescence quantum yield in the absence of the acceptor; $F_D(\nu)$ is the fluorescence spectrum of the donor; $\epsilon_A(\nu)$ is the molar extinction coefficient of the acceptor. $R_0$ is the Förster radius, which is read:

$$R_0 = \left[\frac{9000\ln(10)}{128\pi^5 N_A}\frac{\kappa^2\phi_D}{n^4}\frac{\int_0^\infty F_D(\nu)\epsilon_A(\nu)\nu^{-4}d\nu}{\int_0^\infty F_D(\nu)d\nu}\right]^{\frac{1}{6}}. \tag{2.61}$$

The physical parameter, $R_0$, in FRET is the critical distance where the radiative decay rate of the donor in the absence of acceptors is the same as the rate of EET. It is very sensitive in the distance range of 2-10 nm and has been used as a spectroscopic ruler to resolve the distance between the donor-acceptor pairs in a condensed-phase system, especially in biological applications. In addition, the EET efficiency, $\Phi_{EET}$, can be defined as [61]:

$$\Phi_{EET} = \frac{k_{EET}}{\frac{1}{\tau}+k_{EET}} = \frac{\frac{1}{\tau}\left|\frac{R_0}{\mathbf{R}_{ab}}\right|^6}{\frac{1}{\tau}+\frac{1}{\tau}\left|\frac{R_0}{\mathbf{R}_{ab}}\right|^6} = \frac{1}{1+\left(\frac{r}{R_0}\right)^6}. \tag{2.62}$$

Thus, when the distance between molecules is equal to $R_0$, $\Phi_{EET}$ is 50%.

If the distance between the donor-acceptor pairs is less than 1 nm, the EET can be realised via electron exchange, where the orbital overlap between molecules occurs in close physical proximity. This mechanism was first proposed by D. L. Dexter [82]. $H_{inter-el}$ must now contain elements of $H_{inter-el}^{Coulomb}$ and $H_{inter-el}^{exchange}$, where $H_{inter-el}^{Coulomb}$ is the original $H_{inter-el}$ in Equation 2.56, and $H_{inter-el}^{exchange}$ is the Hamiltonian of the Coulomb interaction in the condition

of electron exchange. Using Fermi's golden rule, the energy transfer rate of the Dexter mechanism is approximated to be proportional to $\exp(-\mathbf{R}_{ab}/L)$, where $L$ is the average Bohr radius [39]. This function depends even more strongly on the distance between the donor and acceptor than FRET, so when $R_{ab} > 1$ nm, EET is dominated by FRET.

The PL waveform influenced by EET in an organic complex is usually analysed and fitted by multi-exponential functions; however, it is sometimes difficult to rationalise the fitted parameters, for example, the fitted PL decay rates. The fitting functions are best constrained by the characteristics of the studied system with meaningful physical models, so that the resultant parameters in various processes of the exciton dynamics can be assigned by physical significance. If there are no suitable physical models to perform a simulation, the empirical exponential stretched function can be employed, which has a small number of undecided parameters and has been proven to be able to analyse the PL quenching mechanisms in the absence of energy diffusion before FRET occurs [83]. It is given as:

$$I(t) = A \exp\left[-\left(\frac{t}{\tau_d}\right)^{\beta}\right], \tag{2.63}$$

where $A$ is the pre-exponential factor, and $\tau_d$ is the lifetime of an energy donor in the presence of acceptors. Here $\beta$ is the stretched parameter, and in the FRET, $\beta$ is equal to 1/6, 1/3 and 1/2 for a one-, two- and three-dimensional molecular system, respectively. Nevertheless, in the experiment, energy diffusion is usually observed to occur in a molecular system between energy donors, as long as they have spectral overlaps, before the energy is transferred to the acceptor; energy diffusivity is therefore time-dependent. Different configurations of the molecular aggregates can result in various excitonic states. After being promoted to the excited state by the pulsed laser, the excitons start their intrachain and/or interchain diffusion. They first have a distribution with a higher than average energy, and then the population gradually diffuses to those who have lower energy, because the spectral overlap of excited species is larger at long-wavelength electronic transitions than the short-wavelength versions [38]. Thus, the average energy of the chromophores decreases with time and finally achieves the lowest value, since all of the excitons have already relocated to the lowest energy

states. In the whole process of FRET, energy diffusivity keeps descending because the spatial distribution of the energy ensemble becomes broadened and consequently excitons became stationary. As a result, PL decay rates are also time-dependent. This physical phenomenon could be described by the complicated Monte-Carlo simulation, but it usually introduces heavy computational costs and has no explicit expressions.

# Chapter 3

# Experimental Methods

The classification of experimental techniques for investigating photophysics, which record the photoluminescence (PL) emitted by specific samples, can be divided into time-integrated (steady-state) and time-resolved regimes. Time-integrated PL is obtained by long-term collection (in the order of seconds), and excitons that relax by emitting photons at various timescales are weighted to make contributions to the final spectrum. Information from ultrafast exciton dynamics [84], may only contribute a relatively small amount of data and therefore cannot be recognised clearly in time-integrated PL. Fortunately, time-resolved techniques, including photoluminescence up-conversion spectroscopy (PLUCS) and time-correlated single photon counting (TCSPC), are able to provide abundant time-resolved spectroscopic information with a time-resolution of hundreds of femtoseconds and hundreds of picoseconds, respectively. PLUCS is used to measure electronic dynamics occurring in the range from sub-picoseconds to around one nanosecond. The mapping of an ultrafast optical waveform needs synchronic interaction between the time-delayed ultrashort duration (100 fs) of laser pulses and the sample PL in a non-linear crystal to generate a third frequency-mixing signal. This method is termed optical-gating and possesses the highest time-resolution at present, but it has a complicated experimental setup. TCSPC, which is electronically-gated, is employed to study mechanisms in the time region from sub- to several nanoseconds. The system is sensitive, relatively easy to build up and has been widely commercialised. In this

chapter, the theory of the generation of the femtosecond laser pulse and non-linear optics are introduced. Next, the details of the experimental setups of PLUCS and TCSPC are explained.

## 3.1 Generation of femtosecond pulses

The ultrashort duration (100 fs) of a femtosecond laser pulse is beneficial for visualisation of the electronic dynamics occurring in the femtosecond regime because of its superior temporal resolution (∼500 fs in our PLUCS for sample solutions). The sample can also be therefore promoted to the excited-state in a period of time much shorter than its PL lifetime. In addition, high pulse power also provides more opportunities for various levels of applications. Femtosecond pulses are generated by the longitudinal mode-locking (phase-locking) method, where the initial phases of all the non-continuous modes in a laser resonant cavity are fixed to obtain stable output pulses to propagate through the cavity. The interference between these modes results in several time intervals, in which unsaturated gain is larger than the cavity loss; hence, the mode-locking pulse peaks are amplified. The normalised spectrum for $N$ periods in a laser cavity is described as [85]:

$$\begin{aligned}\mathbf{E}^N(\omega) &= \frac{1}{NT}\int_0^{NT}\mathbf{E}(t)\exp(i\omega t)dt \\ &= \frac{1}{N}\frac{1-\exp(i\omega NT)}{1-\exp(i\omega T)}\mathbf{E}(\omega),\end{aligned} \tag{3.1}$$

where $\omega$ is the frequency, and $T$ is the round-trip time of flight. It is noted that the electric field in the cavity is periodic, so $\mathbf{E}(t) = \mathbf{E}(t+nT)$. Therefore, the intensity of the spectrum in the cavity is simply written and approximated as [85]:

$$\begin{aligned}I^N(\omega) &= |\mathbf{E}^N(\omega)|^2 = \frac{1}{N^2}\left|\frac{1-\exp(i\omega NT)}{1-\exp(i\omega T)}\right|^2|\mathbf{E}(\omega)|^2 \\ &= \frac{1}{N^2}\frac{\sin^2(N\omega T/2)}{\sin^2(\omega T)}I(\omega).\end{aligned} \tag{3.2}$$

According to the Fourier transform, the periodic peak combination in the frequency domain leads to a periodic repetition of pulses formed by wavepackets in the time domain. A larger number of modes causes the intensity of the pulse peak to be higher and the pulse duration shorter. In this thesis, Sapphire doped with Titanium (Ti:Sapphire) is chosen to be used as a laser gain medium due to its broad spectral bandwidth. For a standard wavelength of 800 nm, the laser could have more than one million modes in the cavity, and the pulse duration is around 100 fs. In the Ti:Sapphire mode-locking laser, the passive Kerr-lens mode-locking method is used to accomplish the cavity modulation described above. Ti:Sapphire acts as a Kerr medium that follows the Kerr's effect: $n = n_0 + n_2 I$, where $n_0$ and $n_2$ are linear and non-linear coefficients of the refractive indices, respectively [86]. The distribution of refractive indices are intensity-dependent in Ti:Sapphire, so the high intensity part of the Gaussian laser beam is self-focused, and the remainder of the beam with lower intensity has a lower transmission, when there is a suitable aperture in the beam pathway. In order to achieve the phase fixing of different wavelengths of light in a time domain, compensation for group velocity dispersion (GVD) must be made because components with shorter wavelengths propagate slower in a medium, which leads to pulse stretching. The compensation is usually achieved by prism compensators to maintain the difference in the length of various optical paths, i.e. the faster components travel longer optical paths than the slower.

## 3.2 Non-linear optics in PLUCS

When the intensity of the input light illuminated on a material is low, its polarisation density, $\mathbf{P}$, is linearly proportional to the incident electric field, $\mathbf{E}$, with a relationship as $\mathbf{P} = \epsilon_0 \chi_1 \mathbf{E}$, where $\epsilon_0$ and $\chi_1$ are the vacuum permittivity and first-order susceptibility, respectively; $\mathbf{E}$ is the magnitude of the electric field. However, when the incident light becomes intense, higher

order terms of $\mathbf{P}$ must be added to the relationship described above as [87]:

$$\begin{aligned}\mathbf{P} &= \mathbf{P}_1 + \mathbf{P}_2 + \cdots + \mathbf{P}_N \\ &= \epsilon_0 \left(\chi_1 \mathbf{E} + \chi_2 \mathbf{E}^2 + \cdots + \chi_N \mathbf{E}^N\right), \end{aligned} \tag{3.3}$$

where $\mathbf{P}_N$ and $\chi_N$ are the $N$th-order non-linear polarisation and susceptibility in a material, respectively. It is noted that even for a material whose $\chi_2$ and $\chi_3$ are relatively large (higher terms of $\chi_N$ are even smaller than $\chi_2$ and $\chi_3$), polarisation is still dominated by the linear first-order term when $\mathbf{E}$ is not strong enough. In addition, the non-linear medium must be non-centrosymmetric to have a non-zero $\chi_2$ [88]. Fortunately, a femtosecond pulse with great intensity of $\mathbf{E}$ is efficient for applications of non-linear optics, where the frequency of the output pulse is converted from that of the incident beams. For example, second harmonic generation (SHG) and frequency mixing are the fundamentals of PLUCS, and they are based on the non-linear term of $\mathbf{P}_2 = \epsilon_0 \chi_2 \mathbf{E}^2$. It is assumed that there are two intense monochromatic plane waves of the form of $\mathbf{E}_i = \mathbf{E}_0^i \cos(\omega_i t)$, $i = 1$ or 2, incident on a non-linear medium, and $P_2(t)$ is written as:

$$\begin{aligned}\mathbf{P}_2(t) &= \epsilon_0 \chi_2 (\mathbf{E}_1 \times \mathbf{E}_2) \\ &= \epsilon_0 \chi_2 \mathbf{E}_0^1 \mathbf{E}_0^2 [\cos(\omega_1 + \omega_2)t + \cos(\omega_1 - \omega_2)t]/2, \end{aligned} \tag{3.4}$$

where $\chi_2$ is usually a tensor, but is assumed to be a scalar here. Equation 3.4 shows that two polarisations with frequency mixing ($\omega_1 + \omega_2$ and $\omega_1 - \omega_2$) are generated by the non-linear effect. The mixing of the frequencies of $\omega_{mix} = \omega_1 + \omega_2$, is efficient when the resultant new electric field is coherent with the incident waves with frequencies of $\omega_1$ and $\omega_2$, and they must fulfil the requirements of energy conservation ($\hbar\omega_{mix} = \hbar\omega_1 + \hbar\omega_2$) and momentum conservation ($\mathbf{k_{mix}} = \mathbf{k_1} + \mathbf{k_2}$) of photons [89]. Momentum conservation of photons is not easy to achieve, because it is concerned with the refractive index of the medium and can be rewritten as $n_{mix}\omega_{mix} = n_1\omega_1 + n_2\omega_2$. Therefore, a medium used to up-convert two waves with the same or different frequencies should follow the two conditions described

above, which are also termed frequency matching and phase-matching, separately. In the experiment, phase-matching is conducted using a non-linear crystal as the medium, which has suitable birefringent properties, and the tilted angle with respect to the incident waves is carefully chosen to obtain correct refractive indices of $n_1$, $n_2$ and $n_{mix}$.

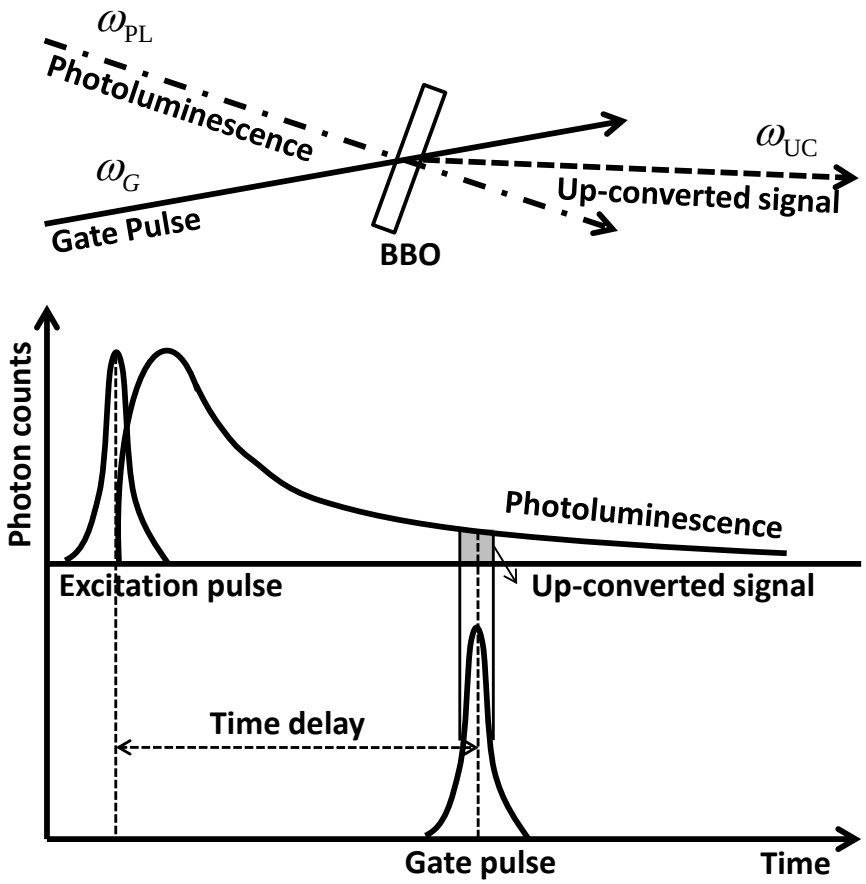


Figure 3.1: Schematic diagram to explain the process of non-linear up-conversion in PLUCS. At the top of the figure, after photoexcitation, frequency mixing of the incident PL from a sample and gate beams from the fundamental laser is realised via an appropriate angle of the BBO crystal fulfilling the phase-matching condition ($\omega_{UC} = \omega_{PL} + \omega_G$). The lower graph illustrates the method used to map out the emitted PL by optical gating, where a carefully controlled time-delayed gate pulse is used to scan a specific time interval, and only the photons at the spatially and temporally overlapped region are up-converted.

Second harmonic generation (SHG) is an example of frequency mixing. Two plane waves have the same frequency ($\omega_1 = \omega_2$) and the generated wave is double the frequency of the incident wave ($\omega_{mix} = 2\omega_1 = 2\omega_2$). The incident waves must propagate colinearly through the non-linear uniaxial crystal with polarisation perpendicular to its optical axis to fulfil the phase-matching condition, which may be achieved by adjusting the angle, $\theta$, between the

propagating direction of the incident waves, so that $n_o = n_{mix}(\theta)$, where $n_o \leq n_{mix}(\theta) \leq n_e$; $n_o$ and $n_e$ are the ordinary and extraordinary refractive indices of the medium, respectively [87]. SHG is usually necessary for the excitation of organic materials by Ti:Sapphire laser, because it halves the output fundamental wavelengths of the laser pulse originally falling in the region between 690 and 1040 nm.

Photoluminescence up-conversion spectroscopy (PLUCS), one of the pump-probe techniques, is based on the same frequency-mixing principle. Here, $\omega_1 = \omega_{PL}$ and $\omega_2 = \omega_G$; $\omega_{mix} = \omega_{UC} = \omega_{PL} + \omega_G$, where $\omega_{PL}$ is the frequency of PL emitted from a sample, which is an excited-state organic complex in this thesis, and $\omega_G$ is the frequency of one of the splitted beams from the femtosecond laser (gate beam), as shown in Figure. 3.1. The up-converted photons with a frequency of $\omega_{UC}$ are generated with an appropriate non-linear crystal with a correct angle that allows phase-matching between two incident beams and the up-converted one. In addition, the incident PL from the sample and the time-delayed laser gate pulse must overlap temporally. According to Equation 3.4, the intensity of the output up-converted signal is proportional to the product of $\mathbf{E}_1$ and $\mathbf{E}_2$, i.e. $\mathbf{E}_{PL} \times \mathbf{E}_G$. In the experiment, the intensity of the gate pulse is fixed, so the up-converted signal is proportional to the PL waveform. Thus, the optical gating method is realised using the gate pulse as an optical shutter, and various time-delayed gate pulses performed by an optical delay line enable the scanning of the PL waveform. In this thesis the non-linear crystal is chosen to be beta barium borate ($\beta$-$BaB_2O_2$, BBO) due to its reasonably high $\chi_2 = 1.28$ pmV$^{-1}$ and small absorption in the visible to infrared regions [90].

## 3.3 Experimental setup of PLUCS

The experimental setup of PLUCS is shown in Figure 3.2. Vertical-polarised ultrashort pulses (<100 fs duration, 80 MHz repetition rate, tunable centre wavelength in the region of 690–1040 nm and >2.5 W average pulse power) are output from a mode-locking Ti:Sapphire laser (Spectra-Physics, Mai Tai), which is pumped by a CW Nd-YAG laser (Spectra-Physics,

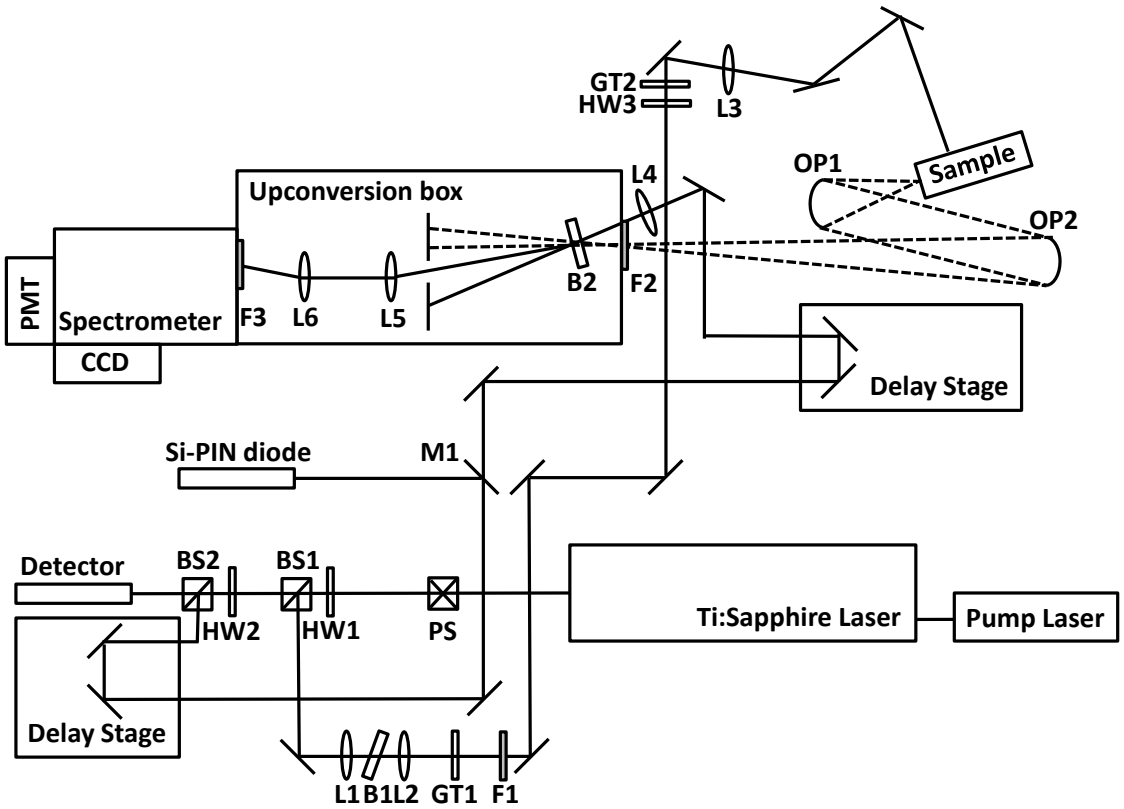


Figure 3.2: The experimental setup of PLUCS, which can perform a sub-picosecond time-resolved PL decay. It is noted that during the measurement, the mirror M1 has to be removed. This setup can also be used for the measurement of time-integrated PL (by replacing B2 with a Glan-Thompson polariser) and TCSPC (by putting M1 back into the system).

Millennia) at 532 nm, 5.5 W. The pulse first passes through a periscope (PS) to adjust the beam height to 6", and pass through the polarising beam splitter (BS1) which separate the split beams into two routes, where the relative intensity of each beam is controlled by the half-wave plate (HW1). Of these two routes, one is the gate beam for the purpose of probing, whilst the other is the excitation beam for pumping the sample to generate PL. The separated intense gate beam meets another set of half-wave plate (HW2) and polarising beam splitter (BS2) to reset its polarisation back to vertically-orientated. The minority of the beam goes to a detector, and the majority passes through a fixed delay stage and another computer-controlled mechanical delay stage to arrive on the BBO crystal (B2) for the preparation for the up-conversion process in the box. It is noted that the mirror M1 is taken away, so that the Si-PIN diode is not working here.

On the other hand, if an organic sample needs to be excited between 345 - 520 nm, the excitation beam is first focused by a lens (L1) on the BBO crystal (B1) to be frequency doubled. The residual fundamental beam is collimated by a lens (L2) and blocked by a combination of a vertically-polarised Glan-Thompson polarisor (GT1) (the frequency doubled component is horizontally-polarised) and a band-pass colour filter (F1). Subsequently, it is directed to another set of half-wave plate (HW3) and Glan-Thompson polariser (GT2) for the final adjustment of polarisation state and pulse power for the sample excitation, which is focused again by a lens (L3). The liquid sample is kept in a quartz cuvette fixed by a home-made cuvette holder, and the emitted PL from the sample is collected by a pair of off-axis parabolic mirrors (OP1 and OP2) and focused onto the BBO crystal (B2) in the up-conversion box.

The mixing angle between the PL from the sample and the gate beam is set to be 12° at the B2 for the up-conversion process, which is mounted on a computer-controlled rotation stage, allowing the phase-matching condition to be fulfilled corresponding to different incident PL wavelengths. The up-converted photons are focused and directed by a pair of lenses (L5 and L6) to a spectrometer (Jobin Yvon Triax 90) and then dispersed and detected by a liquid-nitrogen-cooled charge-coupled device (CCD) (Jobin Yvon:Symphony). Therefore, a time-resolved PL decay is mapped out by the computer-controlled time-delayed gate beam over a specific time interval of the optical waveform emitted by the sample. It is noted that the up-conversion signal is usually weak, so in addition to a long integration time by the CCD, a high signal-to-noise ratio must be achieved by reducing background noise, which is mainly from the reflected excitation beam from the cuvette surface and the frequency-doubled signal of the gate beam through B2. They can be reduced by a suitable set of long-pass or band pass colour filters (F2 and F3) with the combination of an aperture with an appropriate size. The temporal resolution of the sample in solution is roughly 500 fs, which is decided by the cross-correlation of the gate beam and the excitation beam scattered from the surface of the cuvette.

The time-integrated PL spectrum emitted from the sample can also be collected by the

| Equipment | Details |
|---|---|
| Pump laser | Nd-Yag laser |
| Ti:sapphire laser | Spectra-Physics, Mai Tai |
| PS | Periscope |
| HW1, HW2, HW3 | Half-wave plate |
| BS1, BS2 | Beam-splitters |
| L1, L2, L3, L4, L5, L6 | Focusing lens |
| B1, B2 | BBO crystals |
| GT1, GT2 | Glan-Thompson Polariser |
| OP1, OP2 | Off-axis parabolic mirrors |
| F1, F2, F3 | Colour filters |
| CCD | Charged-coupled device |
| PMT | Photomultiplier tube |

Table 3.1: List of equipments used in PLUCS

same experimental setup, but the gate beam must be blocked, and B2 is replaced by a Glan-Thompson polariser, which allows the measurement of the emitted PL polarisation states. Furthermore, F2 and F3 may also need to be carefully chosen to permit the correct optical waveform to be detected by the CCD.

## 3.4 Operating principle of TCSPC

In addition to PLUCS, time-correlated single photon counting (TCSPC) is another technique for observing the electronic dynamics in a sample [91]. The time resolution falls between sub-nanoseconds to hundreds of nanoseconds, which is lower than PLUCS due to its electronic gating method; however, it possesses high sensitivity to the low PL intensity and is a relatively easy-to-build system. The time resolution is limited by the response speed in the electronics and is characterised by the instrument response function (IRF), which is mainly composed of contributions from the laser system and the optical layout. The time resolution is defined as the full width of half maximum (FWHM) of the IRF, which is better than any analogue recording technique at present, and it is around 120 ps in this system. With a light source with a high repetition rate, where the time interval of each laser pulse is fixed, TCSPC makes high-speed measurement possible. Several million photons can be detected

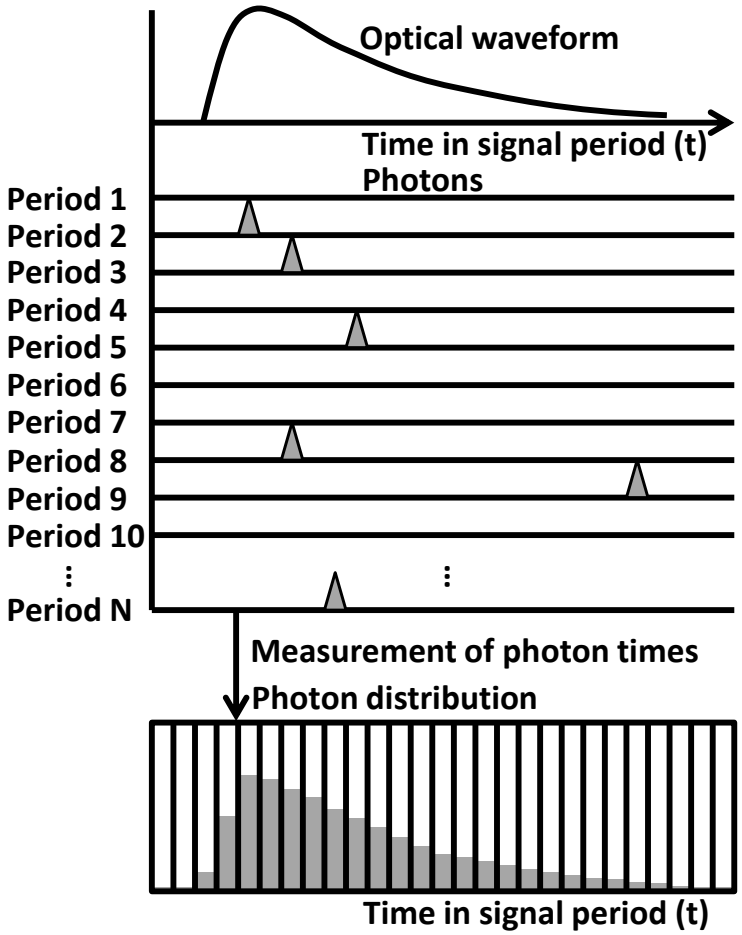


Figure 3.3: A schematic diagram shows the process of obtaining a histogram in TCSPC. Less than one photon is detected in each measurement period, and the information is transformed by electronics to finally form a histogram simulating the real optical waveform.

every second.

The general principle is shown in Figure 3.3. One of the separated fundamental laser beams hits a silicon-PIN diode, where a series of pulses (80 MHz repetition rate) are considered to be "start" signals in the recording process by the electronics. Meanwhile, the other separated fundamental laser beam is used to synchronously excite the sample, whose PL shone on a photomultiplier tube (PMT) is considered to be a "stop" signal for the recording process. There are many recording periods, defined by the period of time between the "start" and "stop" pulses, and in each period, the probability of detecting one photon is much less than one. It is noted that if the average number of photons emitted by the sample exceeds 0.01 to 0.1 per signal period, the resultant waveform may be distorted because of the pile-up

effect, whereby some photons may not be counted and therefore lead to a shortened PL lifetime. Hence, in some of the periods, there are no photons to be detected and the probability of finding more than one photon is very small. When a photon is detected, its travelling time is recorded, and the corresponding computer memory, whose location in the electronics is related to the photon propagation time, is increased by one. After many repetitions of detections, a histogram, which is a convolution of the IRF and the real sample PL waveform, is built. If the lifetime of the sample PL is of the same order of magnitude compared with the IRF, the deconvolution technique must be used to restore the real sample PL.

## 3.5 Electronics in TCSPC

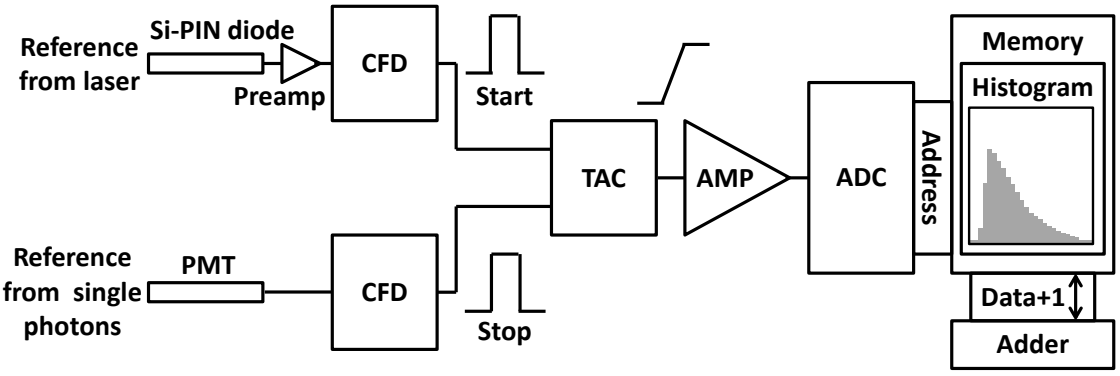


Figure 3.4: The simplified electronics used in TCSPC. It is noted that CFD denotes constant fraction discriminator, TAC time-to-amplitude converter, AMP amplifier and ADC analogue-to-digital converter. The references of the signal sources are usually exchanged for the purpose of circuit design, but the system works with the same operating principle.

The layout of the TCSPC electronics is shown in Figure 3.4 [91]. As described in the previous section, the fundamental laser beam is split into two, and one is used for the sample excitation, whilst the other sends the "start" pulse to the silicon-PIN diode. Here, a constant fraction discriminator (CFD) is used to reduce background noise and the time fluctuation resulting from the pulse amplitude jitter in PMT, which has random amplification as one of its characteristics. The other CFD connected to the silicon-PIN diode is also for the purpose of preventing the amplitude jitter of the reference "start" pulse. Next, the output square waves of these two CFDs are used as "start" and "stop" signals to the time-to-amplitude

converter (TAC), where the photon propagation time is converted to a corresponding voltage across a capacitor. The TAC output voltage is then fed to a biased-amplifier (AMP), and then sent to the analogue-to-digital converter (ADC) to form a digital counterpart of the amplified TAC signal with time channels as small as 1 ps. The ADC output functions to plus 1 in a specific address of the memory array, which is concerned with the period of time between the "start" and "stop" pulses. Finally, after many repetitions of detections, a time-resolved histogram representing the PL transient is created.

In the experiment, the electronic layout is usually modified to exchange the light sources of the "start" and "stop" pulses, i.e. the laser pulses on the silicon-PIN diode are used as a "stop" signal, whilst detection of a photon by the PMT is used as the "stop" indicator. This change is adopted to reduce the overloading issue of the TAC. In the original design, the periods when no photons are detected render the recording process unstopped, so a compensating circuit in the traditional TCSPC electronics is needed to reset the TAC. However, the Ti:Sappire laser with a repetition rate of 80 MHZ renders a reset of TAC as short as 15 ns unfeasible. Thus, the reverse of the "start" and "stop" configuration permits the TAC to only work during the periods when a photon is detected. Compensation of the inversed trend of the TAC output voltage can be realised by a simple circuit design.

# Chapter 4

# Full Delocalisation of the Absorbing Excited State in Porphyrin Nanorings

## 4.1 Introduction and Background

In this chapter, experimental results obtained from the steady-state photoluminescence and time-resolved spectroscopy on synthesised porphyrin nanorings are demonstrated and discussed. Porphyrin ring assemblies are building blocks for establishing the photosynthetic system in nature, where they are used as the light antenna to harvest solar energy with almost 100% quantum efficiency, and the excitation energy subsequently arrives at chemical reaction centers [92–95]. Some of these protein-pigment assemblies have strong intermolecular coupling and the exciton wavefunctions are often remarkably delocalised between adjacent feeder antennae, for example, within the B850 ring of light harvesting system 2 (LH-2) from bacterium Rhodobacter shpaeroides [96–100]. The delocalised excitation states following the initial light absorption may facilitate the formation of charge-separated states in typical synthetic materials used in organic photovoltaics, which plays a crucial role in device efficiency [25, 26]. A widely-delocalised electronic wavefunction may be achieved and attributed to the structural rigidity of materials; for instance, fullerenes and porphyrins possess stiff structures [101–103], and their superior properties of photophysics have inspired researchers

to synthesise biomimetic materials with high electronic delocalisation. However, the fully conjugated macrocyles synthesised in the laboratory are intrinsically different from their counterparts in nature, where individual chromophores are surrounded and supported by proteins [92–94]. Furthermore, not all of the man-made fully conjugated macrocycles possess widely-delocalised electronic wavefunctions; instead, the excitation energy is transfered via a slower non-radiative resonance process [12–14].

Here, a fully $\pi$-conjugated porphyrin nanoring system is demonstrated, which exhibits a property of full delocalisation of electronic wavefunctions along the ring following light absorption. Remarkably, such initial electronic delocalisation is able to be maintained in larger rings, even in the largest version that includes 24 porphyrin units with a diameter of $\sim$10 nm. Due to the symmetry of circular structures, transitions of the nanorings being involved with the lowest excited state are shown to be theoretically forbidden. The symmetry constraint for radiative transitions may be released via both static and dynamic distortions, particularly for larger rings, which are generally more flexible in solution. These artificially-synthesised porphyrin nanorings exhibiting electronic wavefunction delocalisation have analogies to those porphyrin ring assemblies found in natural light-harvesting systems. Moreover, the covalent bonding between adjacent porphyrin units may even provide the opportunity for these porphyrin nanorings to surpass their natural counterparts by offering more robust and wider delocalisation, which is not limited by disorder-induced weakening of the electronic coupling between porphyrin units. These findings open promising new opportunities for exploring the fundamental science of nanometer molecular rings and using these man-made light-harvesting systems as organic materials for organic photovoltaic applications.

## 4.2 Sample Preparation and Experiments

### 4.2.1 Synthesis and characterisation of porphyrins

All photoluminescence experiments were carried out in liquid solutions, where zinc porphyrin oligomers were molecularly-dissolved in toluene with 1% pyridine (volume concentration), whilst ***c*-P6·T6** and ***c*-P8·T8** were studied in pure toluene. The pyridine ligand coordinates to the zinc centres of the porphyrin units, increasing the solubility and preventing aggregation. The chemical structures of the zinc porphyrin oligomers and polymers used in this study are shown in Figure 4.1. These materials were synthesised by the research group of Harry Anderson at Oxford University and characterised by the group using previously published procedures [27, 103–110]. Monodisperse linear oligomers ***l*-P6** and ***l*-P8** were synthesised by coupling mono-silylated precursors as described in references [104, 107–110]. The polydisperse polymer ***l*-P40** was synthesised directly from the corresponding bis-ethynyl monomer ***l*-P1** (as described in ref. [108]) and purified by gel permeation chromatography (GPC); the chain-length distribution of this polymer was determined both by analytical GPC and by STM imaging (ref. [105]). The cyclic hexamer and its template complex, ***c*-P6** and ***c*-P6·T6**, were prepared directly from the porphyrin monomer ***l*-P1** as described in ref. [27]. The cyclic octamer and its template complex, ***c*-P8** and ***c*-P8·T8**, were prepared from ***l*-P2** using the **T8** template, using the method in ref. [105].

### 4.2.2 Time-resolved photoluminescence spectroscopy

The photoluminescence up-conversion spectroscopy described in Chapter 3 was used to detect the PL emission from samples held in a quartz cuvette with a time resolution of ∼500 fs. Samples were excited with the output of a mode-locked Ti:Sapphire laser providing pulses of 100 fs duration at a photon energy of 1.61 eV (770 nm) or 1.51 eV (820 nm) and a repetition rate of 80 MHz. For longer (>1 ns) time delays PL decay dynamics were resolved using electronic gating through time-correlated single-photon counting (TCSPC, Becker & Hickl),

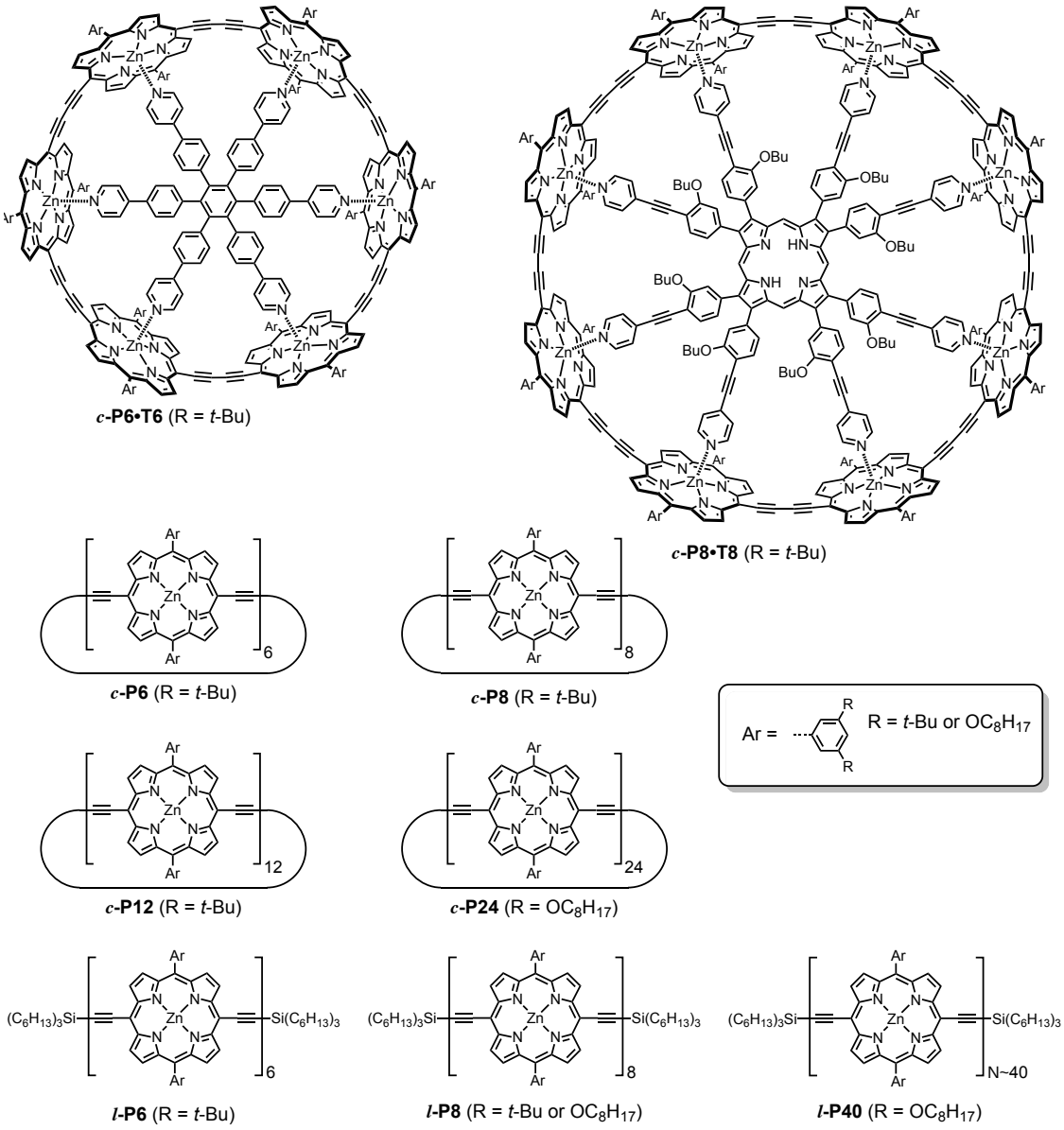


Figure 4.1: Chemical structures of the porphyrin oligomers and polymers used in this chapter. The sidechain (R) has no significant effect on the absorption or photoluminescence spectra of the compounds, but it influences the solubility, aggregation behaviour and ease of purification. The oligomers with R = t-Bu or R = $OC_8H_{17}$ were used, as indicated in the figure.

which is described in chapter 3, with a temporal resolution of 180 ps and detection based on a photomultiplier tube (PMT).

### 4.2.3 PL Intensity Transients

Time-dependent PL intensity decay transients were determined from the two measured intensity components ($I_{\parallel}$, with polarisation parallel, and $I_{\perp}$ with polarisation perpendicular to the excitation polarisation, respectively) as $I_{total} = I_{\parallel} + 2I_{\perp}$ and are plotted in Figure 4.8 for cyclic and Figure 4.9 for linear porphyrins. From monoexponential fits to these data ($I = I_0 \exp(-k_{total}t)$) the overall decay rate $k_{total}$ was determined, which is composed of both radiative ($k_r$) and non-radiative ($k_{nr}$) parts.

### 4.2.4 Quantum Yield

To determine the quantum yield of porphyrin compounds under investigation, the absorption spectra of the samples were first measured using a UV-VIS spectrophotometer. The solution concentration was set to ensure that the optical density of the absorption spectrum was below 0.05 over the whole spectral range in order to avoid re-absorption effects. Subsequently, the PL emission spectrum of compound **P** was measured in the range of 750-1280 nm, corrected for spectral response of the system, and integrated over this spectral range to yield $I_{\text{Emission}}(\mathbf{P})$. This procedure was applied to all investigated compounds including the porphyrin hexamer ***l*-P6** whose quantum yield had previously been determined [107] to be 0.08, and which hence served as a fluorescence standard. From the integrated area of the emission spectra ($I_{\text{Emission}}(\mathbf{P})$) and the absorbance at the excitation wavelength ($ABS_{\text{exc}}(\mathbf{P})$) the quantum yield $QY(\mathbf{P})$ of sample **P** was then determined using the following equation:

$$QY(\mathbf{P}) = \frac{I_{\text{Emission}}(\boldsymbol{l}\text{-}\mathbf{P6})}{I_{\text{Emission}}(\mathbf{P})} \times \frac{ABS_{\text{exc}}(\mathbf{P})}{ABS_{\text{exc}}(\boldsymbol{l}\text{-}\mathbf{P6})} \times 0.08.$$

The resulting values for the quantum yield measured by the research group of Harry Anderson are displayed in Table 4.1 for the investigated range of cyclic and linear porphyrins.

| Material | Quantum Yield |
|---|---|
| ***l*-P6** | 0.08 – ref. [107] |
| ***l*-P8** | 0.096 |
| ***l*-P40** | 0.044 |
| ***c*-P6** | 0.0043 |
| ***c*-P6·T6** | 0.0012 |
| ***c*-P8** | 0.018 |
| ***c*-P8·T8** | 0.007 |
| ***c*-P12** | 0.046 |
| ***c*-P24** | 0.0756 |

Table 4.1: Quantum yield of porphyrins measured by the research group of Harry Anderson.

## 4.3 Results and Discussion

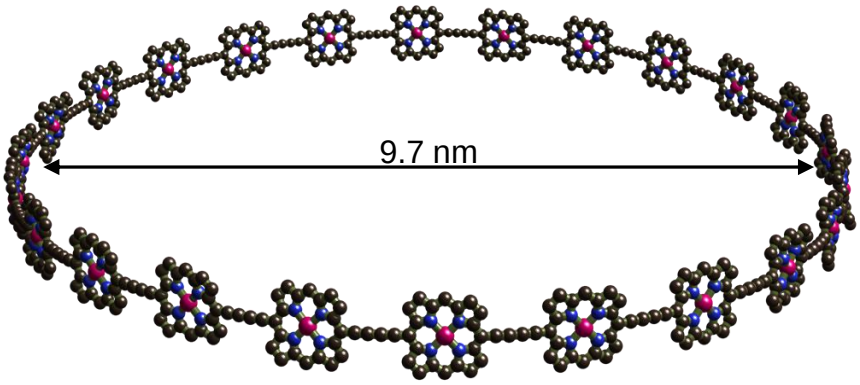


Figure 4.2: Simulated molecular structure of ***c*-P24** derived from Molecular Modelling simulation by the research group of Harry Anderson.

Figure 4.2 demonstrates the molecular structure of ***c*-P24** porphyrin ring by a Molecular Model done by the research group of Harry Anderson. The diameter of this ***c*-P24** porphyrin ring joined by butadiyne bridges is found to be $\approx 9.7\,\text{nm}$, which is significantly larger than the porphyrin ring assemblys found in natural light harvesting system 2 (LH-2) [93] and comparable to the porphyrin ring assembles found in light harvesting system 1 (LH-1) of bacterium Rhodospirillum rubrum [111].

Figure 4.3 shows the steady-state absorption and time-integrated emission spectra of ***c*-P6**, ***c*-P8**, ***c*-P12** and ***c*-P24** porphyrin rings. The $\pi$-conjugation through the butadiyne-bridged lifts the degeneracy of the lowest-energy Q-band of the porphyrin monomer into

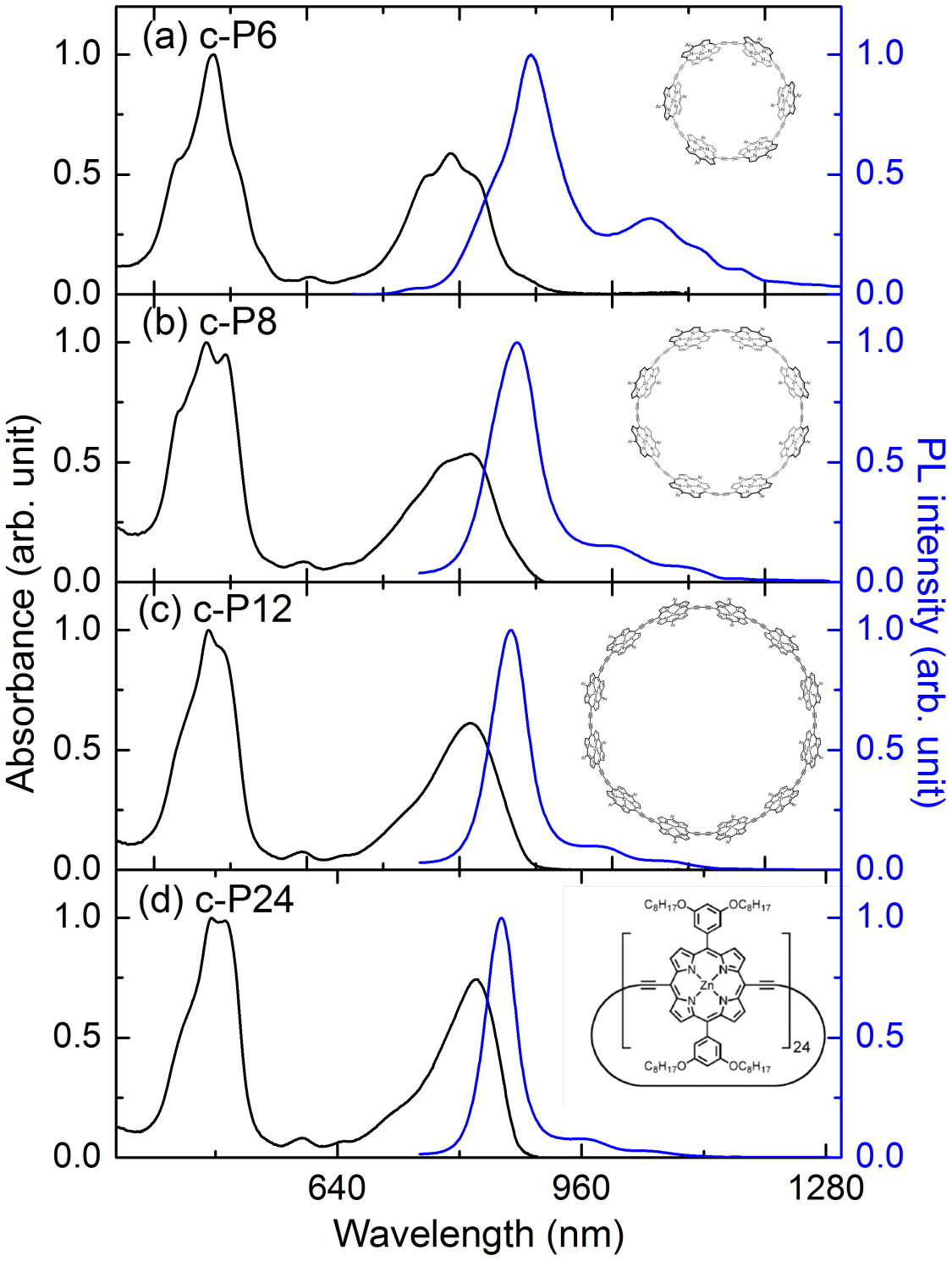


Figure 4.3: Normalized steady-state absorption (black lines) and photoluminescence (blue lines) spectra at 295 K of cyclic porphyrins (a) ***c*-P6**, (b) ***c*-P8**, (c) ***c*-P12** and (d) ***c*-P24** in toluene/1% pyridine. The emission was recorded after excitation at 770 nm (1.61 eV).

transitions polarised parallel ($Q_x$) and perpendicular ($Q_y$) to the molecular backbone. The $Q_y$ transition remains weakly visible in the absorption spectra at 600 nm for the full series of rings; however, the spectroscopic absorption intensity of $Q_x$ is raised and it is red-shifted with respect to the Soret band (400–500 nm) concomitantly with increasing the number of porphyrin units ($n$). It indicates that the effective conjugation is lengthened with increasing the length of the perimeter of the rings. Furthermore, the emission spectra, collected after excitation with an ultrashort laser pulse at photon wavelength of 770 nm, show a gradual blue-shift and spectral-narrowing, as $n$ is increased from 6 to 24.

The effort of synthesising porphyrin cyclic structures with various sizes in the past cannot effectively enhance their conjugation length, as only marginal red-shifts of the $Q_x$-band compared with the monomer appear in the absorption spectra [13, 14, 112, 113]. Therefore, only partial electronic delocalisation is achieved in subunits of those nanostructures; as a result the excitation energy transfer occurs via incoherent hopping between segments over a few picoseconds after the excitation [12, 13]. For example, partial electronic delocalisation on the macrocycle thiophene rings synthesised by McMurry coupling has recently been observed [114, 115]. In contrast, the synthesis method using a suitable template facilitates the creation of ring-like molecules without incorporating kinked molecules for ring closure, and it allows excellent $\pi$-conjugation properties throughout the entire ring. The recent advent of Vernier templating [103] which has successfully synthesised a series of porphyrin macrocycles as the largest version as 9.7 nm was used by the Anderson group to synthesise the materials investigated in this Chapter.

### 4.3.1 Anisotropy of PL Polarisation of Nanorings

PL upconversion measurements by selectively exciting the nanomaterials at a photon wavelength of 770 nm were performed to examine the electronic delocalisation as a function of their sizes, and the PL emission dynamics were monitored at the emission peak energy of the nanomaterials. The excitation wavelength of 770 nm was chosen in order to promote electrons to the band $Q_x$ with transitions along the backbone of linear porphyrin molecules,

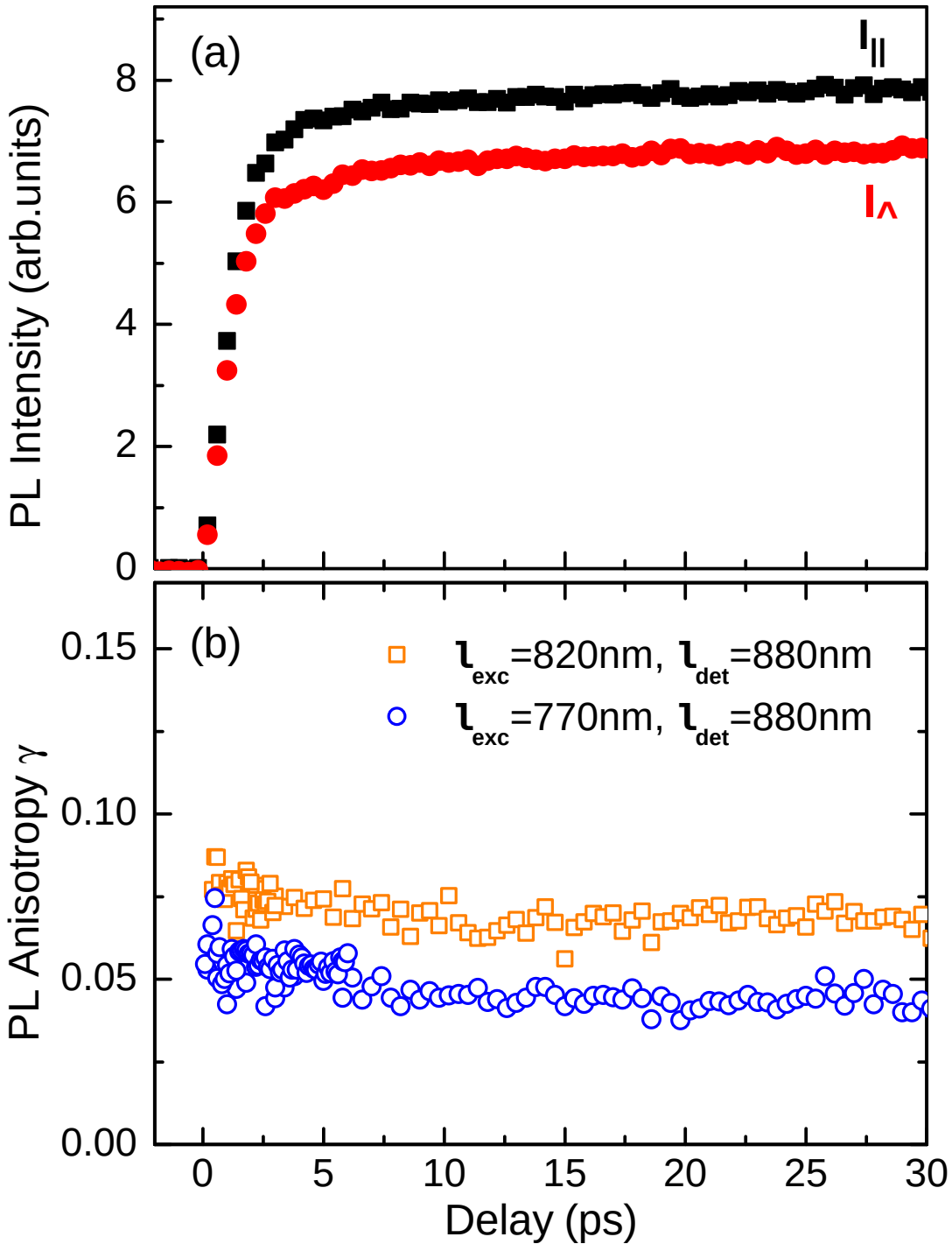


Figure 4.4: (a) PL emission transients of ***c*-P24** in toluene/1% pyridine for excitation at a photon wavelength of 770 nm and detection at 880 nm. The collected parallely- and perpendicularly-polarised PL of solution samples are denoted as $I_{\parallel}$, black squares, and $I_{\perp}$, red circles, respectively. (b) The derived PL polarisation anisotropy $\gamma = (I_{\parallel} - I_{\perp})/(I_{\parallel} + 2I_{\perp})$ as a function of time delay after excitation at 770 nm and 820 nm, and detection at 880 nm. It is noted that measurements with excitation at 770 nm and detection at 870 nm give identical results to those with excitation at 770 nm and detection at 880 nm.

where the spectroscopic splitting between the $Q_x$ and the $Q_y$ transitions indicates that selective excitation of the nanoring near the $Q_y$ band will create the other excited state with well-defined transitions perpendicularly to the $Q_x$ band [116, 117]. The excitation fluence was kept low ($0.15\,\mu\mathrm{Jcm}^{-2}$) in order to prevent the unintended PL quenching via exciton-exciton annihilation [118]. Figure 4.4a shows the PL transient of ***c*-P24** nanorings probed at the emission wavelength of 880 nm. The samples were photoexcited with pulse polarisation either parallel ($I_{\parallel}$) or perpendicular ($I_{\perp}$) with equal energy to the detection polarisation. The PL anisotropy $\gamma$ can be extracted from the relationship: $\gamma = (I_{\parallel} - I_{\perp})/(I_{\parallel} + 2I_{\perp})$. An initial PL anisotropy $\gamma(0)$ of 0.4 is expected in the absence of any depolarisation mechanisms, when motionless linear molecules are randomly orientated in solution, whilst $\gamma(0) = 0.1$ can be expected when full polarisation memory loss occurs in a 2D plane [119, 120]. However, additional depolarisation mechanisms may arise, for instance, by out-of-plane distortion of nanorings, which will further lower the value of $\gamma$.

Figure 4.4b shows the evolution of $\gamma$ as a function of time delay after the polarised excitation pulse. For the ***c*-P24** rings, it is observed that within the observation window of 30 ps after excitation, $\gamma$ remains essentially constant, suggesting full electronic delocalisation has already occurred on an ultrafast time scale and slow molecular re-orientation are absent. The value of $\gamma$ is found to be dependent of the excitation energy but is independent of the detection energy. Exciting ***c*-P24** at the high-energy edge of the $Q_x$ band absorption results in a relatively low value of $\gamma(0) = 0.056$, suggesting that significant out-of-plane distortions are possible for the largest rings. When the ***c*-P24** is excited near the red edge of the absorption spectrum at a photon wavelength of 820 nm, the $\gamma$ is recovered from 0.05 towards the value expected for full excitation delocalization on planar rings. These measurements therefore demonstrate that the absorbing state is fully delocalised even in the largest ***c*-P24** rings, with a range of conformations present in the ensembles.

Similarly, $\gamma$ of the rest of the cyclic and linear porphyrin molecules, such as ***l*-P6**, ***l*-P8**, ***l*-P40**, ***c*-P6**, ***c*-P6·T6**, ***c*-P8**, ***c*-P8·T8** and ***c*-P12** were revealed using the same experimental methods, as shown in Figure 4.5. In Figure 4.6, the initial PL anisotropies

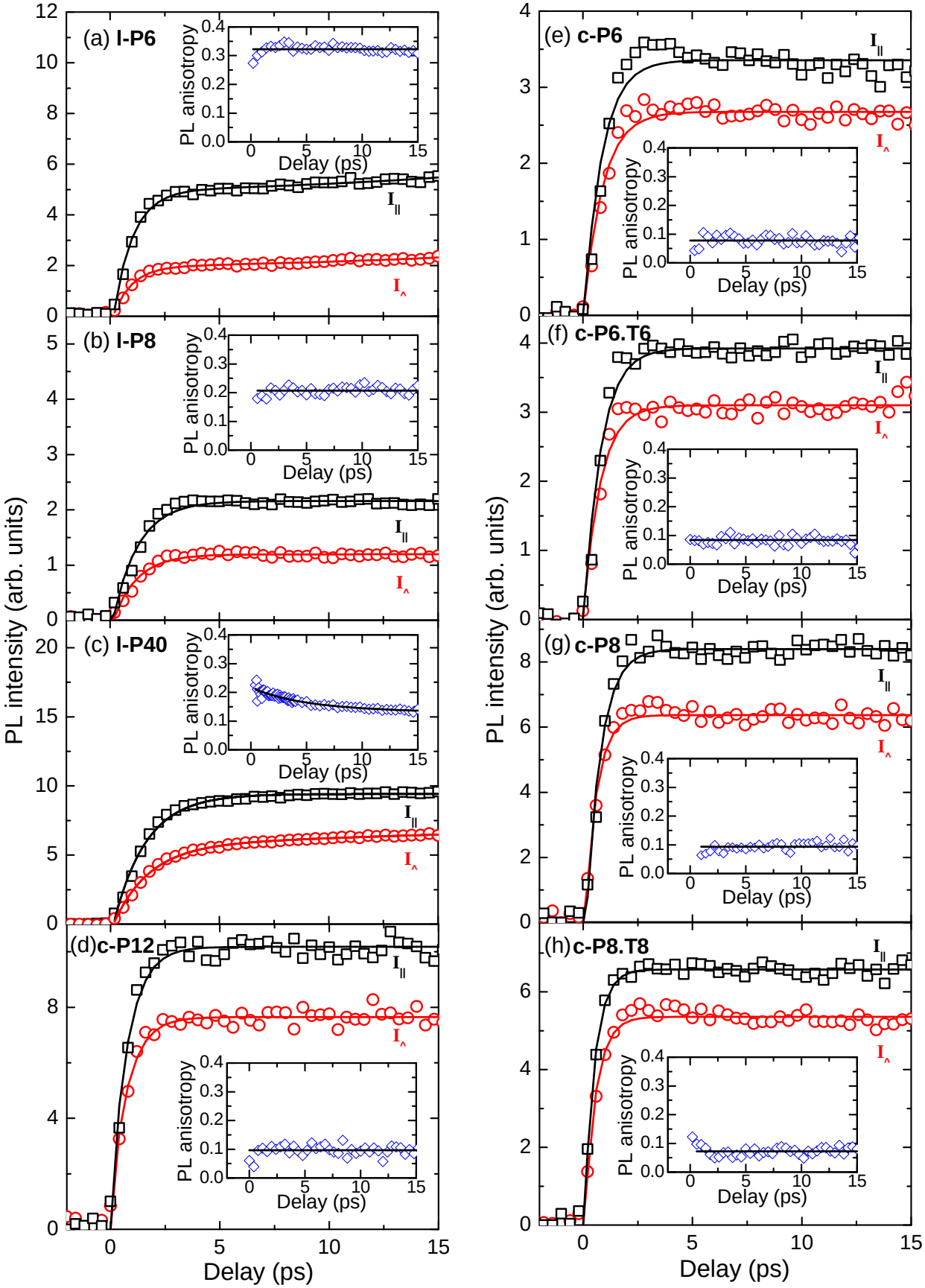


Figure 4.5: PL transients of (a) ***l*-P6**, (b) ***l*-P8**, (c) ***l*-P40**, (d) ***c*-P12**, (e) ***c*-P6**, (f) ***c*-P6·T6**, (g) ***c*-P8** and (h) ***c*-P8·T8** after excitation at 770 nm and detection at the emission wavelength corresponding to the peak emission of their steady-state PL spectra. The collected PL polarised parallel and perpendicular to the polarisation of the excitation pulse are denoted as $I_{\parallel}$, black squares, and $I_{\perp}$, red circles, respectively. Insets: The calculated PL anisotropy of polarisation $\gamma$ as a function of time. The solid lines are guides to the eye.

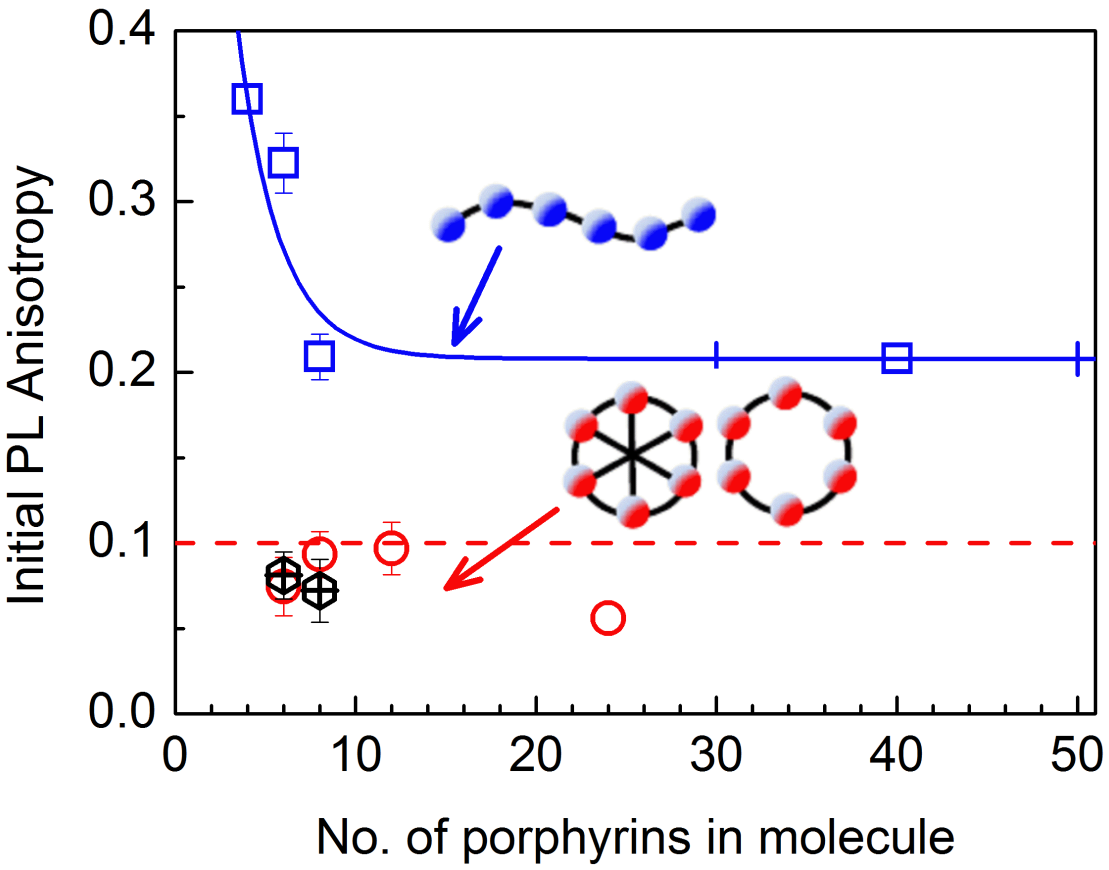


Figure 4.6: Initial PL polarisation anisotropy within the first few hundred femtoseconds after excitation as a function of the number of porphyrins contained in the molecule, for free nanorings (red circles), templated nanorings (black hexagons with cross) and oligomers and polymers (blue squares). All lines are guides to the eye.

of all samples after the short pulse excitation demonstrate two clear trend curves with a function of the number of porphyrin units. The PL anisotropy of a cyclic nanoring has a value just below 0.1 regardless of its size, and whether it is sterically constrained to a rigid cyclic shape using a template (***c*-P6·T6** and ***c*-P8·T8**, as shown in Figure 4.1), and drops to 0.056 for the largest (***c*-P24**). It suggests that larger rings are more susceptible to deformations. Therefore, complete polarisation memory loss in an out-of-2D plane is observed for nanorings incorporating between 6 and 24 porphyrin units on an ultrafast time scale. On the other hand, linear oligomers and polymers of similar number of porphyrin units keep a significantly higher fraction of their polarisation memory in the same experimental conditions. The PL anisotropy lower than the value of 0.4 has attributed to their worm-like structures naturally existing in solution, particularly for longer linear chains [117]. This observation is in agreement with the higher fraction of initial exciton delocalisation for oligomers incorporating up to eight porphyrins. However, a polymer containing porphyrin statistically between 30 and 50 units possesses a similar polarisation memory loss as that of an oligomer with 8 porphyrin units, which suggests that kinked and bent structures in a polymer may break its conjugation, and therefore it can be considered as a combination of subunits with an effective conjugation length not longer than 8 porphyrin units.

The observed ultrafast excitation delocalisation across a full porphyrin ring of diameter up to 9.7 nm is remarkable and represents the longest delocalisation length among synthetic molecular rings examined at present. The B850 comprising 18 individual porphyrin bacteriochlorophyll (BChl) units with diameter of $\approx 2.5$ nm formed by assembly of porphyrin pigments in the LH-2 system is proven experimentally and theoretically to exhibit similar rapid depolarisation of the excited state, although the excitation wave packet is contracted within a time constant of $\approx$50 fs owning to disorder-induced localisation [97, 99, 100, 121]. The overall process leads to PL anisotropy values of $\leq$0.1 to be assumed within a time scale of $\approx$100 fs when B850 is probed in absorption [122] and emission [98] spectroscopy, similar to the values found for the synthetic systems in this Chapter.

### 4.3.2 Radiative Transition Rates of Nanorings

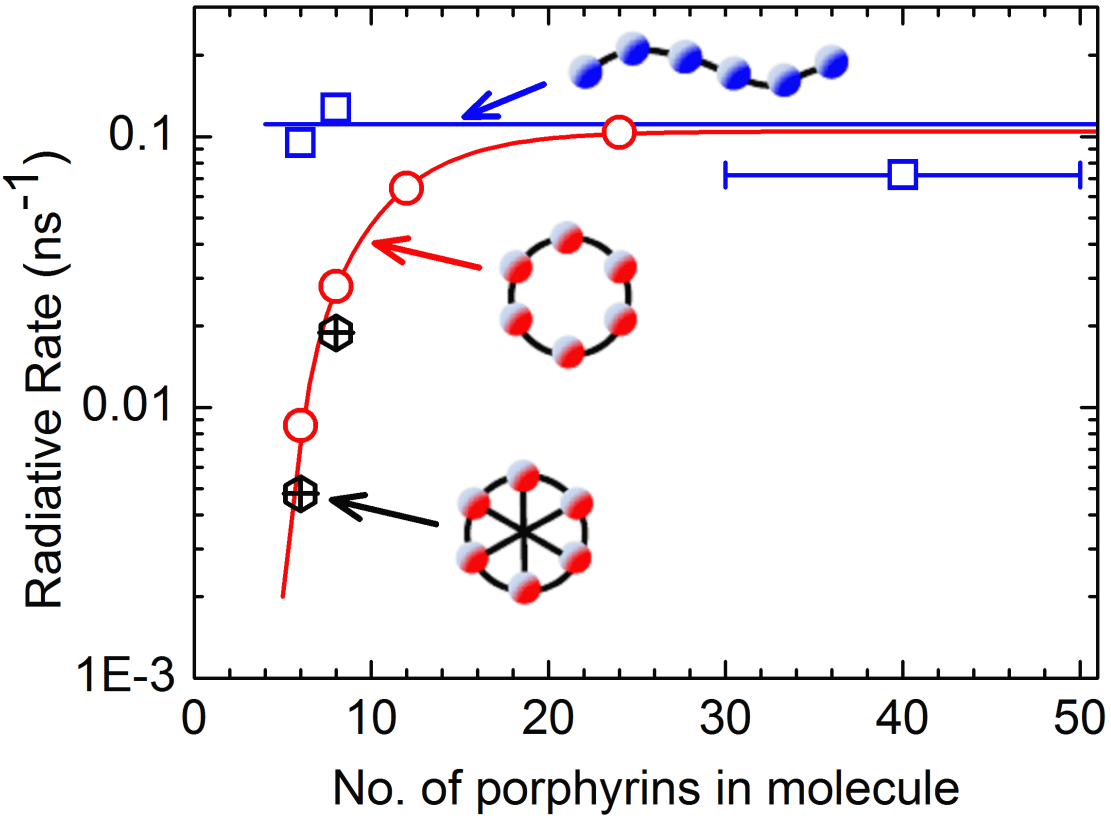


Figure 4.7: Radiative transition rate as a function of the number of porphyrins in the molecule. The transition rates for free porphyrin nanorings, templated porphyrin nanorings and porphyrin linear oligomers are represented by the red open circles, black open hexagons with cross and blue open squares, respectively. All lines are guides to the eye.

To examine the subsequent evolution of the emitting dipole moment on the nanorings, their radiative rates were determined. Figure 4.7 displays the radiative emission rate for circular and linear molecules as a function of the number of porphyrins incorporated, which were calculated from the polarisation-independent decay traces of total photoluminescence intensity, as shown in Figure 4.8 and Figure 4.9, combined with the fluorescence quantum yields (Table 4.1). It is noted that the radiative rates for $n = 6$–$8$ porphyrin oligomers are relatively the same because of their similar conjugation lengths, whilst a $n \approx 40$ porphyrin polymer possessing a lower radiative rate than that of the oligomers may be attributed to the PL quenching owning to the existence of trapping states induced by its kinked and bent structures. It is observed that a dramatic radiative rate rise of almost two orders of magni-

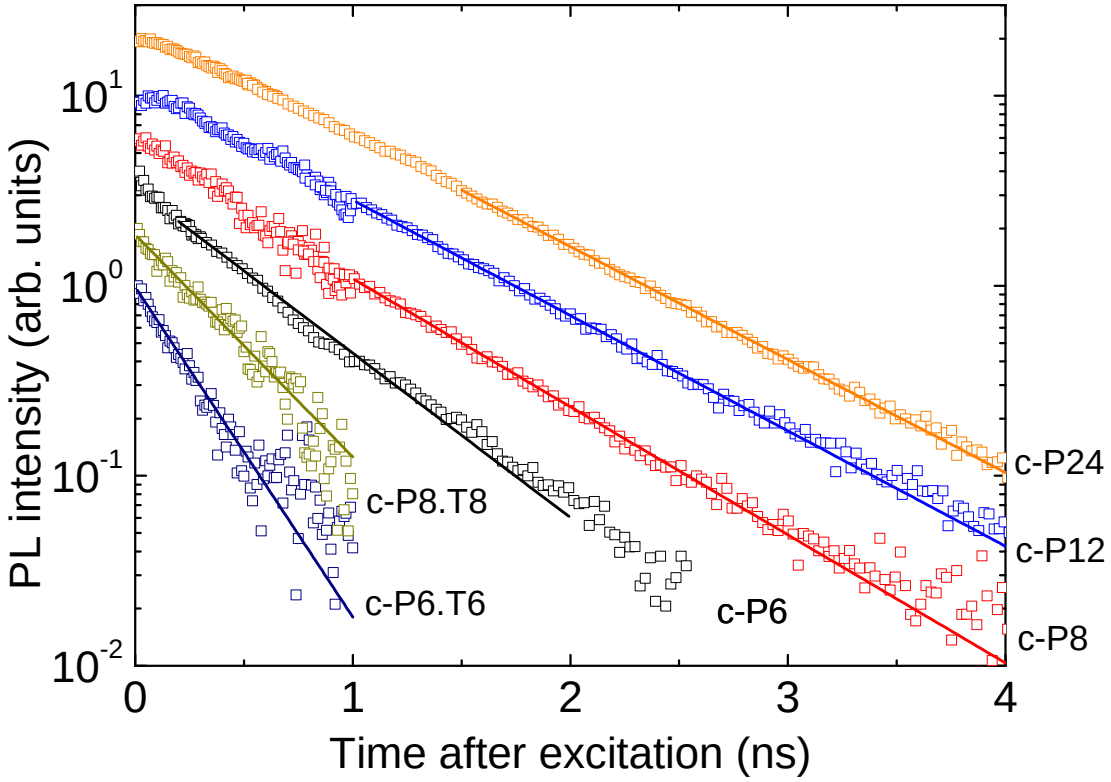


Figure 4.8: PL transients of templated porphyrin nanorings ***c*-P6·T6** and ***c*-P8·T8** in toluene and free nanorings ***c*-P6**, ***c*-P8**, ***c*-P12** and ***c*-P24** in toluene/ 1% pyridine detected at the emission wavelength corresponding to the peak emission of their steady-state PL. The solid lines are fitting from single-exponential function from which the total decay rate was extracted.

tude when the nanoring size increases from 6 to 24 porphyrin units. Particularly, for smaller porphyrin structures ($n = 6$–$8$), circular molecules have radiative rates that are 1–2 orders of magnitude lower than those of their linear counterparts. These results are reminiscent of the situation for other small ring-like molecules such as benzene [123, 124] and porphyrin ring assemblies in natural light-harvesting systems [94, 125], whose electronic transitions from the lowest excited state to the ground state are forbidden due to the symmetry of their structures. Figure 4.7 displays the radiative rates of the lowest emitting states constrained by the circular symmetry of structures are significantly increased for large ($n = 24$) porphyrin nanorings. A key to the mechanisms behind this effect is obtained when comparing the $n = 6$, and 8 nanorings that are fixed with rigidifying templates to those template-free. The rings with freedom to distort have significantly higher emission rates than identical rings that are constrained by a template into a more rigid ring-like geometry. Hence, deviations from ring-like symmetry are most likely the cause of the recovery in emission strength and this appears to be more effective for larger rings.

Such distortion can be either static (on the time scale of the excitation) or dynamic, where the latter may result from the coupling with suitable vibrations that may induce dynamic self-localisation or intensity borrowing from higher-lying states of different symmetry. Figure 4.10 illustrates how these two mechanisms influence the strength of the electronic transition moment. In most cases, polyatomic molecules can be well described under the Franck-Condon (FC) principle, assuming that electronic transitions occur much more rapidly than the accompanying nuclear vibrations [126, 127]. Under such approximations, the overall moment for the coupled vibronic transition may be factorised into its electronic part $\boldsymbol{\mu}_e$ and its vibrational overlap integral. For molecules with certain high symmetries, such as benzene [128] or buckminster fullerene ($C_{60}$) [129], the lowest electronic transition becomes dipole-forbidden, $(\boldsymbol{\mu}_e)_{eq} \approx 0$. However, some emission may be observed through Herzberg-Teller (HT) intensity borrowing, by involving a non-totally symmetric vibration in a coupled electronic-vibrational transition. As a result, intensity can be "borrowed" from a higher-lying electronically allowed state of symmetry that matches the coupled symmetry of the lowest state and the involved vibration [126, 127]. Such Herzberg-Teller transitions may

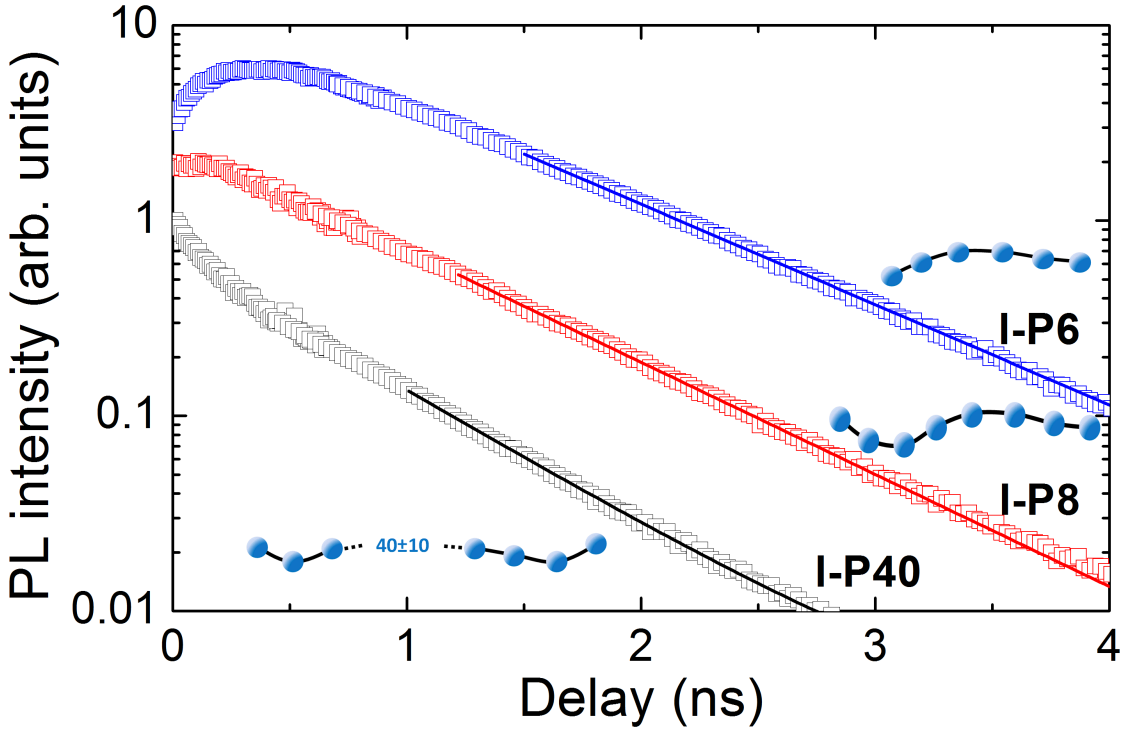


Figure 4.9: PL transients of ***l*-P6**, ***l*-P8** and ***l*-P40** in toluene/ 1% pyridine detected at the emission wavelength corresponding to the peak emission of their steady-state PL (***l*-P6**: 876 nm, ***l*-P8**: 856 nm, ***l*-P40**: 867 nm). The solid lines are fitting from single-exponential function from which the total decay rate was extracted.

be explained in terms of a breakdown of the Franck-Condon approximation, allowing the electronic transition moment to be expanded into a Taylor series in the normal coordinates $Q_k$ associated with the relevant vibrations (Figure 4.10). The low emission rate of ***c*-P6** illustrates (Figure 4.7) transitions rates are weak for this rigid, highly symmetric molecule, suggesting $(\boldsymbol{\mu}_e)_{eq} \approx 0$. Larger porphyrin nanorings, on the other hand, are mechanically more flexible and so can allow direct FC transitions as a result of a static relaxation in symmetry constraints ($(\boldsymbol{\mu}_e)_{eq} > 0$). Such effects will allow a recovery of the radiative emission rates towards those of their linear porphyrin analogues as shown in Figure 4.7. This interpretation is consistent with the results of an excitation-energy dependent emission anisotropy for ***c*-P24** (Figure 4.4b) and the scanning tunneling microscopy (STM) images [103, 106, 130] of larger porphyrin rings revealing significant structural deformation. These observations have direct analogues with natural porphyrin ring assemblies such as B850 for which the lowest ($k$=0) coupled exciton state is known to be dipole forbidden due to symmetry [131]. However, distortion from circularity and general disorder have been shown to energetically split the higher lying ($k$=±1) states and transfer oscillator strength to the $k$=0 state [125, 131, 132].

## 4.4 Conclusion

In this chapter, time-resolved photoluminescence spectroscopy was carried out for the investigation of spatial distribution of electronic states after excitation in a series of fully $\pi$-conjugated porphyrin nanorings. The initial PL anisotropy of polarisation smaller than 0.1 in all of the sizes of nanorings suggests that full delocalisation of excited states occurs in nanorings including diameters up to ∼10 nm, which is the largest artificially-synthesised molecular nanoring at present. Although the circular symmetry of their structures theoretically limits the radiative transition involved in the lowest-lying excited state to the ground state in all nanorings, the deviation from the ideal ring-like symmetry by distortions can relax this constraint. The static distortion plays an important role in the more flexible larger nanorings and dramatically raise their radiative decay rates, whilst the dynamic distortion dominating in smaller rings can induce dynamic self-localisation or intensity borrowing from

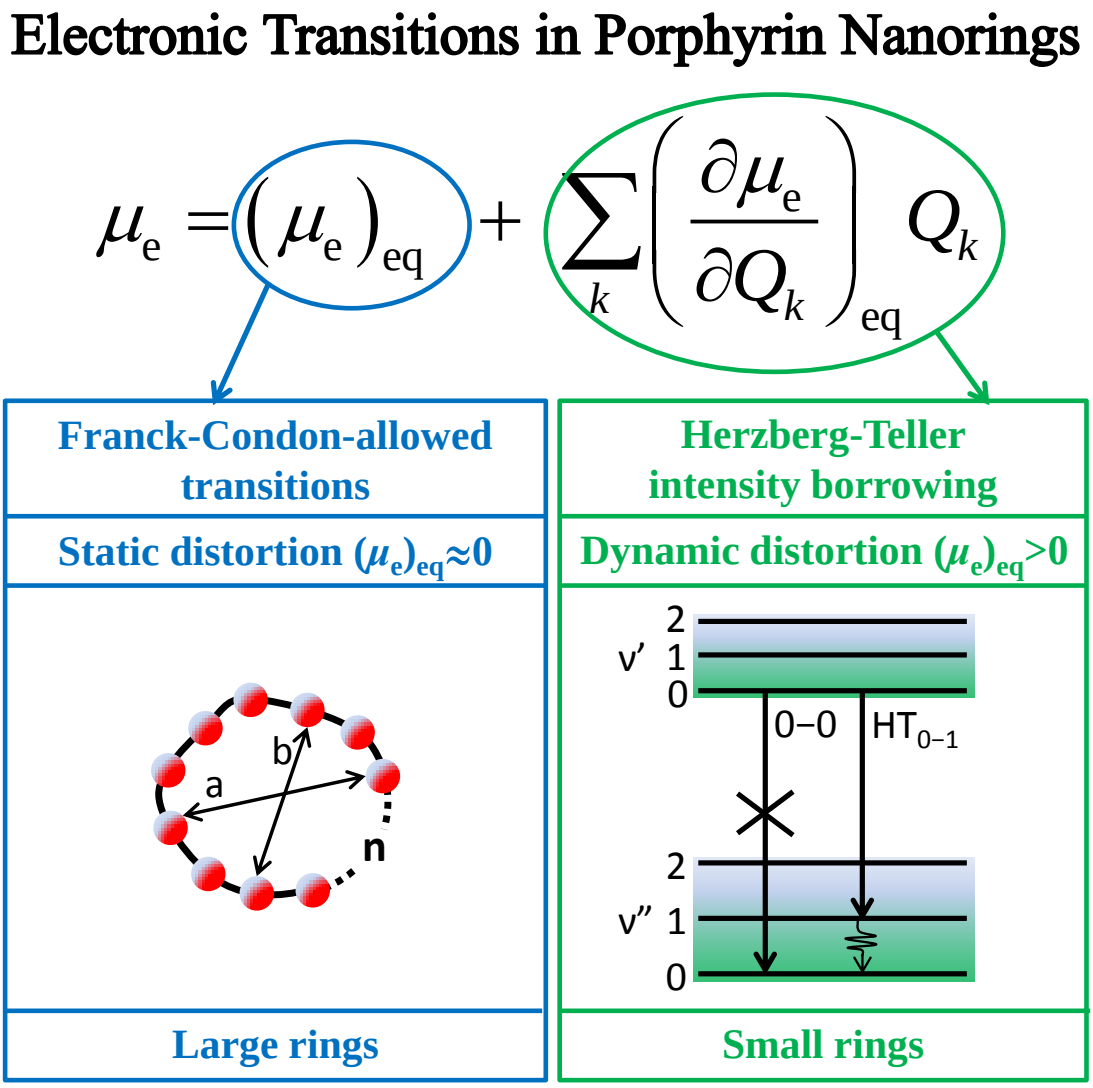


Figure 4.10: Schematic diagram illustrating the processes leading to coupled electronic–vibrational transitions in porphyrin nanorings. The electronic transition moment $\boldsymbol{\mu}_e$ may be developed into a Taylor series in the normal coordinates $Q_k$ of the vibrations involved in the transition. Large rings are more flexible, and hence static distortions from symmetry yield lowest vibronic transitions that are allowed within the standard Franck-Condon approximation, $(\boldsymbol{\mu}_e)_{eq} \geq 0$. For small rings, $(\boldsymbol{\mu}_e)_{eq} \approx 0$ as a result of the high symmetry, but Herzberg-Teller intensity borrowing from higher-lying allowed transitions may lead to emission from the lowest state through involvement of a nontotally symmetric vibration.

the higher-lying states of different symmetry via coupling with suitable vibrations, which can be explained by the Herzberg-Teller approximation. These results open up a whole host of technological applications for light-harvesting materials that match the efficiency of their natural counterparts, and allow for an exploration of the fundamental science of large molecular macrocycles supporting spatially coherent electronic states.

# Chapter 5

# Excitation Energy Transfer in Organic Self-Assembled Nanoparticles of Amphiphilic Monomers with Targeting Ligands

## 5.1 Introduction and Background

Fluorescent nanomaterials with modified surface characteristics have gained considerable interest in bio-imaging, bio-sensing and drug delivery for decades [18, 133–136]. A quantum dot (QD), possessing excellent photoluminescence properties, including high quantum yield, narrow and size-dependant emission spectra, large molar extinction coefficient and high resistance against photobleaching, is one of the most promising candidates for biological applications [19–21, 137, 138]. However, their cores formed usually by noble metals or inorganic semiconductors lead to potential bio-toxicity to the human body, especially nephrotoxicity [139] via endocytosis [22, 24]. For solving the problem of toxicity, biocompatible organic fluorescent materials are adopted. Traditional organic dyes used as labeling in bio-systems have been widely commercialized but have disadvantages of low absorption

coefficients, weak fluorescent and low stability, which means it is difficult to have a high signal-to-noise ratio and long-term observation before photobleaching occurs [137]. Many attempts have been made to incorporate nanoparticles (NPs) with organic dyes [140], but these nanoparticles may inherit the intrinsic weaknesses as described above. A fluorescent $\pi$-conjugated nanoparticle may combine the advantages of inorganic QDs and dyes, which means no additional dyes need to be incorporated into a nanoparticle, and its organic components are not toxic to cells. Nanoparticles formed by polydispersed polymers have the fluorescence properties based on their chemical structures and multiple interactions between random aggregates [23], whilst nanoparticles formed by monodispersed oligomers tend to allow for more precise control of the morphology. The conformation of the molecules within nanoparticles formed by oligomers could be driven by only the structures and the lengths of stiff segments and soft coils instead of their intrinsic chemical properties [141]. With careful design, nanoparticles can fulfil the requirement of forming suitable sizes in order to move freely through human tissues and organs after being injected into the circulatory system [142–144]. In addition, surface functionalisation plays a crucial role for nanoparticles to be utilised in bio-systems. Functional groups can be covalently or non-covalently attached to the surface of nanoparticles, so that the binding affinity to a specific target is tuned; therefore, nanoparticles are able to automatically direct themselves to targets *in vivo* or *in vitro* [18, 24]. For the purpose of amplification of fluorescence brightness in bio-sensing and bio-labelling, excitation energy needs to be harvested and transported to energy acceptors on nanoparticles [145]. Hence, the strategy of creating energetic cascades to funnel excitons to specific quencher sites [146, 147] is expected to display enhanced emission of fluorescent acceptors.

In this chapter, homotransfer and heterotransfer of excitation energy in self-assembled nanoparticles in water have been investigated by time-resolved photoluminescence spectroscopy. The transient PL spectra measurements in a 8 ns observation window show that nanoparticles formed with a higher molar fraction of mannose exhibit larger red-shifts in average energy of exciton emission, and therefore faster exciton migration through energetic cascades to sites with lower energy. The study of Förster resonance energy transfer from NP

chromophores to ConA/AF633 acceptors, which are bound onto the surface of nanoparticles via mannose, proves that a higher molar fraction of mannose in nanoparticles raises the energy transfer rate more significantly. In addition, Amp3-B monomers in nanoparticles can create more energetically favorable routes for excitons towards the surface to perform direct energy transfer from Amp3-B monomers to ConA/AF633 acceptors. This is due to the fact that Amp3-B monomers possess the lowest energy levels and a higher probability to stay on the surface of nanoparticles. As a result, higher energy transfer rates were observed in Amp3-B/Amp1-B-mannose NPs. Nevertheless, increasing the number of Amp3-B monomers will lead to a decreased number of Amp1-B-mannose on the NP surface, so optimisation of the molar ratios of these two monomers is important for engineering the energy transfer rate in the system for the purpose of a high signal-to-noise ConA/AF633 emission. These findings provide opportunities for the new carbohydrate-coated organic amphiphilic nanoparticles to be used in biological sensing and labelling applications.

## 5.2 Samples and Experimental Details

### 5.2.1 Characterization of Amphiphilic Monomers

Studied amphiphilic coil-rod-coil monomers [148, 149] are synthesised by the research group of A. P. H. J. Schenning and shown in Figure 5.1a. The stiff core of the amphiphilic rod is composed of two hydrophobic aminofluorene boronic esters, which are linked by a benzothiadiazole dibromo linker by the metal-catalysed aryl-aryl Suzuki coupling method [150]. One of the chromophores is decorated with an acid chloride of gallic acid derivatives, on which hydrophobic alkyl chains are attached. The other side of the chromophore is connected by gallic acid derivatives as well but with ethylene glycol chains. In this chapter, there are three kinds of amphiphilic monomers: (1) Amp1-B, (2) Amp1-B-mannose and (3) Amp3-B, where “Amp” and “B” are the abbreviations of “Amphiphile” and “benzothiadiazole dibromo linker”, respectively. The head and end tails of these three monomers are hydrophobic and hydrophilic side chains, respectively, which are responsible for the phase separation in wa-

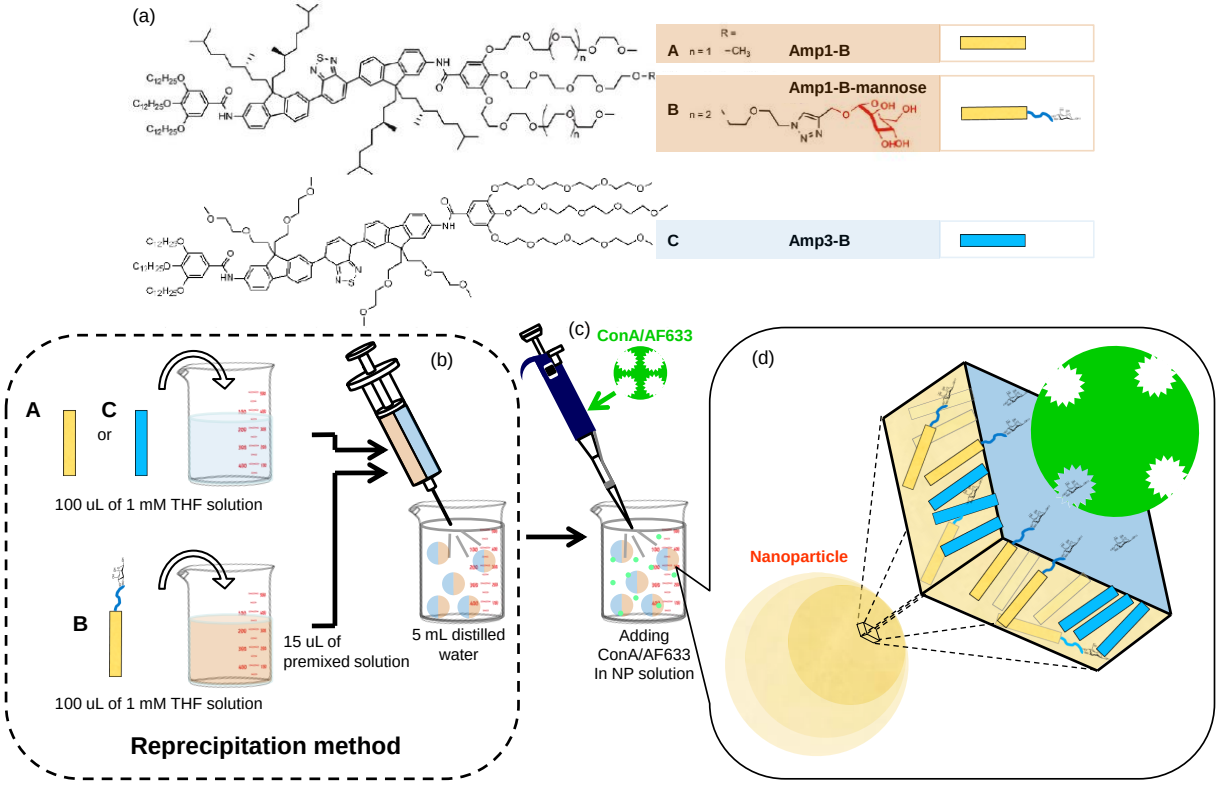


(e)

| NP | 1 | 2 | 3 | 4 | 5 | 6 | 7 |
|---|---|---|---|---|---|---|---|
| Amp1-B-mannose | 100 % | 0 % | 10 % | 90 % | 0 % | 10 % | 90 % |
| Amp1-B | 0 % | 100 % | 90 % | 10 % | 0 % | 0 % | 0 % |
| Amp3-B | 0 % | 0 % | 0 % | 0 % | 100 % | 90 % | 10 % |

Figure 5.1: Schematic illustration of the sample preparation to form self-assembled nanoparticles attached by ConA/AF633. (a) The molecular structures of three types of amphiphilic monomers (Amp1-B, Amp1-B-mannose and Amp3-B) synthesised by the Schenning group. (b) Nanoparticles are formed by the reprecipitation method, where different molar fraction of monomers are premixed in Tetrahydrofuran (THF) and subsequently fast injected into a large amount of distilled water. (c) and (d) Consequently, 15-750 nM of ConA/AF633 is added into nanoparticle solution made of 300 nM of amphiphilic monomers, where ConA/AF633 can be bound on nanoparticles via mannose to realize Förster resonance energy transfer (FRET) from the excitons on chromophores to ConA-carried AF633 under pulsed laser excitation. (e) Seven compositions of NPs used in this chapter are listed.

ter [141, 151]. In addition, the ethylene glycol chains have the properties of (1) excellent water solubility and (2) reducing unspecific adsorption to the nanoparticles [148].

An $\alpha$-D-mannosyl group could be functionalised on the ethylene glycol chain of Amp1-B to provide a ligand for its binding target, and the whole monomer is termed Amp1-B-mannose [152]. Due to phase separation, in the layer near the NP surface, hydrophilic chains have the inclination to point out to water molecules, so some of the mannose covalently attached on those hydrophilic chains are able to stay on the NP surface. It is noted that the arrangement of monomers inside NPs is amorphous, as treated by a study of transmission electron microscopy (TEM) [148]. The difference between Amp1-B and Amp3-B is that their side chains are hydrophobic and hydrophilic for Amp1-B and Amp3-B, respectively. Various molar ratios of monomers are mixed with one another to form self-assembled NPs in distilled water, for the investigation of the influence of side chains and targeting ligands on transient fluorescent properties and excitation energy transfer in nanoparticles. All of the samples are listed at the table in Figure 5.1e.

### 5.2.2 Introduction to Conconavalin A

Conconavalin A (ConA) is a lectin and also a metalloprotein extracted from jack bean, which can recognize residues of $\alpha$-D-mannosyl and $\alpha$-D-glucosyl groups. ConA exists as a tetramer in the experiment due to the pH 7.0 10 mM NaPi buffer solution, and it has 4 binding pockets (receptors) in total for monosaccharides [153, 154]. When binding to these mannose residues, each ConA needs one manganese and one calcium ion simultaneously to bind to its receptors to be activated, increasing its affinity towards mannose which is linked by hydrogen bonds [153].

### 5.2.3 Sample Preparation

The reprecipitation method [155] shown in Figure 5.1b was adopted to form nanoparticles. A specific molar fraction of functional $\alpha$-D-mannosyl group on the surface of nanoparticles

directly originate from the molar fraction of Amp1-B-mannose premixed with Amp1-B or Amp3-B monomers in Tetrahydrofuran (THF). The mixed THF solution was fast injected into a relatively large amount of distilled water to form self-assembled nanoparticles according to their thermodynamic behaviour in solution [156]. For instance, in order to obtain 10 % Amp1-B and 90 % Amp1-B-mannose in one nanoparticle, 20 $\mu$L Amp1-B and 180 $\mu$L Amp1-B-mannose 1 mM THF stack solution were premixed, and then 15 $\mu$L of the premixed solution was taken out by a pipette and fast injected into 5 mL distilled water.

For the investigation of Förster resonance energy transfer (FRET) between chromophores in nanoparticles and fluorescent dye acceptor (Alexa Fluor 633, AF633), ConA was used as a carrier, on which AF633 is covalently linked, to target and bind to the mannose on the NP surface, as illustrated in Figure 5.1d. Various concentrations of ConA/AF633, 15–750 nM, added into the solution with self-assembled nanoparticles will lead to various amounts of acceptors being attached on the NP surface, as illustrated in Figures 5.1c and 5.1d. Consequently, 100 $\mu$L of the solution containing nanoparticles, 900 $\mu$L of 10 mM NaPi buffer, 1 $\mu$L $CuCl_2$, 1$\mu$L $MnCl_2$ and various concentrations of ConA/AF633 are mixed in the quartz cuvette for static and transient PL measurements.

### 5.2.4 Measurement of Transient Photoluminescence Decay

The basic principle of time-correlated single photon counting (TCSPC), which performs the time-resolved PL measurement, is described in Chapter 3. The laser pulse with excitation power of 50 $\mu$W possesses a central wavelength of 425 nm, which arises from a fundamental laser beam frequency-doubled by a $\beta$-barium-borate (BBO) nonlinear crystal, and photons are collected at various wavelengths of the emission PL of NP chromophores. Förster resonance energy transfer can be observed by time-resolved PL measurements and characterised by the decreased lifetime of the donor transient decay.

## 5.3 Results and Discussion

### 5.3.1 Transient Fluorescent Characteristics of Nanoparticles

Figure 5.2a shows the absorption and emission spectra of Amp1-B NPs and Amp3-B NPs dissolved in distilled water and the corresponding monomers in THF solution. In Figure 5.2b, the emission spectra of the nanoparticles and monomers in distilled water and THF are shown respectively. Whilst the emission energy of the monomers with different side chains remain essentially unchanged, their corresponding nanoparticles show different emission energy. On the other hand, whilst the emission energy of Amp1-B NPs is blue-shifted with respect to their monomers, the spectrum becomes red-shifted for Amp3-B NPs. By increasing the molar ratio of mannose in the nanoparticles, the PL emission energy of Amp3-B NPs was gradually blue-shifted, as seen in the inset of 5.2b. However, such effect was not observed in Amp1-B NPs. It is noted that the effect of side chain on the optical properties of Amp1-B and Amp3-B monomers can be ruled out, since the absorption and emission properties remain essentially identical in these two monomers. Hence, the distinguishable emission spectra observed in Amp1-B NPs and Amp3-B NPs are attributed to the effects of different molecular packing in the aggregates when self-assembled in the distilled water to form nanoparticles [157, 158]. This is further supported by the observation of emission spectra where the emission energy of Amp3-B NPs gradually blue-shifted and converged with the emission energy observed in Amp1-B NPs, when the molar ratio of mannose in the NPs is increased.

Figure 5.3 and Figure 5.4 show the transient PL spectral map for monomers and nanoparticles, respectively, where the vertical axis shows the time after the laser excitation pulse, and the horizontal axis shows the emission energy of the collected photons. The false-colour mapping is on the linear scale. Figure 5.5 shows the average emission energy of the investigated samples. The average emission energy of monomers remains essentially unchanged over the 8 ns observation window; however, a sizeable decrease of emission energy over the 8 ns observation window was observed for all nanoparticles. It is found that the emission energy of Amp3-B NPs decreases faster than that in Amp1-B NPs (Figure 5.4 and Figure

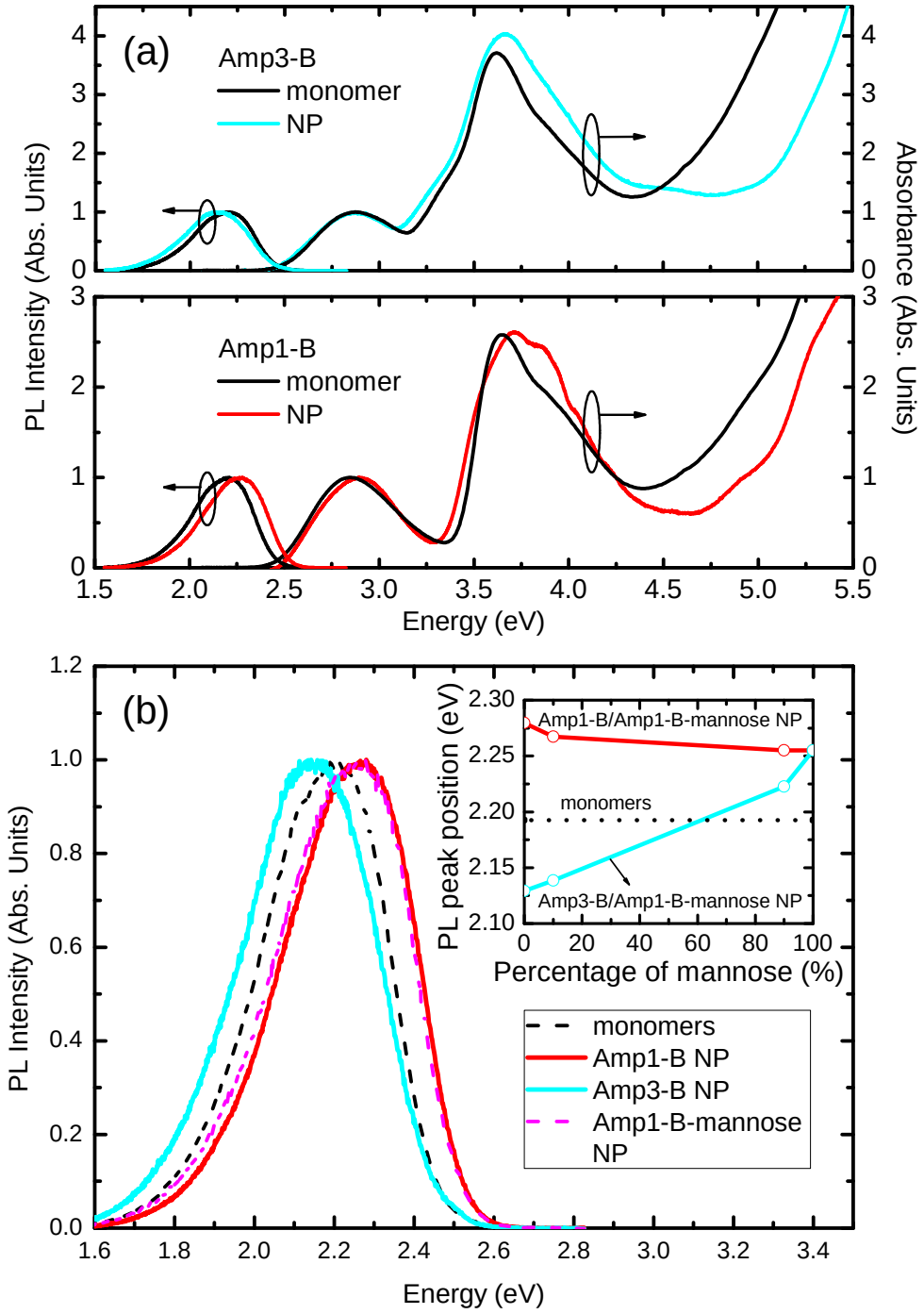


Figure 5.2: (a) Absorption and emission spectra of Amp1-B and Amp3-B monomers dissolved in THF or aggregated to form NPs in distilled water. (b) Time-integrated PL spectra of Amp1-B NPs, Amp1-B-mannose NPs and Amp3-B NPs in distilled water. The emission spectra of Amp1-B, Amp1-B-mannose and Amp3-B monomers dissolved in THF are also shown. The inset shows the emission peak energy of the Amp1-B NPs and Amp3-B NPs with various molar ratio of mannose.

5.5). Furthermore, nanoparticles formed with a higher molar ratio of mannose also show a higher degree of decrease of emission energy over the 8 ns observation window, as compared with the nanoparticles without mannose attachment.

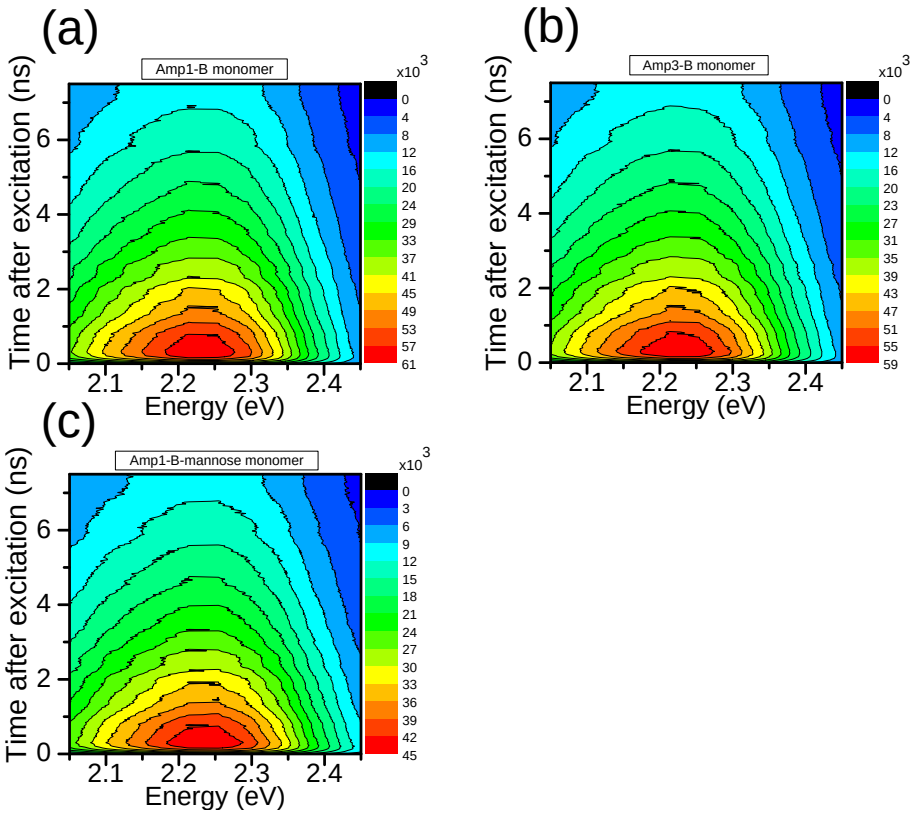


Figure 5.3: Time-resolved PL spectral map for (a) Amp1-B (b) Amp3-B and (c) Amp1-B-mannose monomers in THF showing the intensity (on a linear false colour scale) as a function of time delay (vertical scale) and emission energy (horizontal scale).

The larger energy red shift observed in the time-resolved PL mapping over the 8 ns observation window is associated with faster exciton migration, which indicates that excitons are hopping to sites with lower energy in the nanoparticles. Increasing the molar ratio of Amp1-B-mannose and introducing Amp3-B in nanoparticles further enhance this process; for instance, larger emission energy red-shifts were observed in the Amp1-B (10%)/Amp1-B-mannose (90%) NPs as compared to the Amp1-B (90%)/Amp1-B-mannose (10%) NPs, and in the Amp3-B (10%)/Amp1-B-mannose (90%) NPs as compared to the Amp1-B (10%)/Amp1-B-mannose (90%) NPs. These results strongly suggest that the presence of mannose and in particular Amp3-B monomer in the nanoparticles provides pathways for excitons to hop to such lower energy sites: exciton migration towards the sites of Amp1-

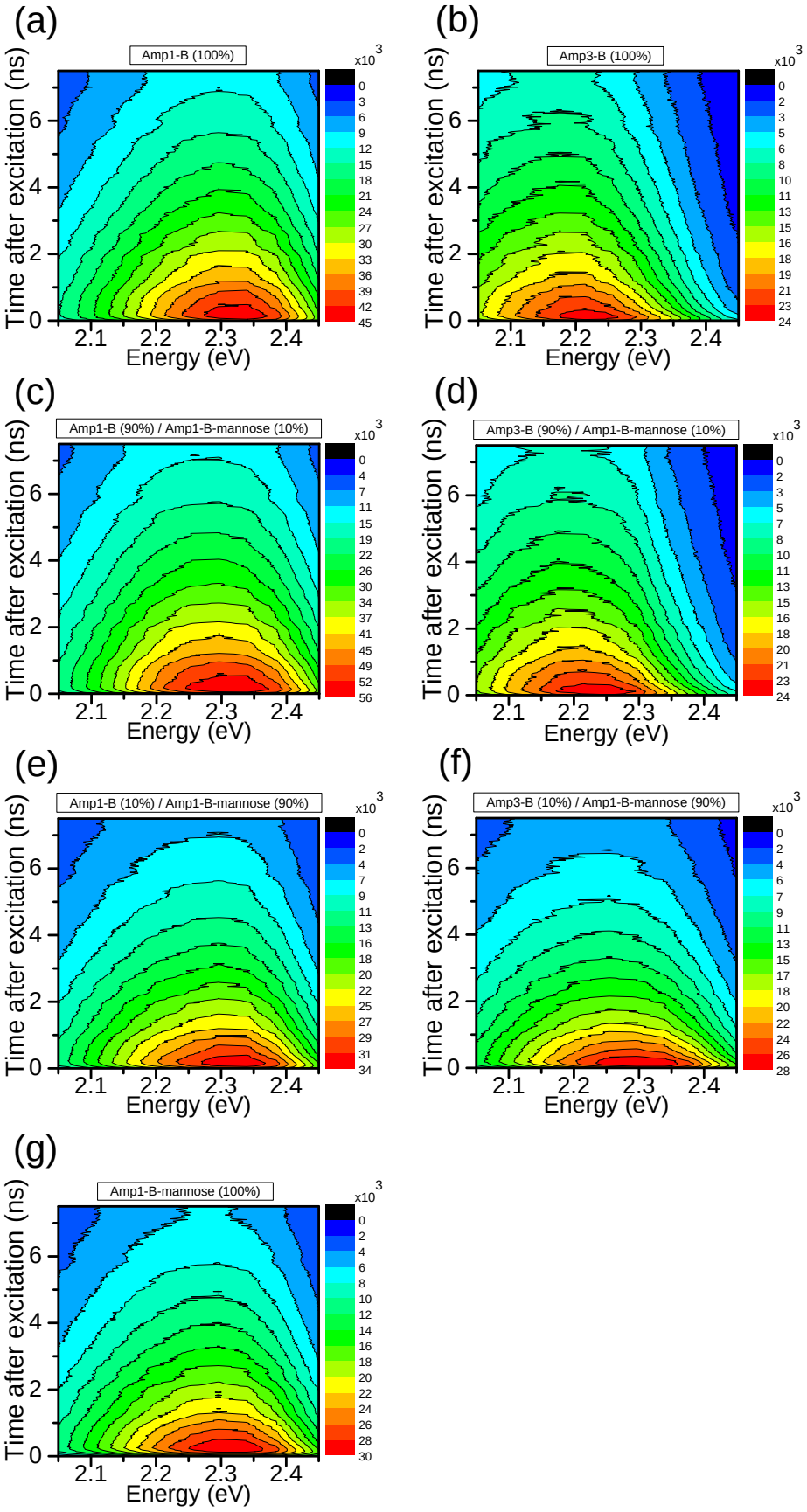


Figure 5.4: Time-resolved PL spectral map for (a) Amp1-B (b) Amp3-B (c) Amp1-B (90%)/Amp1-B-mannose (10%) (d) Amp3-B (90%)/Amp1-B-mannose (10%) (e) Amp1-B (10%)/Amp1-B-mannose (90%) (f) Amp3-B (10%)/Amp1-B-mannose (90%) and (g) Amp1-B-mannose NPs showing the intensity (on a linear false colour scale) as a function of time delay (vertical scale) and emission energy (horizontal scale).

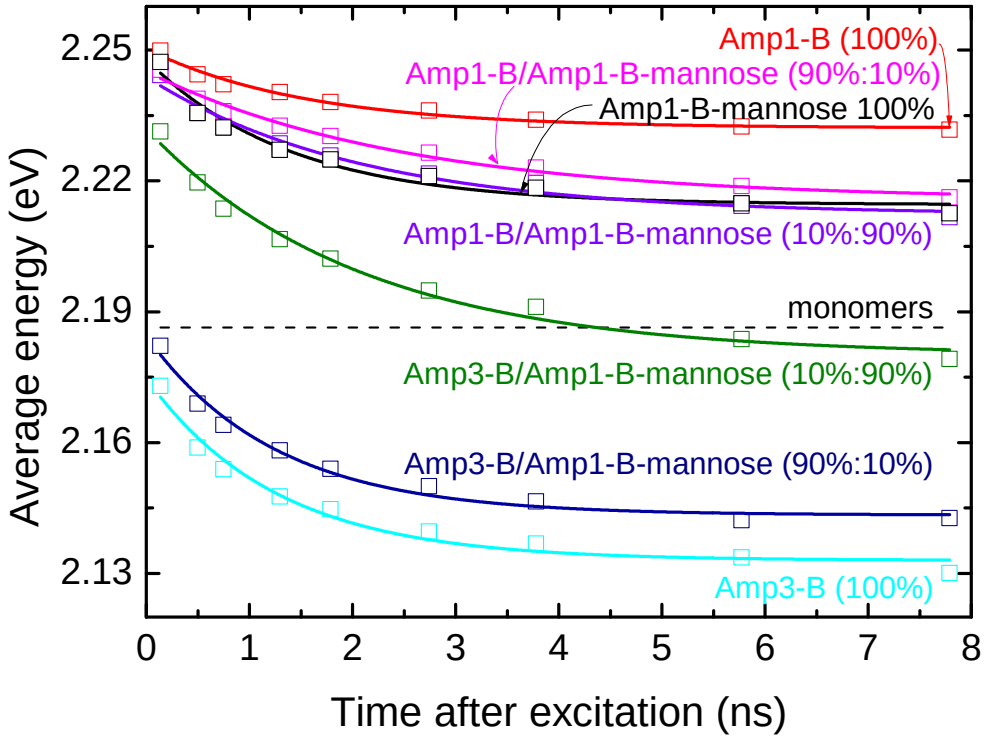


Figure 5.5: Average emission energy as a function of time delay after photoexcitation for all samples. The solid lines are guides to the eye.

B-mannose or Amp3-B monomers resembles going down an energetic cascade. Hence, the exciton emission energy will gradually red-shift at longer time delay, as the exciton gradually hops into sites with lower energy.

### 5.3.2 Energy Transfer between Nanoparticles and Attached Acceptors

The energy shifts in the emission show that the nanoparticles investigated in this chapter not only differ in the side chains on the monomers but also the energy migration rate along the amphiphilic monomers. To examine the energy transfer from NP donor to acceptor, ConA/AF633 acceptors were added to the solution containing the nanoparticles, where the absorbance spectrum of ConA/AF633 acceptors have a broad spectral overlap with the PL emission of nanoparticles to realize resonance energy transfer. It should be noted that the ConA/AF633 acceptors can be effectively bound to the nanoparticles via the

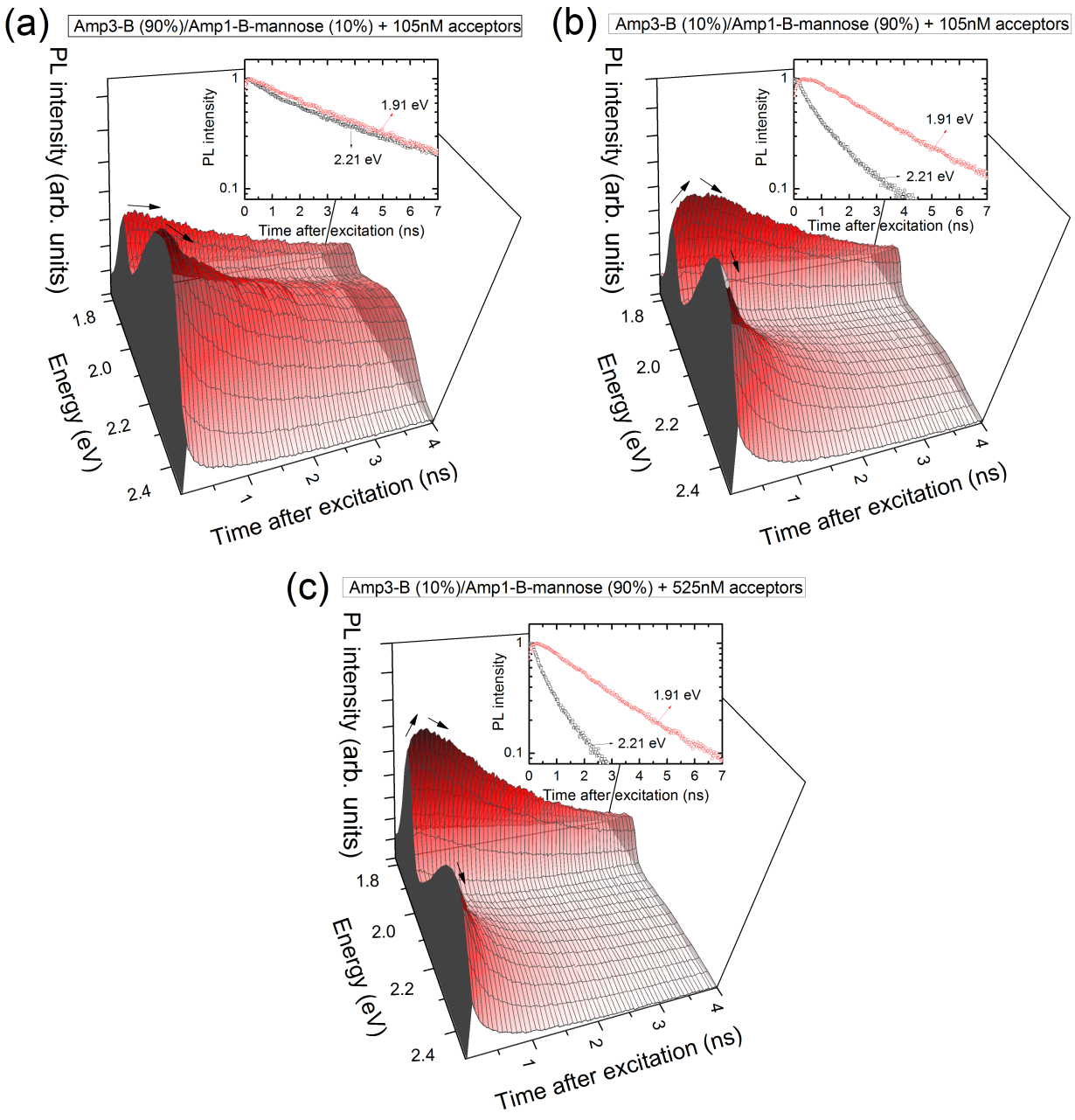


Figure 5.6: Time evolution of PL spectra of (a) Amp3-B (90%)/Amp1-B-mannose (10%) NPs with 105 nM, and Amp3-B (10%)/Amp1-B-mannose (90%) NPs with (b) 105 nM ConA/AF633 and (c) 525 nM ConA/AF633. The insets are PL transients detected at peak positions of the emission of NPs (black squares, 2.21 eV) and AF633 (red circles, 1.91 eV).

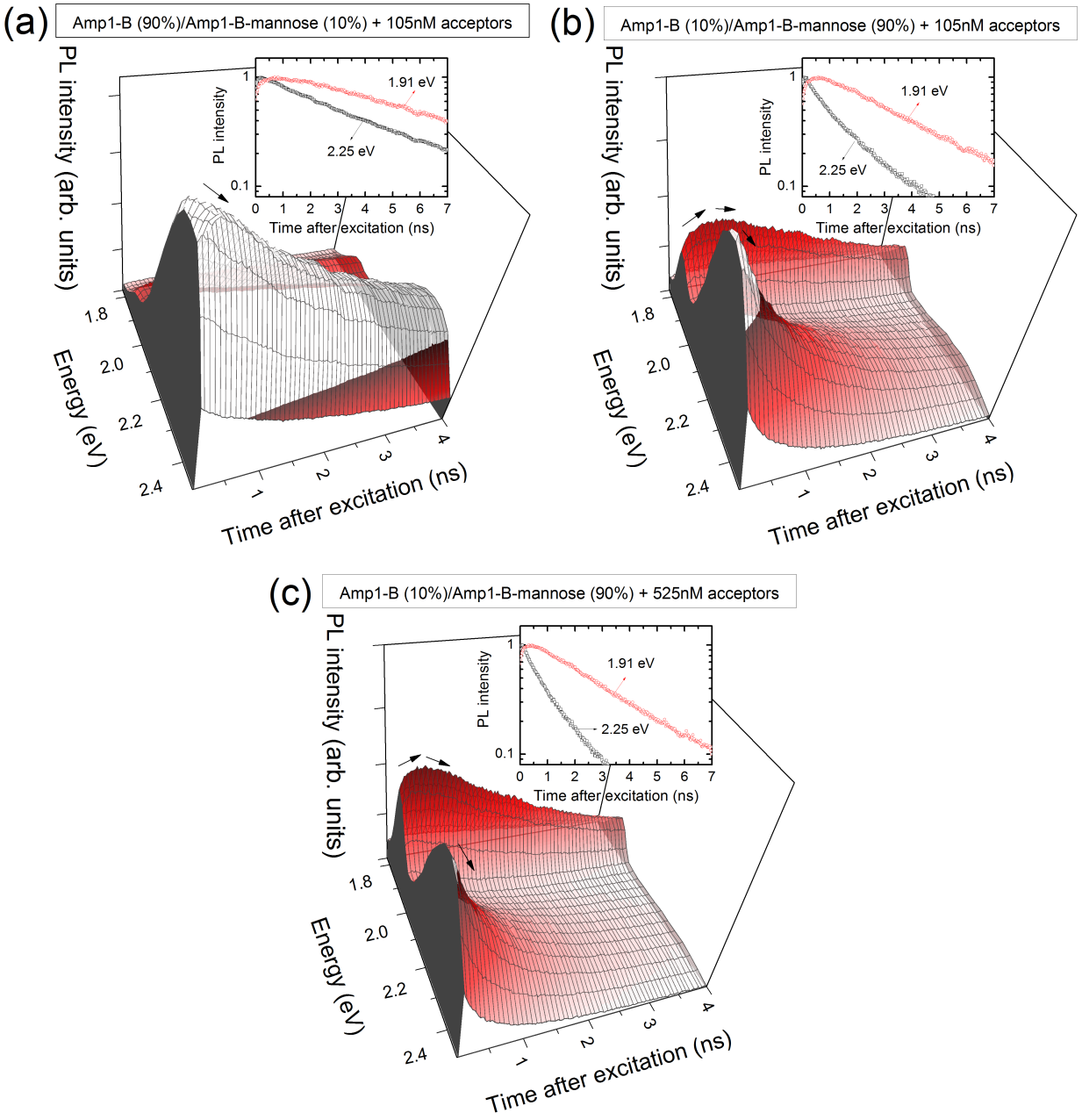


Figure 5.7: Time evolution of PL spectra of (a) Amp1-B (90%)/Amp1-B-mannose (10%) NPs with 105 nM, and Amp1-B (10%)/Amp1-B-mannose (90%) NPs with (b) 105 nM ConA/AF633 and (c) 525 nM ConA/AF633. The insets are PL transients detected at peak positions of the emission of NPs (black squares, 2.25 eV) and AF633 (red circles, 1.91 eV).

mannose, which serves as ligand to bind the donor and acceptor. Figure 5.6a,b show the time-resolved spectral mapping for Amp3-B (90%)/Amp1-B-mannose (10%) NPs and Amp3-B (10%)/Amp1-B-mannose (90%) NPs after injection of 105 nM ConA/AF633 acceptor to the solution. The insets in Figure 5.6 show the transient PL probed at the peak emission energy of nanoparticles (2.21 eV) and acceptors (1.91 eV). It was found that the PL decay in the Amp3-B (90%)/Amp1-B-mannose (10%) NPs remains essentially unchanged after the injection of ConA/AF633 acceptor into the solution (Figure 5.6a). In marked contrast, significant PL decay and enhanced emission of ConA/AF633 acceptor were observed in the Amp3-B (10%)/Amp1-B-mannose (90%) NPs after the injection of the same concentration of ConA/AF633 acceptor into the solution (Figure 5.6b). This suggests the efficient energy transfer between the NP donor and ConA/AF633 acceptor can only occur for nanoparticles consisting of high molar ratio of Amp1-B-mannose. A similar observation was made for the Amp1-B/Amp1-B-mannose NPs with ConA/AF633 acceptor system, as shown in Figure 5.7a,b. As the injection concentration of ConA/AF633 acceptor is further increased, the PL decay rate of nanoparticles becomes faster, as seen in Figure 5.6c and Figure 5.7c. These results clearly suggest that the efficient energy transfer between the nanoparticles and ConA/AF633 acceptor strongly depends on the molar ratio of mannose in the nanoparticles to provide binding sites for the ConA/AF633 acceptor. This further implies that the energy transfer between the nanoparticle and ConA/AF633 acceptor is limited by their relative distance in the solution, where binding of ConA/AF633 acceptor on the surface of nanoparticles is required to achieve efficient energy transfer. In order to estimate the distance requested for efficient energy transfer, the Förster radius is calculated, which defines the distance between the donor and acceptor at which energy transfer efficiency of 50% is reached, from the established Förster equation [79]:

$$R_0 = \left[ \frac{9000 \ln(10)}{128\pi^5 N_A} \frac{\kappa^2 \phi_D}{n^4} \frac{\int_0^\infty F_D(\nu)\epsilon_A(\nu)\nu^{-4} d\nu}{\int_0^\infty F_D(\nu) d\nu} \right]^{\frac{1}{6}}, \tag{5.1}$$

where $N_A$ is Avogadro's constant; $\kappa^2$ is the dipole orientation factor; $\phi_D$ is the fluorescence quantum yield of the donor in the absence of acceptor; $n$ is the refractive index of the mate-

rial; $F_D(\nu)$ is the fluorescence spectrum of the donor NP; $\epsilon_A(\nu)$ is the molar extinction coefficient of the acceptor. The refractive index of NPs is approximated as 1.5, which represents an amorphous polymer film [159], and $\kappa^2$ is estimated to be $(0.845\sqrt{2/3})^2 = 0.476$, which is in agreement with the model of random distribution but fixed dipoles [160]. It is calculated from Equation 5.1 that the $R_0$ for energy transfer between Amp1-B NPs and ConA/AF633, and between Amp3-B NPs and ConA/AF633 is 5.69 nm and 5.45 nm, respectively. The Förster radius observed in these two systems indicates that efficient energy transfer between the nanoparticle and ConA/AF633 acceptor dissolved in the solution without the linkage on the surface of nanoparticles is highly unlikely.

In order to further understand the dynamics of energy transfer in these nanoparticles with ConA/AF633 acceptors, a model is constructed based on coupled rate equations in order to account for exciton generation ($G$), the PL decay rate of the nanoparticle ($k_D$) and acceptor ($k_A$), and the energy transfer rate ($k_{DA}$). The energy transfer process can then be modelled as following [161–163]:

$$\frac{d}{dt}n_D(t) = G(t) - k_D n_D(t) - \frac{1}{2}\left(\frac{k_{DA}}{t}\right)^{\gamma} n_D(t) \tag{5.2}$$

$$\frac{d}{dt}n_A(t) = \frac{1}{2}\left(\frac{k_{DA}}{t}\right)^{\gamma} n_D(t) - k_A n_A(t), \tag{5.3}$$

where $n_D(t)$ and $n_A(t)$ are the population of excitons in NPs and AF633, respectively. $\gamma$ is a characteristic constant, which is 0.5 for a three dimensional system [161–163]. The term $\frac{1}{2}\left(\frac{k_{DA}}{t}\right)^{\gamma}$ accounts for the dynamic change of energy transfer rate over time as a result of progressive depletion of acceptor that captures the excitations. For a $\delta$–function like excitation at zero time delay ($\Delta$t = 0), the solution of $n_D(t)$, assuming $\gamma = 0.5$, is given by

$$n_D(t) = n_D(0)exp[-k_D t - (k_{DA}t)^{0.5}]. \tag{5.4}$$

To extract the dynamics of energy transfer, the measured PL transient of nanoparticles

with acceptors was divided by the PL transient of nanoparticles, and the energy transfer rate $k_{DA}$ can be extracted by fitting the data with the stretched exponential function with a stretching constant $\gamma$ of 0.5. The outputs from such fitting procedures are shown in Figure 5.8 for all investigated nanoparticles. Figure 5.9 plots the energy transfer rate $k_{DA}$ extracted in this manner as a function of ConA/AF633 acceptor concentration. Again, the dynamics of energy transfer between the nanoparticles and acceptors ($k_{DA}$) depends crucially on the molar fraction of mannose, which serves as ligands to bind the ConA/AF633 acceptors onto the nanoparticles. Nanoparticles with no mannose show negligible energy transfer to the acceptor, because no efficient energy transfer is able to occur when the distance between donor and acceptor is much larger than the Förster radius found in these systems. It is noted that when the concentration of ConA/AF633 is lower than ∼100 nM, Amp3-B NPs possess slower energy transfer rate than Amp1-B NPs, which can be attributed to more ethylene glycol chains on each Amp3-B monomer and therefore reducing unspecific adsorption of ConA/AF633 to the surface of nanoparticles. As the molar fraction of the mannose was increased from 10% to 90%, a sharp increase in energy transfer rate was observed. In addition, for nanoparticles with a high molar fraction of mannose (90%), $k_{DA}$ rises rapidly as the concentration of acceptor injected into the solution is increased. These results therefore indicate that efficient energy transfer from NP donor to acceptor in a system can only occur for nanoparticles with suitable ligand attachment. It further suggests the targeting properties of the investigated organic nanoparticles can be used in biological labeling and sensing purposes [23, 148].

Interestingly, the energy transfer rate across the Amp3-B/Amp1-B-mannose NPs with ConA/AF633 acceptors was found to be significantly higher than that observed in the Amp1-B/Amp1-B-mannose NPs with ConA/AF633 acceptors, for a given concentration of mannose and acceptor. As mentioned above, the Förster radius calculated for these two systems are nearly identical, which suggests that the energy transfer efficiency in these two systems is highly likely to be similar. However, for the case of nanoparticles with a high molar ratio of mannose (90%), where binding between ConA/AF633 and nanoparticles is highly possible, a clear difference of the energy transfer rate is readily observed even at low acceptor

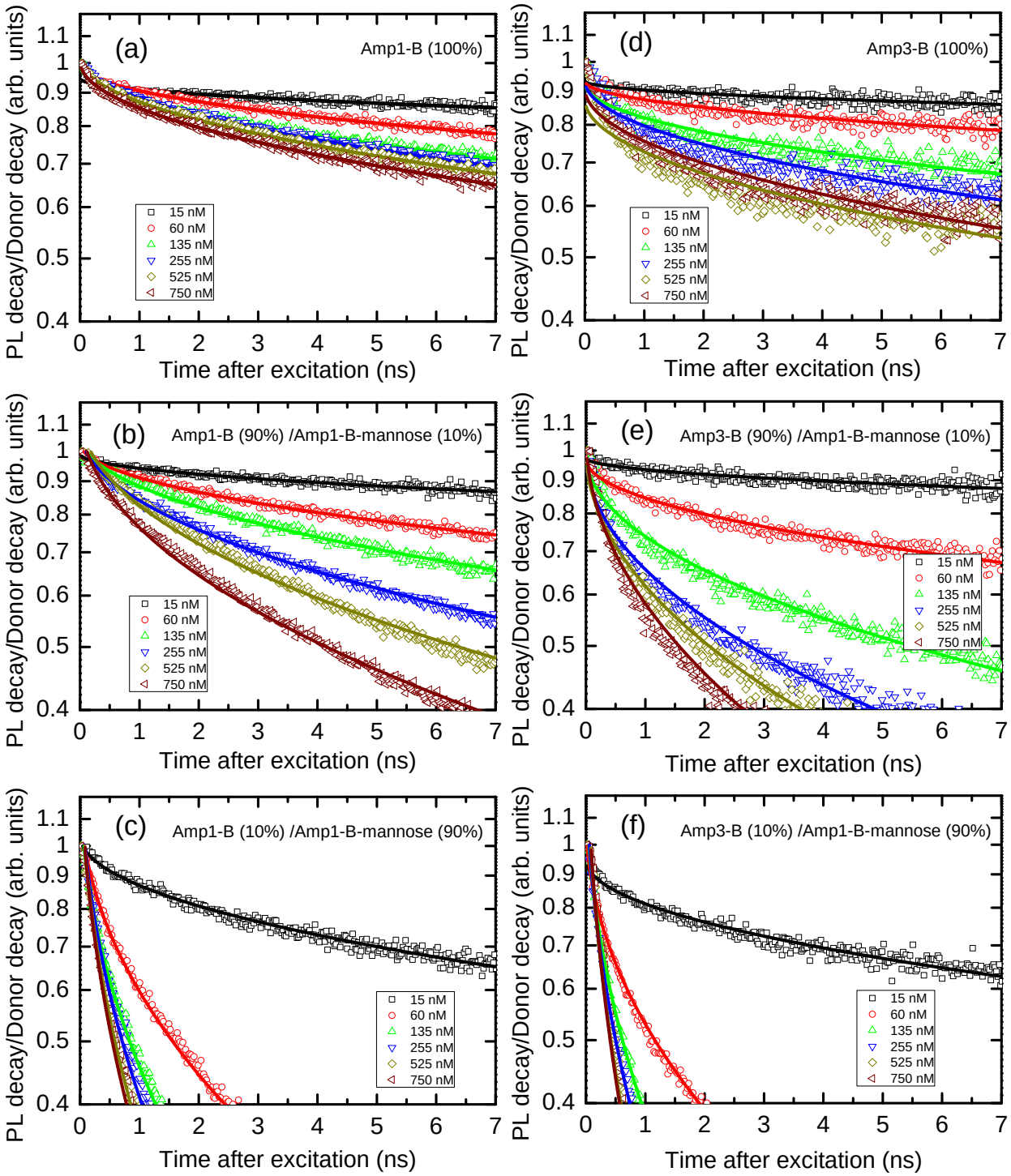


Figure 5.8: Transients of PL decay/donor decay of (a) Amp1-B (b) Amp1-B (90%)/Amp1-B-mannose (10%) (c) Amp1-B (10%)/Amp1-B-mannose (90%) (d) Amp3-B (e) Amp3-B (90%)/Amp1-B-mannose (10%) and (f) Amp3-B (10%)/Amp1-B-mannose (90%) NPs after the addition of ConA/AF633 acceptors at various concentrations in the nanoparticle solution. The solid curves are outputs of fitting based on stretched single exponential function ($\exp[-(k_{DA}t)^{\gamma}]$) with the stretching exponent $\gamma$ of 0.5.

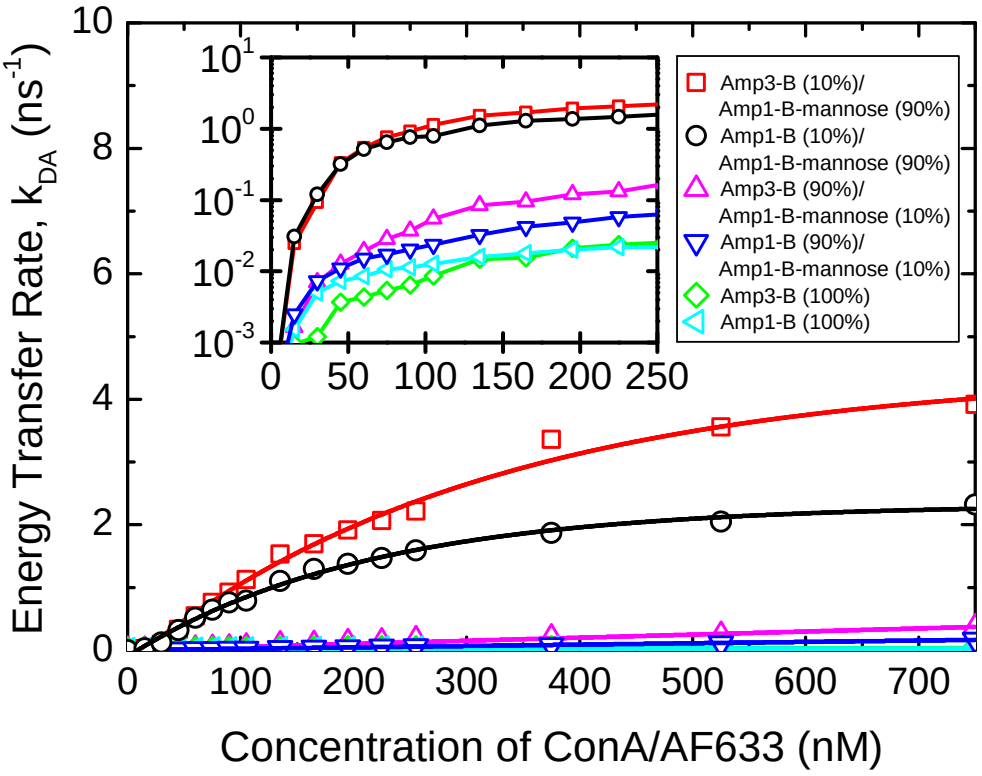


Figure 5.9: The energy transfer rate, $k_{DA}$, of all NPs as a function of the concentrations of ConA/AF633 acceptors in the solution. The solid lines are guides to the eye. The inset is plot of $k_{DA}$ at low concentrations of ConA/AF633 acceptors.

concentration, as seen in the inset of Figure 5.9. This suggests other mechanisms that further enhance the energy transfer rate become active in the Amp3-B/Amp1-B-mannose NPs with ConA/AF633 acceptor system.

It is proposed that the faster energy transfer observed in the Amp3-B/Amp1-B-mannose NPs with ConA/AF633 acceptors, as compared with the Amp1-B/Amp1-B-mannose NPs with ConA/AF633 acceptors, arises from faster exciton hopping to the Amp3-B monomers at surface. The Amp3-B monomer, which has three hydrophilic chains, tends to stay on the surface of nanoparticles owing to the hydrophilic interaction, where water molecules naturally attract the intruding hydrophilic chains in the Amp3-B monomer to form temporary hydrogen bonds [157, 158]. Hence, the exciton migration towards the Amp3-B monomers on the NP surface becomes directional, as schematically shown in Figure 5.10a. Although the ConA/AF633 acceptors are bound to the nanoparticles via the mannoses, the size of ConA is large enough to cover the Amp3-B monomers nearby, and therefore efficient energy transfer is performed from excitons on the Amp3-B monomers to AF633 directly. As mentioned above, Figure 5.5 shows that the PL emission energy is reduced faster in the Amp3-B/Amp1-B-mannose NPs than those in the Amp1-B/Amp1-B-mannose NPs, which suggests the migration of exciton towards the Amp3-B monomers in the Amp3-B/Amp1-B-mannose NPs is more energetic favorable. Since the energy transfer rate is raised with reducing the distance ($r$) between exciton donor and ConA/AF633 acceptor, in accordance with Förster theory ($k \propto \left(\frac{R_0}{r}\right)^6$), and more excitons are funnelled to the NP surface, the energy transfer rate in the Amp3-B/Amp1-B-mannose NPs therefore increases significantly. In contrast, as shown in Figure 5.10b, fewer excitons successfully reach the surface of Amp1-B/Amp1-B-mannose NPs than that in Amp3-B/Amp1-B-mannose NPs. It is due to the distribution of sites with different energy in Amp1-B/Amp1-B-mannose NPs is more homogeneous and therefore exciton migration is not necessarily orientated towards the surface.

From the above analysis, two factors can significantly raise the energy transfer rates: (1) increasing the molar fraction of mannose in the nanoparticles to render more ConA/AF633 acceptors in the solution bound on the NP surface, and (2) introducing Amp3-B monomers

in the nanoparticles to channel excitons to the surface by energetic cascades. However, it is a trade-off between these two factors. When the Amp3-B monomers compete to locate on the surface of nanoparticles, the amount of mannose exposing to the solution will be decreased. Hence, the molar ratios of Amp1-B-mannose and Amp3-B monomers in nanoparticles need to be optimised in order to achieve the highest energy transfer rate in the system, and guarantee a high signal-to-noise ConA/AF633 emission, which is highly beneficial in the bio-sensing and bio-labelling applications.

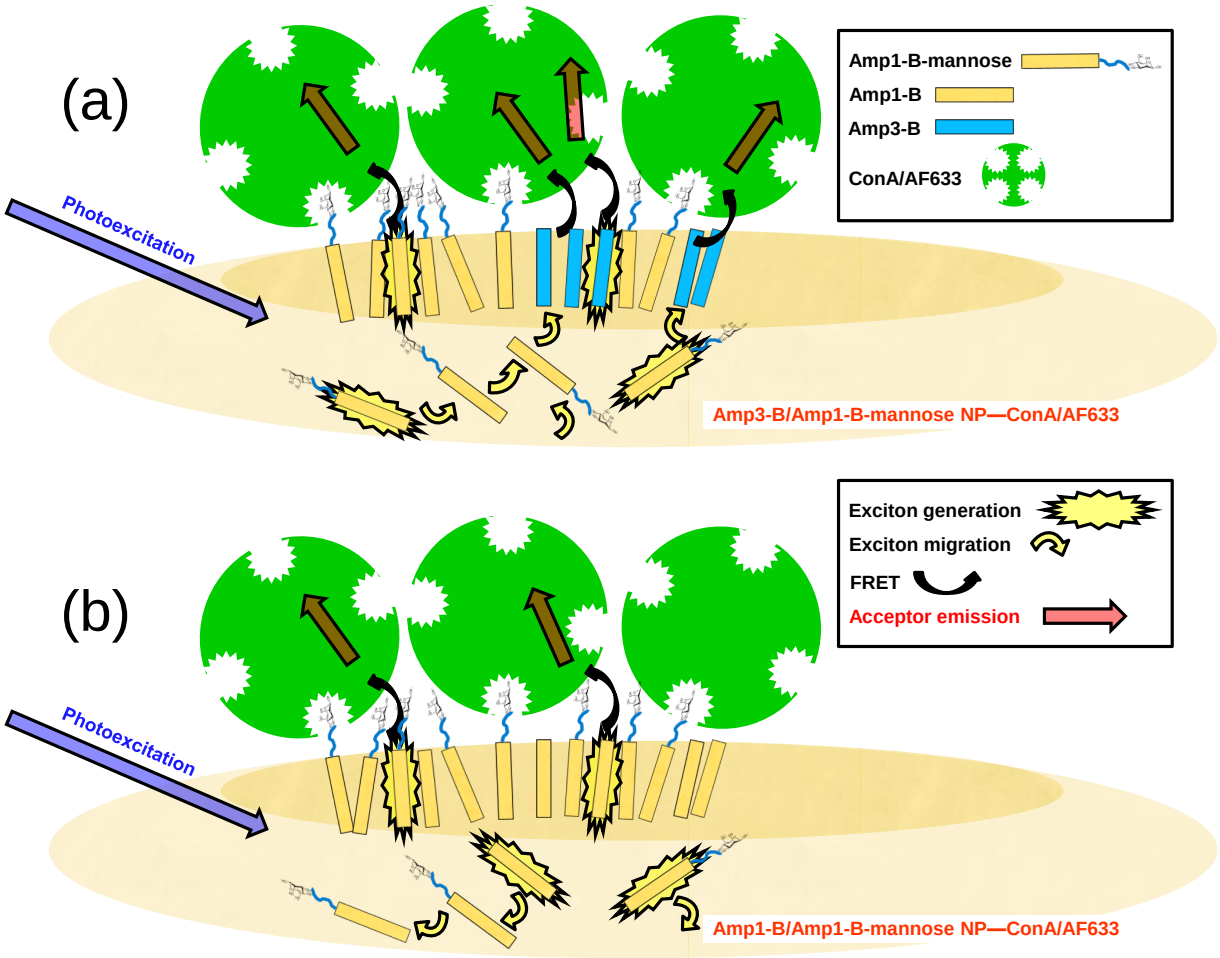


Figure 5.10: Schematic illustrations of (a) exciton migration along the energetic cascade to Amp3-B monomers in Amp3-B/Amp1-B-mannose NP with ConA/AF633, which causes efficient directional exciton movement towards the NP surface; (b) more random exciton hopping in Amp1-B/Amp1-B-mannose NP with ConA/AF633, where fewer excitons successfully arrive the surface than the case in (a).

## 5.4 Conclusion

In this chapter, strong evidence has been provided for significant exciton migration along the amphiphilic monomers in self-assembled nanoparticles by energetic cascades. The red-shifted average emission energy of excitons in all nanoparticles in the 8 ns observation window is attributed to the exciton hopping from where excitons are generated, to sites with lower energy. In addition, a higher molar ratio of Amp1-B-mannose in nanoparticles results in a larger emission energy shift. The study of Förster resonance energy transfer from excitons on photoexcited amphiphilic monomers to ConA/AF633 acceptors shows that the amount of mannose, which provides the ligand for the ConA/AF633 acceptor, is crucial for the energy transfer rate. On the other hand, Amp3-B monomers can create more energetically favorable pathways for excitons in Amp3-B/Amp1-B-mannose NPs towards the surface and therefore further increase the energy transfer rates. However, in a nanoparticle, an increase in the molar fraction of Amp3-B results in a decrease in that of Amp1-B-mannose, and the number of monomers on the surface of nanoparticles is limited. Therefore, optimisation of these two parameters is able to achieve the highest energy transfer rate in the system, which leads to a high signal-to-noise ConA/AF633 emission. These new surface-functionalized-nanoparticles with investigated fluorescening and targeting characteristics exhibit potential to be utilised in medical applications.

# Chapter 6

# Conclusions and Outlook

In this thesis, fundamental photophysics and excitation energy transfer in biomimetic and biosensing molecular nanomaterials have been investigated using ultrafast time-resolved photoluminescence spectroscopy. This method has been proven to be an ideal tool to study physical processes following photon absorption, including radiative photon emission and non-radiative energy relaxation pathways on a timescale of sub-picoseconds to several nanoseconds. Some of the interesting physical phenomena relevant to light-harvesting and biological applications have been observed.

In Chapter 4, fully $\pi$-conjugated porphyrin nanoring systems with various number of porphyrins incorporated have demonstrated full delocalisation of the absorbing excited state among the entire ring. This electronic property has been confirmed by the initial PL anisotropy of polarisation smaller than 0.1. It is remarkable such spatially coherent excitations are able to exist in the ring of 24 porphyrin units with a diameter of $\sim$10 nm, which is the largest artificially-synthesised molecular nanoring at present. The structurally symmetric constraint for radiative transitions can be lifted by the deviation from the ideal ring-like symmetry of nanoring structures via static and dynamic distortions. In larger rings, static distortions dominate and allow direct Franck-Condon transitions, whilst in smaller rings, dynamic distortion plays an important role to redistribute the intensity from a higher-lying electronically allowed state of symmetry to the lowest one through a coupled electronic-

vibrational transition, increasing the radiative transition rates. These findings open promising new opportunities for using these man-made light-harvesting materials that match the efficiency of their natural counterparts in technological applications.

Generally, disorder-induced weakening of the electronic coupling between porphyrin units leads to an incoherent excitation transfer in light-harvesting process. However, in some other biological systems, when the order of magnitude of electronic coupling strength is comparable to the reorganisation energy[164–166], it is interesting that the protein scaffolds surrounding the light-harvesting units may be able to keep the electronic coherence in hundreds of femtoseconds between the chromophores by their corresponding coherent vibration [167]. The coherent exciton waves may interfere with one another and avoid the energy trapping location in the pathway to reach the chemical reaction centre, which may be the reason that the natural light-harvesting systems usually have a quantum yield of nearly 100% for excitation energy transfer [168]. Therefore, it may be useful to examine how long the full electronic delocalisation can remain in our nanorings, by for example 2D photon echo spectroscopy [169], which provide a comparison of photophysics between the artificial and natural systems. The man-made prophyrin nanorings provide an opportunity to surpass their natural counterparts by offering more robust and perhaps longer timescale of coherent state wavefunctions. Furthermore, it is intriguing to establish a network using our nanorings as building blocks in an organic photovoltaic cell to realise a long-distance excitation energy transfer with high quantum efficiency in the future.

Homotransfer and heterotransfer of excitation energy in self-assembled nanoparticles in water has been investigated in Chapter 5. The time evolution of the average emission energy of excitons in the 8 ns observation window in various nanoparticles suggests significant exciton migration from where excitons are generated, to sites with lower energy, where higher molar fraction of mannose in nanoparticles leads to larger average energy shift. The Förster resonance energy transfer from excitons on photoexcited monomers to ConA/AF633 acceptors, which are connected onto the surface of nanoparticles via the binding between mannose and ConA, confirms that higher molar fraction of mannose in nanoparticles raises the energy

transfer rate more significantly. Furthermore, in Amp3-B/Amp1-B-mannose NPs, the energetic cascades towards the surface of nanoparticles are more efficient for excitons than that in Amp1-B/Amp1-B-mannose NPs, resulting in faster exciton migration to the region near ConA/AF633 acceptors, and therefore higher energy transfer rates were observed. Nevertheless, in a nanoparticle, an increase in the number of Amp3-B results in a decrease in that of Amp1-B-mannose, and the number of monomers on the surface is limited. Hence, optimisation of the amount of Amp1-B-mannose and Amp3-B monomers is crucial for maximising the energy transfer rate in the system and for achieving a high signal-to-noise ConA/AF633 emission. These findings provide opportunities for new carbohydrate-coated organic amphiphilic nanoparticles to be used in biological sensing and labelling applications.

An interesting topic would be the modelling of Förster resonance energy transfer considering the exciton migration along the amphiphilic monomers by Monte Carlo simulation, which would be able to further provide more accurate energy transfer rate between excitons on the surface of nanoparticle and ConA/AF633 acceptors. This simulation could also estimate the average number of ConA/AF633 acceptors attached to mannose per nanoparticle, instead of their total amount dissolved in solution, where the binding between ConA and mannose via monovalent linkage is actually very weak, and it is difficult to estimate that number from the experimental results. In addition, further investigation could concentrate on the performance of energy transfer rates when an alternative ligand is synthesised on monomers; for instance, biotin can also be covalently linked on Amp1-B monomers [148]. Therefore, Förster resonance energy transfer can be realised between nanoparticles and acceptors-labelled streptavidin (SA), which is able to recognise and to be bound to biotin. In reference [148], it is shown that energy transfer rates are higher in biotin–NPs/SA/AF633 than mannose–NPs/ConA/AF633, so it is interesting to examine the cause, which may be due to a shorter distance between the donor–acceptor or more energetically favorable cascades towards the NP surface existing in biotin–NPs/SA/AF633 than in mannose-NPs/ConA/AF633. Understanding the mechanisms of excitation energy transfer in organic nanoparticles is crucial for optimisation of their optical performance in possible medical applications.

# Bibliography


[1] C. K. Chiang, C. R. Fincher, Y. W. Park, A. J. Heeger, H. Shirakawa *et al.*, *Phys. Rev. Lett.*, 39 1098 (1977).

[2] J. H. Burroughes, D. D. C. Bradley, A. R. Brown, R. N. Marks, K. Mackay *et al.*, *Nature*, 347 (6293) 539 (1990).

[3] L. Schmidt-Mende, A. Fechtenktter, K. Mllen, E. Moons, R. H. Friend *et al.*, *Science*, 293 (5532) 1119 (2001).

[4] G. Li, V. Shrotriya, J. Huang, Y. Yao, T. Moriarty *et al.*, *Nat Mater*, 4 (11) 864 (2005).

[5] R. H. Friend, R. W. Gymer, A. B. Holmes, J. H. Burroughes, R. N. Marks *et al.*, *Nature*, 397 (6715) 121 (1999).

[6] H. Sirringhaus, N. Tessler, & R. H. Friend, *Science*, 280 (5370) 1741 (1998).

[7] H. Sirringhaus, T. Kawase, R. H. Friend, T. Shimoda, M. Inbasekaran *et al.*, *Science*, 290 (5499) 2123 (2000).

[8] L. Chen, D. W. McBranch, H.-L. Wang, R. Helgeson, F. Wudl *et al.*, *Proceedings of the National Academy of Sciences*, 96 (22) 12287 (1999).

[9] S.-S. Sun & L. R. Dalton, *Introduction to organic electronic and optoelectronic materials and devices*, CRC Press, 3rd edn. (2008).

[10] K. Ariga, J. P. Hill, & Q. Ji, *Phys. Chem. Chem. Phys.*, 9 2319 (2007).

[11] G. D. Scholes, *The Journal of Physical Chemistry Letters*, 1 (1) 2 (2010).

[12] N. Aratani, D. Kim, & A. Osuka, *Accounts Chem. Res.*, 42 1922 (2009).

[13] H. S. Cho, H. Rhee, J. K. Song, C. K. Min, M. Takase *et al.*, *J. Am. Chem. Soc.*, 125 5849 (2003).

[14] T. Hori, X. Peng, N. Aratani, A. Takagi, T. Matsumoto *et al.*, *Chem. Eur. J*, 14 582 (2008).

[15] M. C. OSullivan, J. K. Sprafke, D. V. Kondratuk, C. Rinfray, T. D. W. Claridge *et al.*, *Nature*, 469 (7328) 72 (2011).

[16] P. Sharma, S. Brown, G. Walter, S. Santra, & B. Moudgil, *Advances in Colloid and Interface Science*, 123126 (0) 471 (2006).

[17] D. J. Maxwell, J. R. Taylor, & S. Nie, *Journal of the American Chemical Society*, 124 (32) 9606 (2002).

[18] N.-T. Chen, S.-H. Cheng, C.-P. Liu, J. S. Souris, C.-T. Chen *et al.*, *International Journal of Molecular Sciences*, 13 (12) 16598 (2012).

[19] X. Gao, Y. Cui, R. M. Levenson, L. W. K. Chung, & S. Nie, *Nat Biotech*, 22 (8) 969 (2004).

[20] J. K. Oh, *J. Mater. Chem.*, 20 8433 (2010).

[21] I. L. Medintz, H. T. Uyeda, E. R. Goldman, & H. Mattoussi, *Nat Mater*, 4 (6) 435 (2005).

[22] T. Zhang, J. L. Stilwell, D. Gerion, L. Ding, O. Elboudwarej *et al.*, *Nano Letters*, 6 (4) 800 (2006).

[23] A. Kaeser & A. P. H. J. Schenning, *Advanced Materials*, 22 (28) 2985 (2010).

[24] M. E. Davis, Z. Chen, & D. M. Shin, *Nat Rev Drug Discov*, 7 (9) 771 (2008).

[25] A. A. Bakulin, A. Rao, V. G. Pavelyev, P. H. M. van Loosdrecht, M. S. Pshenichnikov *et al.*, *Science*, 335 1340 (2012).

[26] R. Österbacka, C. P. An, X. M. Jiang, & Z. V. Vardeny, *Science*, 287 839 (2000).

[27] J. K. Sprafke, D. V. Kondratuk, M. Wykes, A. L. Thompson, M. Hoffmann *et al.*, *J. Am. Chem. Soc.*, 133 17262 (2011).

[28] G. Orlandi & W. Siebrand, *J. Chem. Phys.*, 58 4513 (1973).

[29] S. Leach, M. Vervloet, A. Despres, E. Breheret, J. P. Hare *et al.*, *Chem. Phys.*, 160 451 (1992).

[30] J. McMurry, *Organic chemistry*, Thomson Brooks/Cole, 5th edn. (1999).

[31] K. J. Laidler, J. H. Meiser, & B. C. Sanctuary, *Physical chemistry*, Houghton Mifflin, 4th edn. (2003).

[32] S. N. Ege, *Organic chemistry: structure and reactivity*, Houghton Mifflin, 5th edn. (2004).

[33] A. J. Heeger, N. S. Sariciftci, & E. B. Namdas, *Organic chemistry: structure and reactivity*, Oxford University Press, 1st edn. (2010).

[34] P. Atkins & R. Friedman, *Molecular quantum mechanics*, Oxford University Press, 3rd edn. (1997).

[35] R. F. Pierret, *Advanced semiconductor fundamentals*, Prentice Hall/Pearson Education, 2nd edn. (2006).

[36] M. Sze, *Physics of semiconductor devices*, Wiley-Interscience, 3rd edn. (2006).

[37] H. van Mullekom, J. Vekemans, E. Havinga, & E. Meijer, *Materials Science and Engineering: R: Reports*, 32 (1) 1 (2001).

[38] B. Valeur & M. N. Berberan-Santos, *Molecular fluorescence*, Wiley-VCH, 2nd edn. (2013).

[39] W. W. Parson, *Modern optical spectroscopy: with examples from piophysics and biochemistry*, Springer-Verlag, 1st edn. (2007).

[40] M. Yurkin & A. Hoekstra, *Journal of Quantitative Spectroscopy and Radiative Transfer*, 106 (13) 558 (2007).

[41] P. A. M. Dirac, *Proceedings of the Royal Society of London. Series A*, 114 (767) 243 (1927).

[42] P. J. Feibelman & D. E. Eastman, *Phys. Rev. B*, 10 4932 (1974).

[43] R. C. Hilborn, *American Journal of Physics*, 50 (11) 982 (1982).

[44] M. Kasha, *Radiation Research*, 20 (1) pp. 55 (1963).

[45] W.-M. Y. et al, *Journal of Physics G: Nuclear and Particle Physics*, 33 (1) 1 (2006).

[46] R. J. Elliott, *Phys. Rev.*, 96 266 (1954).

[47] M. Born & R. Oppenheimer, *Ann. Phys.*, 84 457 (1927).

[48] W. S. Struve, *Fundamental of molecular spectroscopy*, Wiley-Interscience, 1st edn. (1989).

[49] L. S. Cederbaum, *The Journal of Chemical Physics*, 128 (12) 124101 (2008).

[50] E. U. Condon, *American Journal of Physics*, 15 (5) 365 (1947).

[51] M. Liess, S. Jeglinski, Z. V. Vardeny, M. Ozaki, K. Yoshino *et al.*, *Phys. Rev. B*, 56 15712 (1997).

[52] T. Takagahara, *Journal of Luminescence*, 70 (16) 129 (1996).

[53] C. Manneback, *Physica*, 17 (1112) 1001 (1951).

[54] M. Pope & C. E. Swenberg, *Electronic processes in organic crystals and polymers*, Oxford University Press, 1st edn. (1999).

[55] M. Kasha, *Radiation Research*, 20 (1) pp. 55 (1963).

[56] G. D. Scholes & G. Rumbles, *Nat Mater*, 5 (9) 683 (2006).

[57] H. Fidder, J. Terpstra, & D. A. Wiersma, *The Journal of Chemical Physics*, 94 (10) 6895 (1991).

[58] M. Grover & R. Silbey, *The Journal of Chemical Physics*, 54 (11) 4843 (1971).

[59] Y. Kayanuma, *Phys. Rev. B*, 38 9797 (1988).

[60] R. L. Greene, K. K. Bajaj, & D. E. Phelps, *Phys. Rev. B*, 29 1807 (1984).

[61] H. van Amerongen, L. Valkunas, & R. van Grondelle, *Photosynthetic excitons*, World Scientific Publishing, 1st edn. (2000).

[62] G. A. Kaminski, R. A. Friesner, & R. Zhou, *Journal of Computational Chemistry*, 24 (3) 267 (2003).

[63] J. M. Rib, J. M. Bofill, J. Crusats, & R. Rubires, *Chemistry — A European Journal*, 7 (13) 2733 (2001).

[64] G. A. Crosby & J. N. Demas, *The Journal of Physical Chemistry*, 75 (8) 991 (1971).

[65] M. Kasha, *Discuss. Faraday Soc.*, 9 14 (1950).

[66] U. Rauscher, H. Bässler, D. D. C. Bradley, & M. Hennecke, *Phys. Rev. B*, 42 9830 (1990).

[67] B. Bagchi, D. W. Oxtoby, & G. R. Fleming, *Chemical Physics*, 86 (3) 257 (1984).

[68] J. B. Birks & D. J. Dyson, *Proceedings of the Royal Society of London. Series A. Mathematical and Physical Sciences*, 275 (1360) 135 (1963).

[69] P. Klan & J. Wirz, *Photochemistry of organic compounds: from concepts to practice*, John Wiley and Sons, Ltd., 1st edn. (2009).

[70] A. Einstein, *Annalen der Physik*, 322 (8) 549 (1905).

[71] M. von Smoluchowski, *Annalen der Physik*, 326 (14) 756 (1906).

[72] L. D. Landau & E. M. Lifshitz, *Statistical physics*, Oxford: Butterworth–Heinemann, 3rd edn. (1980).

[73] S. J. Strickler & R. A. Berg, *The Journal of Chemical Physics*, 37 (4) 814 (1962).

[74] R. T. Ross, *Photochemistry and Photobiology*, 21 (6) 401 (1975).

[75] R. H. Friend, D. D. C. Bradley, & P. D. Townsend, *Journal of Physics D: Applied Physics*, 20 (11) 1367 (1987).

[76] O. Kuhn, V. Sundstrom, & T. Pullerits, *Chemical Physics*, 275 (13) 15 (2002).

[77] A. Ishizaki & G. R. Fleming, *The Journal of Chemical Physics*, 130 (23) 234110 (2009).

[78] O. Kühn & V. Sundström, *The Journal of Chemical Physics*, 107 (11) 4154 (1997).

[79] T. Forster, *Discuss. Faraday Soc.*, 27 7 (1959).

[80] D. Andrews, C. Curutchet, & G. Scholes, *Laser Photonics Reviews*, 5 (1) 114 (2011).

[81] T. Gadella (editor), *Volume 33: FRET and FLIM techniques*, Elsevier Science, 1st edn. (2008).

[82] D. L. Dexter, *The Journal of Chemical Physics*, 21 (5) 836 (1953).

[83] M. Berberan-Santos, E. Bodunov, & B. Valeur, *Chemical Physics*, 315 (12) 171 (2005).

[84] S. I. Hintschich, F. B. Dias, & A. P. Monkman, *Phys. Rev. B*, 74 045210 (2006).

[85] H. Abramczyk, *Introduction to laser spectroscopy*, Elsevier Science, 1st edn. (2005).

[86] C. Yang, D.-W. Huang, C.-W. Hsu, S.-Y. Liang, C.-W. Lay *et al.*, *International Journal of High Speed Electronics and Systems*, 8 599 (1997).

[87] G. Rupper, N. H. Kwong, & R. Binder, *Phys. Rev. Lett.*, 97 117401 (2006).

[88] M. Fox (editor), *Optical properties of solids*, Oxford University Press, 1st edn. (2001).

[89] C. Rulliere (editor), *Femtosecond laser pulses: principles and experiments*, Springer–Verlag, 1st edn. (1998).

[90] D. Nikogosyan, *Applied Physics A*, 52 (6) 359 (1991).

[91] W. Becker (editor), *Advanced time-correlated single photon counting techniques*, Springer, 1st edn. (2005).

[92] W. Kühlbrandt, D. N. Wang, & Y. Fujiyoshi, *Nature*, 367 614 (1994).

[93] G. McDermott, S. M. Prince, A. A. Freer, A. M. Hawthornthwaite-Lawless, M. Z. Papiz *et al.*, *Nature*, 374 517 (1995).

[94] A. M. van Oijen, M. Ketelaars, J. Köhler, T. J. Aartsma, & J. Schmidt, *Science*, 285 400 (1999).

[95] G. S. Engel, T. R. Calhoun, E. L. Read, T. K. Ahn, T. Mancal *et al.*, *Nature*, 446 782 (2007).

[96] J. L. Herek, W. Wohlleben, R. J. Cogdell, D. Zeidler, & M. Motzkus, *Nature*, 417 533 (2002).

[97] V. Sundström, T. Pullerits, & R. van Grondelle, *J. Phys. Chem. B*, 103 2327 (1999).

[98] R. Jimenez, S. N. Dikshit, S. E. Bradforth, & G. R. Fleming, *J. Phys. Chem.*, 100 6825 (1996).

[99] M. Dahlbom, T. Pullerits, S. Mukamel, & V. Sandstrom, *J. Phys. Chem. B*, 105 5515 (2001).

[100] D. Leupold, H. Stiel, K. Teuchner, F. Nowak, W. Sandner *et al.*, *Phys. Rev. Lett.*, 77 4675 (1996).

[101] Y. Kim, S. Cook, S. M. Tuladhar, S. A. Choulis, J. Nelson *et al.*, *Nat. Mater.*, 5 197 (2006).

[102] S. H. Park, A. Roy, S. Beaupre, S. Cho, N. Coates *et al.*, *Nat. Photonics*, 3 297 (2009).

[103] M. C. O'Sullivan, J. K. Sprafke, D. V. Kondratuk, C. Rinfray, T. D. W. Claridge *et al.*, *Nature*, 469 72 (2011).

[104] P. N. Taylor & H. L. Anderson, *J. Am. Chem. Soc.*, 121 11538 (1999).

[105] A. Saywell, J. K. Sprafke, L. J. Esdaile, A. J. Britton, A. Rienzo *et al.*, *Angew. Chem.-Int. Edit.*, 49 9136 (2010).

[106] D. V. Kondratuk, L. M. A. Perdigao, M. C. O. Sullivan, S. Svatek, G. Smith *et al.*, *Angew. Chem.-Int. Edit.*, 51 6696 (2012).

[107] M. Hoffmann, J. Kärnbratt, M. H. Chang, L. M. Herz, B. Albinsson *et al.*, *Angew. Chem.-Int. Edit. Engl.*, 120 5071 (2008).

[108] F. C. Grozema, C. Houarner-Rassin, P. Prins, L. D. A. Siebbeles, & H. L. Anderson, *J. Am. Chem. Soc.*, 129 13370 (2007).

[109] M. Drobizhev, Y. Stepanenko, A. Rebane, C. J. Wilson, T. E. O. Screen *et al.*, *J. Am. Chem. Soc.*, 128 12432 (2006).

[110] M. Hoffmann, C. J. Wilson, B. Odell, & H. L. Anderson, *Angew. Chem. Int. Ed.*, 46 3122 (2007).

[111] S. Karrasch, P. A. Bullough, & R. Ghosh, *Embo J.*, 14 631 (1995).

[112] M. C. Yoon, S. Cho, P. Kim, T. Hori, N. Aratani *et al.*, *J. Phys. Chem. B*, 113 15074 (2009).

[113] T. M. Wilson, T. Hori, M.-C. Yoon, N. Aratani, A. Osuka *et al.*, *J. Am. Chem. Soc.*, 132 1383 (2010).

[114] M. Williams-Harry, A. Bhaskar, G. Ramakrishna, T. Goodson, M. Imamura *et al.*, *J. Am. Chem. Soc.*, 130 3252 (2008).

[115] J. E. Donehue, O. P. Varnavski, R. Cemborski, M. Iyoda, & T. Goodson, *J. Am. Chem. Soc.*, 133 4819 (2011).

[116] V. S. Y. Lin, S. G. Dimagno, & M. J. Therien, *Science*, 264 1105 (1994).

[117] M. H. Chang, M. Hoffmann, H. L. Anderson, & L. M. Herz, *J. Am. Chem. Soc.*, 130 10171 (2008).

[118] G. Trinkunas, J. L. Herek, T. Polìvka, V. Sundström, & T. Pullerits, *Phys. Rev. Lett.*, 86 4167 (2001).

[119] B. Valeur, Molecular Fluorescence: Principles and applications, Germany (2002).

[120] D. Magde, *J. Chem. Phys.*, 68 3717 (1978).

[121] L. D. Book, A. E. Ostafin, N. Ponomarenko, J. R. Norris, & N. F. Scherer, *J. Phys. Chem. B*, 104 8295 (2000).

[122] J. T. M. Kennis, A. M. Streltsov, S. I. E. Vulto, T. J. Aartsma, T. Nozawa *et al.*, *J. Phys. Chem. B*, 101 7827 (1997).

[123] A. Hiraya & K. Shobatake, *J. Chem. Phys.*, 94 7700 (1991).

[124] T. Hashimoto, H. Nakano, & K. Hirao, *J. Mol. Struct.*, 451 25 (1998).

[125] M. A. Bopp, A. Sytnik, T. D. Howard, R. J. Cogdell, & R. M. Hochstrasser, *Proc. Natl. Acad. Sci. USA*, 96 11271 (1999).

[126] J. M. Hollas, High Resolution Spectroscopy, U. K. (1998).

[127] G. Herzberg, Molecular Spectra and Molecular Structure, III. Electronic Spectra and Electronic Sturcture of Polyatomic Molecules, Florida (1966).

[128] H. Sponer, G. Nordheim, A. L. Sklar, & E. Teller, *J. Chem. Phys.*, 7 207 (1939).

[129] G. Orlandi & F. Negri, *Photochem. Photobiol. Sci.*, 1 289 (2002).

[130] S. A. Svatek, L. M. A. Perdigao, A. Stannard, M. B. Wieland, D. V. Kondratuk *et al.*, *Nano Letters*, 13 (7) 3391 (2013).

[131] M. Ketelaars, A. M. van Oijen, M. Matsushita, J. Kohler, J. Schmidt *et al.*, *Biophys. J.*, 80 1591 (2001).

[132] R. Monshouwer, M. Abrahamsson, F. Vanmourik, & R. Vangrondelle, *J. Phys. Chem. B*, 101 7241 (1997).

[133] C. Zhu, L. Liu, Q. Yang, F. Lv, & S. Wang, *Chemical Reviews*, 112 (8) 4687 (2012).

[134] X. Feng, L. Liu, S. Wang, & D. Zhu, *Chem. Soc. Rev.*, 39 2411 (2010).

[135] B. Htzer, I. L. Medintz, & N. Hildebrandt, *Small*, 8 (15) 2297 (2012).

[136] N. L. Rosi & C. A. Mirkin, *Chemical Reviews*, 105 (4) 1547 (2005).

[137] R. E. Bailey, A. M. Smith, & S. Nie, *Physica E: Low-dimensional Systems and Nanostructures*, 25 (1) 1 (2004).

[138] V. Biju, T. Itoh, & M. Ishikawa, *Chem. Soc. Rev.*, 39 3031 (2010).

[139] K. L. Aillon, Y. Xie, N. El-Gendy, C. J. Berkland, & M. L. Forrest, *Advanced Drug Delivery Reviews*, 61 (6) 457 (2009).

[140] V. Mailander & K. Landfester, *Biomacromolecules*, 10 (9) 2379 (2009).

[141] U. Scherf, S. Adamczyk, A. Gutacker, & N. Koenen, *Macromolecular Rapid Communications*, 30 (13) 1059 (2009).

[142] D. Venturoli & B. Rippe, *American Journal of Physiology - Renal Physiology*, 288 (4) F605 (2005).

[143] M. R. Dreher, W. Liu, C. R. Michelich, M. W. Dewhirst, F. Yuan *et al.*, *Journal of the National Cancer Institute*, 98 (5) 335 (2006).

[144] T. Nomura, N. Koreeda, F. Yamashita, Y. Takakura, & M. Hashida, *Pharmaceutical Research*, 15 128 (1998).

[145] Z. Tian, J. Yu, C. Wu, C. Szymanski, & J. McNeill, *Nanoscale*, 2 1999 (2010).

[146] M. Heilemann, R. Kasper, P. Tinnefeld, & M. Sauer, *Journal of the American Chemical Society*, 128 (51) 16864 (2006).

[147] J. Lee, A. O. Govorov, & N. A. Kotov, *Nano Letters*, 5 (10) 2063 (2005).

[148] K. Petkau, A. Kaeser, I. Fischer, L. Brunsveld, & A. P. H. J. Schenning, *Journal of the American Chemical Society*, 133 (42) 17063 (2011).

[149] A. Kaeser, I. Fischer, R. Abbel, P. Besenius, D. Dasgupta *et al.*, *ACS Nano*, 7 (1) 408 (2013).

[150] A. Suzuki, *Journal of Organometallic Chemistry*, 576 (12) 147 (1999).

[151] Y. Liang, H. Wang, S. Yuan, Y. Lee, L. Gan *et al.*, *J. Mater. Chem.*, 17 2183 (2007).

[152] J. H. Naismith & R. A. Field, *Journal of Biological Chemistry*, 271 (2) 972 (1996).

[153] G. M. Edelman, B. A. Cunningham, G. N. Reeke, J. W. Becker, M. J. Waxdal *et al.*, *Proceedings of the National Academy of Sciences*, 69 (9) 2580 (1972).

[154] D. F. Senear & D. C. Teller, *Biochemistry*, 20 (11) 3076 (1981).

[155] H. Kasai, H. S. Nalwa, H. Oikawa, S. Okada, H. Matsuda *et al.*, *Japanese Journal of Applied Physics*, 31 (Part 2, No. 8A) L1132 (1992).

[156] J. Huh, V. V. Ginzburg, & A. C. Balazs, *Macromolecules*, 33 (21) 8085 (2000).

[157] D. Chandler, *Nature*, 437 (7059) 640 (2005).

[158] T. P. Silverstein, *Journal of Chemical Education*, 75 (1) 116 (1998).

[159] D. R. Lide, *CRC Handbook of Chemistry and Physics, 93rd Edition (CRC Handbook of Chemistry & Physics)*, CRC Press (2007).

[160] L. M. Herz, C. Silva, R. H. Friend, R. T. Phillips, S. Setayesh *et al.*, *Phys. Rev. B*, 64 195203 (2001).

[161] R. C. Powell, *Phys. Rev. B*, 2 2090 (1970).

[162] R. C. Powell & Z. G. Soos, *Journal of Luminescence*, 11 (12) 1 (1975).

[163] R. C. Powell & R. G. Kepler, *Phys. Rev. Lett.*, 22 636 (1969).

[164] G. S. Engel, T. R. Calhoun, E. L. Read, T.-K. Ahn, T. Mancal *et al.*, *Nature*, 446 (7137) 782 (2007).

[165] G. S. Schlau-Cohen, A. Ishizaki, T. R. Calhoun, N. S. Ginsberg, M. Ballottari *et al.*, *Nat Chem*, 4 (5) 389 (2012).

[166] G. R. Fleming, G. S. Schlau-Cohen, K. Amarnath, & J. Zaks, *Faraday Discuss.*, 155 27 (2012).

[167] A. W. Chin, J. Prior, R. Rosenbach, F. Caycedo-Soler, S. F. Huelga *et al.*, *Nat Phys*, 9 (2) 113 (2013).

[168] H. Lee, Y.-C. Cheng, & G. R. Fleming, *Science*, 316 (5830) pp. 1462 (2007).

[169] T. Brixner, T. Mančal, I. V. Stiopkin, & G. R. Fleming, *The Journal of Chemical Physics*, 121 (9) 4221 (2004).